https://doi.org/10.1038/s44310-025-00090-5

Halide Perovskite Nanostructures: Processing Methods and Optoelectronics Applications

Xin Peng[1], Zhengxun Lai[1] ✉, He Shao[2], Yi Shen[2], You Meng[1] ✉ & Johnny C. Ho[2,3,4,5]

Low-dimensional halide perovskites, including quantum dots, nanowires, and nanosheets, hold significant promise for optoelectronic applications due to their distinctive quantum confinement effects, adjustable bandgaps, superior carrier dynamics, and cost-effective solution processing. This review explores the properties and benefits of these materials, which, through dimensional tuning, achieve high photoluminescence quantum yields, robust exciton binding energies, and remarkable defect tolerance. We investigate various prevalent synthesis techniques, such as hot injection, ligand-assisted reprecipitation, and vapor deposition, alongside recent advancements and innovations in these methods. Moreover, we examine the latest research on applying low-dimensional halide perovskites in light-emitting diodes, solar cells, photodetectors, and lasers, emphasizing their potential to revolutionize next-generation optoelectronic devices. The review also addresses key challenges in commercializing these materials and suggests future research directions. By providing comprehensive insights, this review aims to advance the development of high-performance, durable, low-dimensional halide perovskites and their integration into optoelectronic technologies.

In recent years, metal halide perovskites (MHPs) have emerged as a focal point in optoelectronic research due to their exceptional optoelectronic properties and structural versatility[1–3]. In the realm of solar energy, perovskite solar cells have achieved power conversion efficiencies exceeding 26%[4], rivaling traditional silicon-based cells[5]. Moreover, perovskite/silicon tandem cells have reached efficiencies of 33%[6], establishing them as pivotal materials for next-generation photovoltaic technologies[7,8]. Beyond solar cells, MHPs exhibit a high light absorption coefficient(reaching up to ~10^5 cm^{-1})[9], long carrier diffusion lengths (exceeding 1 μm)[10], tunable bandgaps (throughout the visible range)[11], and high photoluminescence quantum yields (PLQY), all achievable through low-cost solution processing. These attributes make them promising candidates for applications in light-emitting diodes (LEDs), photodetectors, and lasers[12–15].

The origins of perovskite trace back to the 19th century when German mineralogist Gustav Rose discovered $CaTiO_3$ in the Ural Mountains, naming it "perovskite" in honor of Russian geologist Lev Perovski[16]. This discovery laid the foundation for the broad application of the term to any compound with the ABX_3 formula (Fig. 1a). In MHPs, the A-site is typically occupied by a large monovalent cation (e.g., Cs^+, MA^+, FA^+, or Rb^+), the B-site by a divalent metal cation (e.g., Pb^{2+}, Sb^{2+}, or Sn^{2+}), and the X-site by a halide anion (Cl^-, Br^-, I^-, or their mixtures)[17–19]. The crystal structure features $[BX_6]^{4-}$ octahedra, with A-site cations residing in the interstitial spaces[20,21]. Although 3D perovskites have attracted considerable attention due to their excellent optoelectronic properties, their practical applications are limited by phase transitions and instability issues induced by moisture, light, and heat[22,23]. To overcome these challenges, researchers have shifted their focus to low-dimensional halide perovskites (LHPs) nanostructures, aiming to endow the materials with new properties and functionalities through dimensional engineering. By tuning the synthesis methods and reaction conditions, the size and shape of MHPs can be adjusted to form 0D quantum dots (QDs) or nanocrystals (NCs), 1D nanowires (NWs) or nanorods (NRs), and 2D nanosheets (NSs) or nanoplatelets (NPLs) (Fig. 1b)[24]. These LHP structures exhibit significant differences in size, surface effects, and quantum confinement, enabling substantial modulation of their optoelectronic properties[25]. 0D QDs, with high exciton binding energies and wide bandgaps, offer high color purity and efficient PLQY, making them ideal for LEDs and display technique[26–28], The most advanced QD LEDs have achieved an external quantum efficiency (EQE) of 30%, along with an operational lifetime exceeding 10,000 hours[29,30]. 1D NWs/NRs, with their high aspect ratios, enable efficient charge transport and show

[1]College of Semiconductors (College of Integrated Circuits), Hunan University, Changsha, China. [2]Department of Materials Science and Engineering, City University of Hong Kong, Kowloon, Hong Kong SAR, China. [3]State Key Laboratory of Terahertz and Millimeter Waves, City University of Hong Kong, Kowloon, Hong Kong SAR, China. [4]Shenzhen Research Institute, City University of Hong Kong, Shenzhen, China. [5]Institute for Materials Chemistry and Engineering, Kyushu University, Fukuoka, Japan. ✉e-mail: laizhengxun@hnu.edu.cn; youmeng@hnu.edu.cn

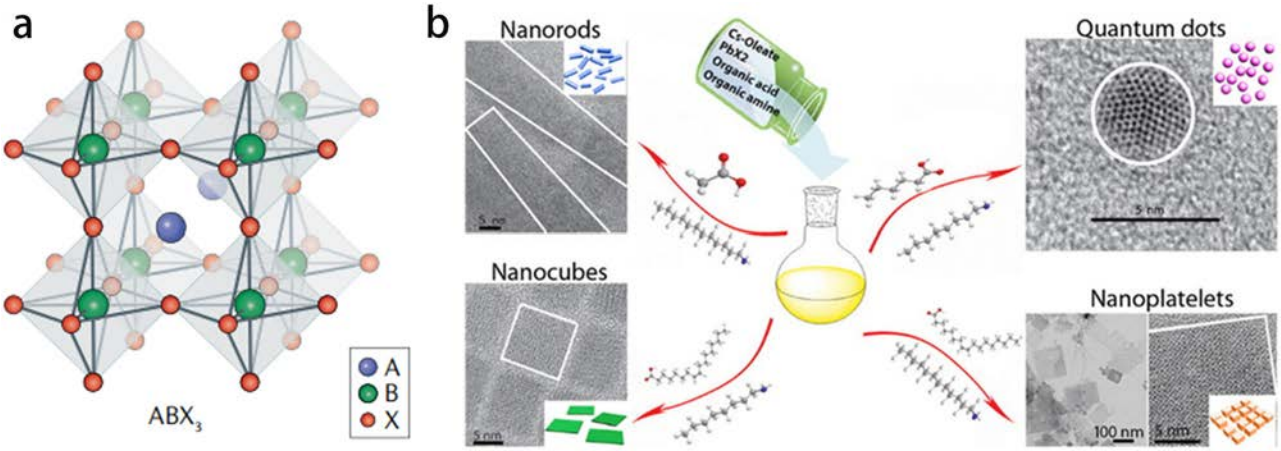

Fig. 1 | Structure and dimensional regulation of perovskites. a Schematic diagram of the ABX_3 crystal structure. **b** Dimensionality control of $CsPbX_3$ NCs via modulation of reaction conditions. **a** Reproduced with permission from ref. 316. Copyright 2019, Springer Nature; **b** Reproduced under the terms of the Creative Commons CC-BY License from ref. 16.

ultrafast response and high gain in photodetectors[31]; for instance, Chen et al. synthesized α-$CsPbI_3$ perovskite NWs arrays for photodetector applications, achieving a responsivity of 1294 A/W and a detectivity of 2.6×10^{14} Jones[32]. 2D NSs/NPLs, with confined electron-hole pairs, enhance PLQY and monochromaticity[19], while their large surface area and hydrophobic interlayer spacers provide excellent environmental stability, making them suitable for photocatalysis and LEDs[33].

Innovations in synthesis methods have propelled the development of LHPs. Techniques like hot injection, ligand-assisted reprecipitation (LARP), exfoliation, and chemical vapor deposition (CVD) offer precise control over size, morphology, composition, and surface chemistry[14,34]. Anion exchange reactions enable continuous tuning of band gaps and emission wavelengths[35]. Hu et al. synthesized a series of $CsPbX_3$ NCs and achieved wide-range tunable PL from 443.3 nm to 649.1 nm via anion exchange[36]. Surface passivation and ligand engineering improve photostability and device performance[37]. Liu et al. introduced 2-bromohexadecanoic acid (BHA) as a bidentate auxiliary ligand for $CsPbX_3$ NCs, which effectively passivated surface defects, resulting in a PLQY as high as 97% even after 48 hours of continuous ultraviolet irradiation[38]. Forming heterostructures with other materials further optimizes performance and expands functionality[39], opening applications in sensing, imaging, biomedicine, and quantum information.

Despite the remarkable advances achieved in LHP materials in recent years and the significant improvements in the performance of related optoelectronic devices, their intrinsic instability and potential toxicity remain key obstacles to large-scale commercial application[40–42]. Researchers are actively exploring various strategies to address the stability issue, such as constructing heterostructures, implementing interface passivation, and optimizing synthesis methods and device encapsulation processes, which have shown promising preliminary results[43,44]. Nevertheless, the operational lifetime of perovskite solar cells still lags far behind that of mature silicon-based modules, and the operational stability of perovskite LEDs remains a major concern[45]. Moreover, these materials are highly sensitive to heat, light, oxygen, and moisture, making them prone to degradation reactions that release toxic byproducts such as PbI_2, posing serious environmental and health risks[46]. Another critical challenge lies in the controllability and reproducibility of large-scale synthesis. Fabrication techniques optimized under laboratory conditions are often difficult to replicate on an industrial scale, where achieving uniformity, consistency, and defect control in high-quality crystals over large areas remains a formidable task[25,47]. In terms of device integration, numerous difficulties also persist, for instance, ensuring compatibility between the perovskite layer and functional components such as electrodes and charge transport layers without compromising performance[48]; assembling flexible, bendable, or multifunctional heterostructure devices[49]; and maintaining long-term structural stability under real-world operating conditions. Therefore, achieving both high device performance and environmental sustainability, along with practical applicability, has become an unavoidable and pressing challenge in the ongoing research of LHPs.

Perovskite materials have been extensively studied, and in contrast to previous reviews that typically focused on a single dimensionality or a specific device type, we present a comprehensive summary of the characteristics and advantages of 0D, 1D, and 2D halide perovskite nanostructures. By comparing materials across different dimensionalities, we elucidate the structure-property relationships that underpin their performance. Furthermore, we provide an in-depth analysis of the synthesis techniques for LHPs, including solution-based methods, vapor-phase deposition, and recent advancements and innovations derived from these approaches. Subsequently, we review the latest progress in applying LHP nanostructures in various optoelectronic devices such as solar cells, LEDs, photodetectors, and lasers. We analyze the major issues and persistent challenges facing this field and discuss recent breakthroughs that aim to address them. Finally, we explore the key obstacles to the industrialization of these materials and outline potential future research directions to contribute to the development of high-performance, high-stability, and commercially viable LHP optoelectronic devices.

Zero-dimensional nanostructure

Properties and advantages

Due to their unique physicochemical properties and excellent performance, 0D halide perovskite nanomaterials have garnered widespread attention in recent years. The main types include NCs and QDs. In contrast to the continuous $[BX_6]^{4-}$ octahedral network of traditional 3D perovskites, 0D halide perovskites consist of independent perovskite units bound together through non-covalent interactions[50,51]. This structural characteristic imparts 0D perovskites with many unique properties. For example, the 0D structure significantly enhances the Coulomb interaction between electrons and holes, producing a much higher exciton binding energy. This characteristic leads to higher luminescence efficiency at room temperature. It effectively reduces the formation of defect states due to the discrete structure, suppressing non-radiative recombination and thereby improving the PLQY[52,53]. Furthermore, due to the quantum confinement effect, 0D halide perovskite NCs typically exhibit a wide bandgap and a narrow emission spectrum, which enables high color purity in light emission[54]. This property is significant for high-performance LEDs, lasers, and display technologies[55]. Regarding stability, the discrete perovskite units are surrounded by organic ligands or inorganic ions, forming strong spatial isolation that prevents environmental moisture from degrading the material, thereby significantly enhancing its moisture resistance[56]. Additionally, the discrete ion units reduce the likelihood of ion

migration, thereby improving the material's thermal stability and laying a solid foundation for its application in practical devices[57]. Notably, by precisely controlling the halide composition and quantum size effects, the bandgap of 0D halide perovskite NCs can be flexibly tuned during synthesis, enabling light emission across the entire visible spectrum[58,59]. This characteristic reveals their tremendous potential for applications in efficient optoelectronic conversion and novel optoelectronic devices.

In conclusion, 0D halide perovskites, with their unique discrete structure, exhibit excellent performance in optical, electrical, and stability-related properties. Their quantum confinement effect, high luminescence efficiency, narrow emission linewidth, wide absorption spectrum, tunable composition, and high defect tolerance make them highly promising for applications in optoelectronic devices.

Synthesis methods

To meet the diverse demands of various applications, the research on the synthesis methods of 0D halide perovskite NCs has continuously evolved and improved. Currently, researchers have developed several efficient synthesis strategies, including hot injection, solvothermal method, ligand-assisted reprecipitation, and ultrasound-assisted method.

Hot injection method. The hot injection method is widely used for synthesizing NCs; the core principle involves rapidly injecting a precursor solution under high-temperature conditions, which induces instantaneous nucleation followed by controlled crystal growth[60]. By strictly controlling factors such as temperature, injection rate, and precursor concentration, it is possible to achieve controllable size, morphology, and distribution of the resulting products[61]. With its simplicity, strong controllability, and excellent reproducibility, the hot injection method has become a classic approach in nanomaterial synthesis[62]. By improving precursor composition and reaction conditions, the stability and performance of the products can be further enhanced, providing more possibilities for the diverse applications of halide perovskites[63]. Leng et al. employed an improved hot injection method to successfully synthesize $CsPbI_3$, $CsPbBr_3$, and $FAPbBr_3$ NCs by optimizing the preparation conditions of the PbX_2 precursor and reaction temperature. They also tuned their emission wavelengths to achieve stable RGB primary color emission (Fig. 2a)[64]. To address the issue of lead toxicity in traditional perovskites, Gao et al. utilized an InI_3-assisted hot injection method (Fig. 2b); by repairing iodine vacancies with I^- ions and controlling crystal growth size with In^{3+} ions, they prepared $Cs_3Cu_2I_5$ NCs (Fig. 2c) with deep blue emission (peak at 440 nm), achieving a PLQY of 96.6% (Fig. 2d). The LEDs made from this material also demonstrated excellent stability, with a half-life exceeding 300 hours[65]. Furthermore, Vighnesh et al. systematically studied the hot injection synthesis of $CsPbBr_3$ NCs (Fig. 2e) and analyzed the effects of precursor ratios, ligand types, and reaction temperatures on material performance. By adjusting the ratio of oleylamine to oleic acid and injecting the precursor solution at 190 °C, they were able to enhance the PLQY of the resulting NCs to 75%, with the particle size distribution maintained around 10 nm[66].

Solid-state heating is also a commonly used approach for synthesizing perovskite NCs. Its principle involves gradually increasing the temperature of the precursor mixture, leading to spontaneous nucleation and crystal growth in a high-temperature solvent[67]. Compared with the traditional hot-injection method, the solid-state heating method offers advantages such as operational simplicity, lower equipment requirements, and suitability for mass production[64]. Chu et al. proposed a simple, scalable one-pot heating strategy to achieve the large-scale synthesis of high-quality, monodisperse Yb^{3+}-doped $CsPbCl_3$ perovskite NCs (Fig. 2f). This method does not require complex pretreatment steps; instead, particle size and Yb^{3+} doping concentration can be tuned simply by controlling the annealing temperature and duration. This strategy overcomes the scalability limitations of traditional hot-injection techniques, achieving a one-time yield exceeding 10 grams (Fig. 2g), and demonstrates promising potential for industrial applications[68].

Solvothermal method. The solvothermal method has become one of the key techniques for synthesizing halide perovskite NCs due to its flexibility, tunability, efficiency, and applicability[69]. This method involves the synthesis of nanomaterials under high-temperature and high-pressure conditions in a sealed container; the elevated temperature and pressure accelerate the decomposition of precursors and ion diffusion, promoting the formation and directional growth of perovskite NCs[70]. Compared to the hot-injection method, the main limitation of the hot-injection method is its strict requirement for an anhydrous and oxygen-free operating environment[71]. In contrast, the solvothermal method is generally easier to implement and more suitable for large-scale production. However, it suffers from longer reaction times and less control over size distribution and reproducibility[72]. Li et al. prepared core-shell structured NCs of $CsPbBr_3$ perovskite QDs coated with an Sn-TiO_2 shell using resaturation recrystallization, sol-gel coating, and solvothermal methods (Fig. 3a). They investigated their photocatalytic performance in the visible-light-driven degradation of the organic dye RhB. The synthesized $CsPbBr_3$/Sn-TiO_2

NCs had a particle size of 15–30 nm, with $CsPbBr_3$ QDs measuring 4-8 nm (Fig. 3b, c). The study showed that the $CsPbBr_3$/Sn-TiO_2 NCs achieved a degradation efficiency of 96.6% for RhB within 30 minutes, with a degradation rate constant of $10.68 \times 10^{-2}\,min^{-1}$, significantly outperforming the traditional P25 photocatalyst. Moreover, after 20 days of water immersion, the absorption edge of $CsPbBr_3$/Sn-TiO_2 showed no significant shift, demonstrating high water stability[73]. In further studies, Ye et al. successfully synthesized $CsPbBr_3/Cs_4PbBr_6$@PbS NCs using the solvothermal method (Fig. 3e). Compared to conventional $CsPbBr_3$ NCs, $CsPbBr_3/Cs_4PbBr_6$@PbS NCs exhibited fluorescence stability at higher temperatures (fluorescence persisted until approximately 200 °C), whereas the fluorescence of $CsPbBr_3$ NCs virtually disappeared at 100 °C (Fig. 3d). After 30 days of immersion in water, the PL intensity of $CsPbBr_3/Cs_4PbBr_6$@PbS NCs remained about 70%, while $CsPbBr_3$ NCs lost almost all fluorescence after only 5 days (Fig. 3f). This indicates that the PbS shell effectively passivates the surface defects of $CsPbBr_3/Cs_4PbBr_6$ NCs, enhancing their thermal and humidity stability. However, introducing the PbS shell slightly reduced the PLQY from 94% to 51.2%[74].

Ligand-assisted reprecipitation method. The LARP method has become a versatile approach for synthesizing perovskite NCs, owing to its operational simplicity, energy-efficient nature, and high production efficiency[75,76]. This approach exploits the inherent solubility differentials between solvents: precursor compounds are first dissolved in a high-solubility solvent system, followed by rapid introduction into a low-solubility antisolvent. The resulting abrupt reduction in solute stability induces instantaneous supersaturation, driving controlled nucleation and subsequent NC precipitation[77]. The addition of ligands can regulate the nucleation and growth processes by coordinating with the reactants or the surfaces of the formed NCs, thereby stabilizing the NCs and improving their morphology and size uniformity[78]. However, one of the main drawbacks of the conventional LARP method is the use of polar solvents such as DMF or DMSO as good solvents, which tend to compromise the stability of perovskite NCs by promoting surface ligand desorption and ionic migration[79]. Recent studies have introduced modified LARP approaches to address this issue, such as using less polar solvents or incorporating suitable dopants to enhance colloidal stability and improve NC quality[80]. Li et al. introduced a novel ligand (DTDB) (Fig. 4a), which enhanced the surface passivation of $CsPbBr_3$, resulting in synthesized NCs with a PLQY of up to 92.3% (Fig. 4b), demonstrating excellent colloidal stability[81]. Kar et al. combined the LARP method with zinc doping to produce $CsPbBr_3$ NCs with high stability and biocompatibility. Their experiments showed that, after zinc doping, the PLQY increased from 74% to 88%, and the luminescence intensity remained above 80% after soaking in polar solvents for 120 h[82]. Hu et al. successfully synthesized $CsPbX_3$ NCs with a PLQY of 85.2% in the LARP method by precisely controlling the reaction parameters. Through anion

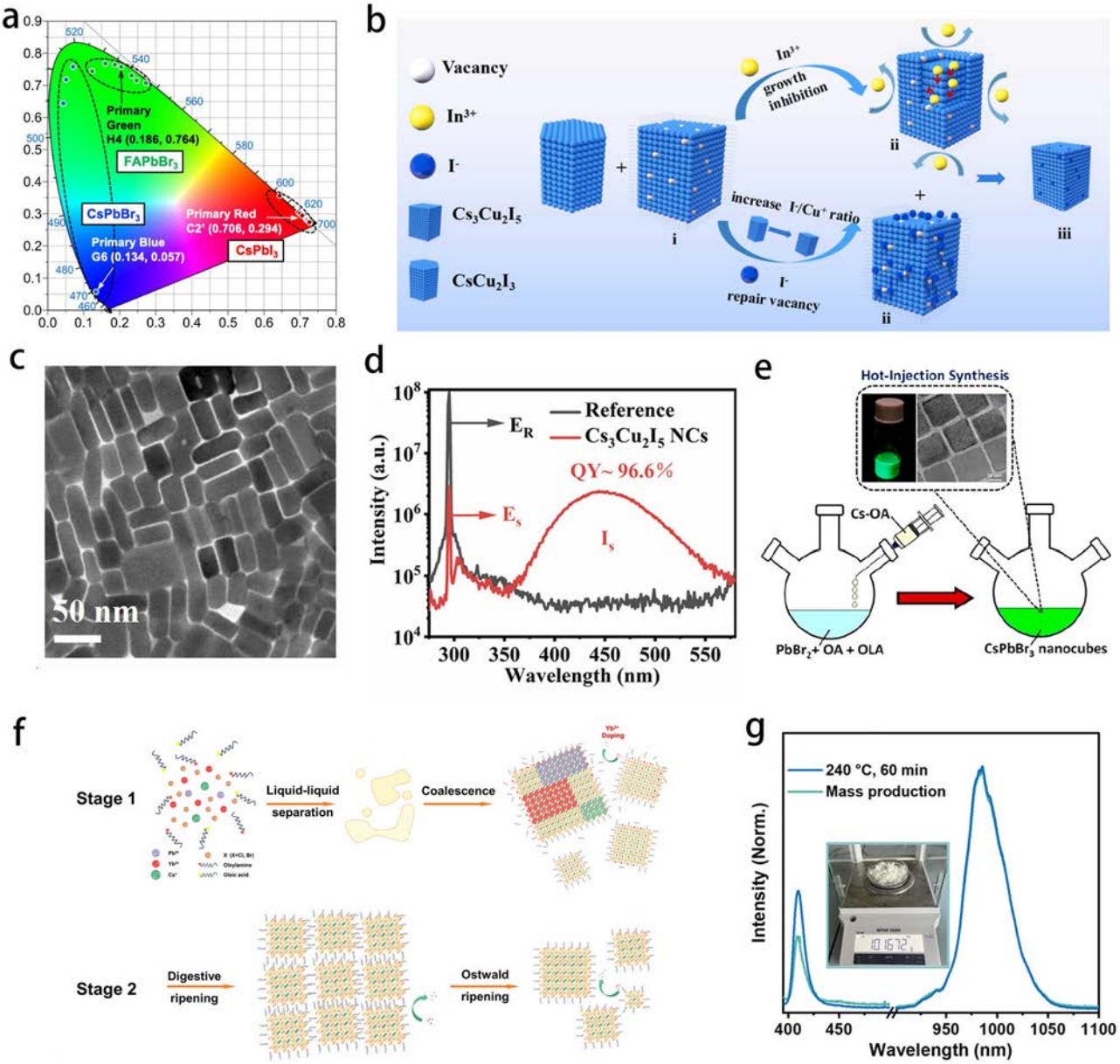

Fig. 2 | Hot injection method for synthesizing perovskite NCs. a The color coordinates of $CsPbI_3$, $CsPbBr_3$, and $FAPbBr_3$ NCs on the CIE1931 color diagram. **b** Schematic diagram of the growth mechanism of $Cs_3Cu_2I_5$ NCs assisted by InI_3. **c** TEM image of $Cs_3Cu_2I_5$ NCs. **d** PLQY of $Cs_3Cu_2I_5$ NCs synthesized with the assistance of InI_3. **e** Schematic diagram of $CsPbBr_3$ NCs synthesis via hot-injection method, with the inset showing a photo of $CsPbBr_3$ NCs solution under UV light and the HRTEM image of $CsPbBr_3$ NCs. **f** Schematic illustration of the one-pot heating synthesis method. **g** PL performance of Yb^{3+}:$CsPbCl_3$ NCs, with an inset showing a real sample weighing over 10 grams. **a** Reprinted under the terms of the Creative Commons CC-BY-NC-ND License from ref. 64; **b**–**d** Reproduced with permission from ref. 65. Copyright 2022, Elsevier; **e** Reproduced with permission from ref. 66. Copyright 2022, American Chemical Society; **f**, **g** Reproduced with permission from ref. 68. Copyright 2024, Royal Society of Chemistry.

exchange, they achieved a wide emission tunability range from 443.3 nm to 649.1 nm (Fig. 4c, d)[36]. Furthermore, in the study of lead-free perovskites, Chen et al. synthesized $FASnI_3$ NCs (Fig. 4e, f) in the LARP method using SnF_2 additives, improving the PLQY from 50% to 76%. Their research showed that SnF_2 effectively suppressed the oxidation of Sn^{2+} and enhanced the material's stability in air, with optical performance maintaining over 90% after 60 days[83]. These improvements in the LARP method provide new insights for preparing perovskite NCs.

Although the LARP method is widely employed for synthesizing $CsPbBr_3$ NCs, it encounters multiple challenges in preparing $CsPbI_3$ NCs. Polar solvents such as DMF accelerate the thermodynamic phase transition of $CsPbI_3$ from the photoactive black phase (α-phase) to the non-perovskite yellow phase (δ-phase)[84]. Additionally, the low migration energy barrier of I^- leads to uncontrolled nucleation rates. The solvent environment further induces iodine vacancy defects and promotes oxidation, undermining structural stability[85]. Moreover, the weak binding affinity of conventional ligands such as oleic acid and oleylamine to the $CsPbI_3$ surface exacerbates colloidal aggregation and phase degradation[86]. To address these challenges, strategies including surface ligand engineering, stabilizing additives, and optimization of solvent polarity have been explored to enhance the colloidal and structural stability of $CsPbI_3$ NCs synthesized via the LARP method[86–88]. Recent studies have shown that post-synthetic ligand exchange is an effective strategy for further improving the stability and optical performance of $CsPbI_3$ NCs. Among various options, thiol-containing ligands have demonstrated remarkable potential. Due to the strong affinity of thiol groups for lead ions on the perovskite surface, these ligands can form

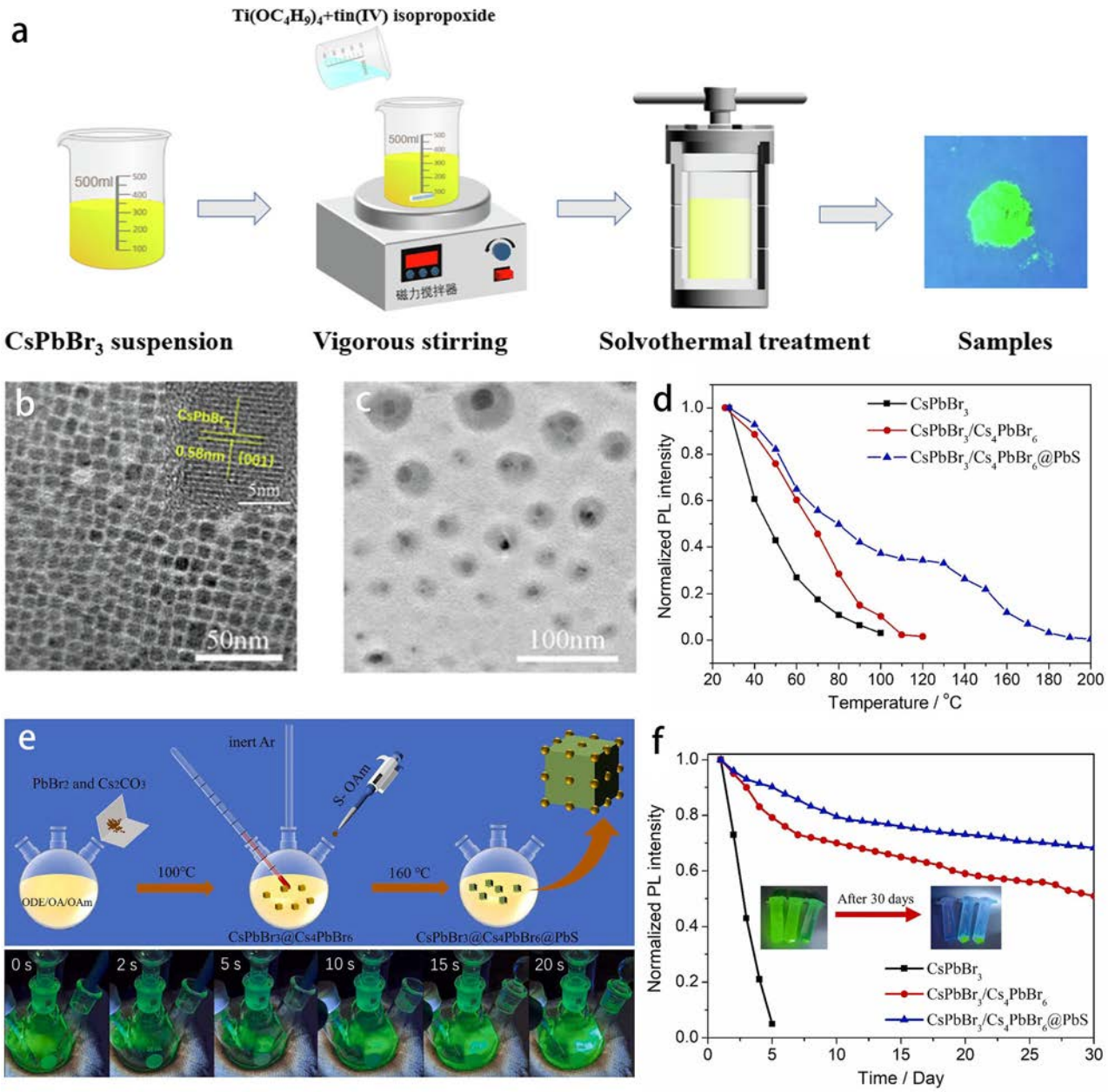

Fig. 3 | Solvothermal method for synthesizing perovskite NCs. a Schematic of the preparation process for $CsPbBr_3$/Sn-TiO_2 NCs. **b** TEM and HRTEM images of $CsPbBr_3$ perovskite QDs. **c** TEM image of the core-shell structure $CsPbBr_3$/Sn-TiO_2 NCs. **d** Temperature-dependent PL intensity curve of the sample. **e** Top: Schematic diagram of the synthesis of $CsPbBr_3/Cs_4PbBr_6$ NCs; bottom: photographs of the solution at different reaction times. **f** Time-dependent PL intensity curve of the sample. **a**–**c** Reproduced with permission from ref. 73. Copyright 2022, Elsevier; **d**–**f** Reproduced with permission from ref. 74. Copyright 2023, Elsevier.

stronger and more stable bonds than traditional carboxylic acid or amine ligands. This improved binding reduces surface trap states, increases the PLQY, and enhances environmental stability[89]. Ghorai et al. proposed the use of 1-dodecanethiol (DSH) as a post-synthetic repairing agent to successfully restore degraded α-$CsPbI_3$ NCs (Fig. 4g), thereby preventing their transition to the inactive δ-phase under ambient conditions. Through surface passivation and the removal of the degraded Cs_4PbI_6 phase, DSH restored the perovskite's cubic structure and significantly enhanced its PLQY and environmental stability[90]. This study highlights the unique role of thiol ligands in repairing "optically failed" perovskites and offers a new strategy for improving perovskite material performance.

Ultrasound-assisted and microfluidic method. The ultrasonic-assisted method is also an efficient and low-energy synthesis technique for producing perovskite NCs by adjusting through systematic modulation of ultrasonic parameters, including power intensity, frequency spectrum, and irradiation duration; this technique enables precise regulation of NCs dimensions and morphological features[91]. The underlying mechanism originates from the cavitation effect generated by ultrasonic waves propagating in a liquid medium, leading to the formation of microscopic bubbles; these bubbles rapidly expand and collapse, releasing localized high temperatures and high pressures; such extreme conditions accelerate the dissolution and nucleation of reactants while promoting their uniform dispersion, effectively preventing crystal aggregation and thus yielding NCs with uniform particle size and well-controlled morphology[92]. Compared to the conventional hot injection method, this approach is typically conducted at room or slightly elevated temperatures without requiring high pressure or complex equipment. These mild reaction conditions help prevent thermal degradation of the material, thereby enhancing its stability[93]. Jiang et al. used a one-step

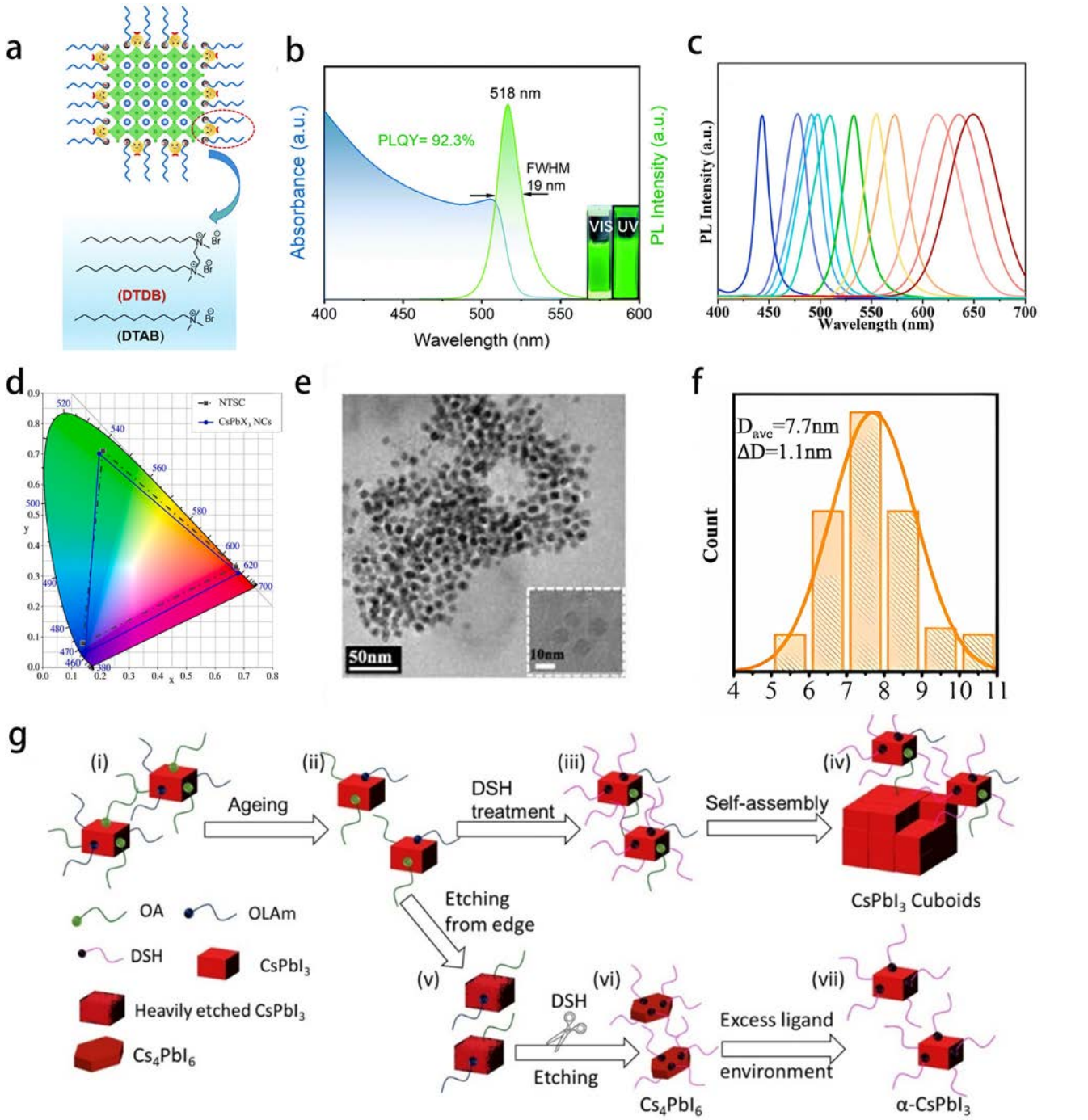

Fig. 4 | The LARP method for synthesizing perovskite NCs. a Schematic illustration of the interaction between $CsPbBr_3$ NCs and the DTDB ligand, along with the chemical structure of the DTDB ligand. **b** UV-vis absorption and PL spectra of DTDB-$CsPbBr_3$ NCs, with the inset showing colloidal solutions under sunlight and 365 nm UV light. **c** PL spectra of $CsPbX_3$ NCs. **d** Color gamut of $CsPbX_3$ NCs. **e** TEM image of $FASnI_3$-6%SnF_2 NCs. **f** Size distribution histograms of $FASnI_3$-6%SnF_2 NCs. **g** Schematic Diagram of the Mechanism by Which DSH Restores Degraded α-$CsPbI_3$. **a**, **b** Reproduced with permission from ref. 81. Copyright 2022, Royal Society of Chemistry; **c**, **d** Reproduced with permission c[36]. Copyright 2022, Elsevier. **e**, **f** Reproduced with permission from ref. 83. Copyright 2023, AIP Publishing; **g** Reproduced with permission from ref. 90. Copyright 2023, Elsevier.

ultrasonic method to prepare a variety of ion-doped $CsPbX_3$ NCs (Fig. 5a) and studied the effects of ion doping on perovskite NCs. Experimental results showed that Sr doping significantly improved the phase stability of $CsPbI_3$ NCs, while Ni doping in $CsPbCl_3$ NCs increased the PLQY from 10.1% to 71% (Fig. 5b). Mn doping in $CsPbCl_3$ NCs resulted in dual-color emission at 406 nm and 580 nm, indicating that ion doping can effectively improve the optical properties and stability of $CsPbX_3$ NCs[94]. Dou et al. used high-power ultrasound to synthesize $FAPbX_3$ NCs. Their research showed that high-power ultrasound significantly reduced issues of uneven stirring and high-temperature instability in traditional methods, ensuring a uniform nanoparticle size distribution. By adjusting the halide composition, they achieved a PL spectrum with emission wavelengths ranging from 453 to 695 nm and a PLQY as high as 93% (Fig. 5c, d)[95].

Recently, microfluidic synthesis methods have garnered significant attention for preparing $CsPbX_3$ NCs due to their superior control over reaction parameters, enhanced reproducibility, and minimal precursor

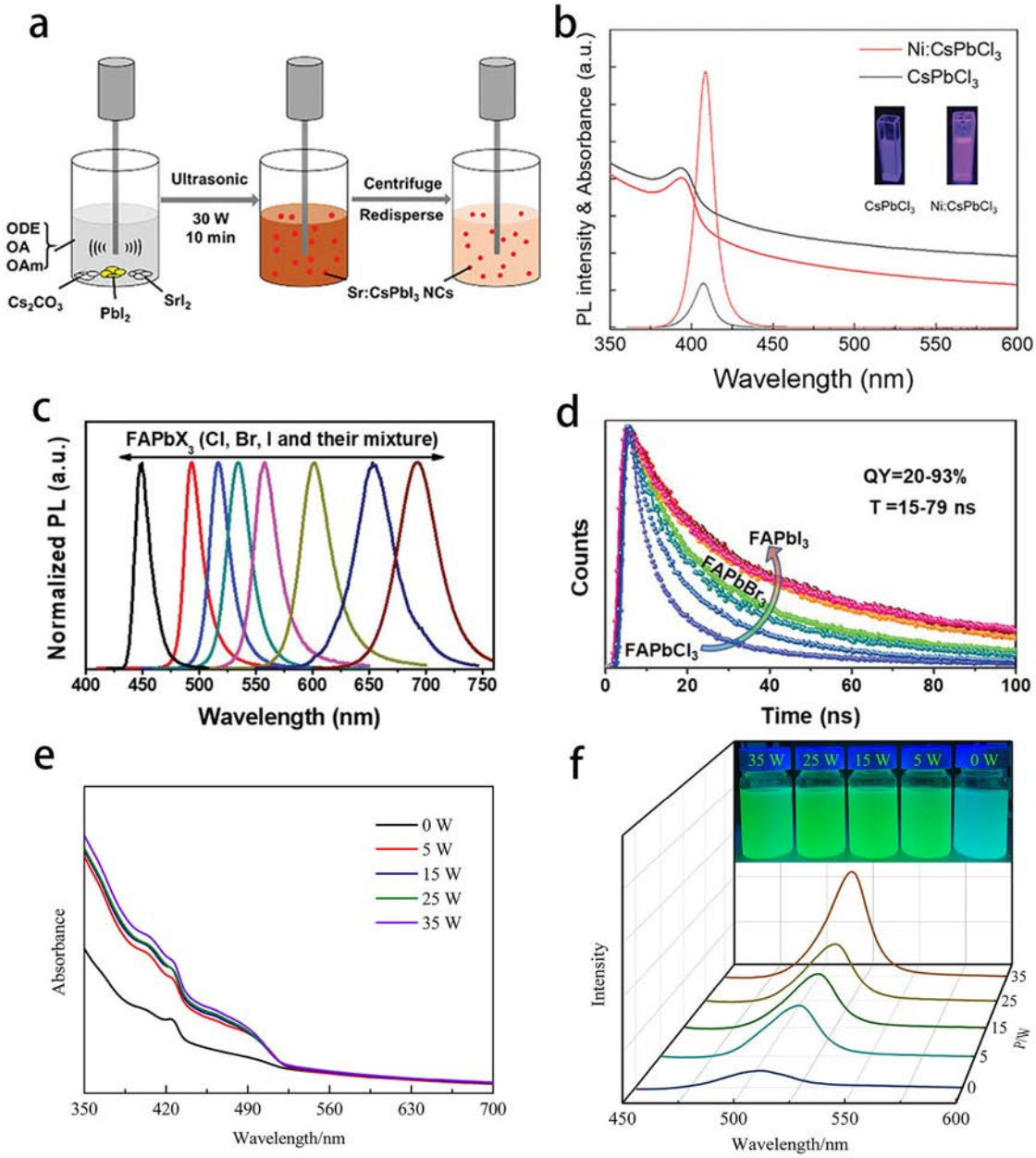

Fig. 5 | Ultrasound-assisted and microfluidic method for synthesizing perovskite NCs. a Schematic diagram of the process for synthesizing Sr:$CsPbI_3$ NCs via a one-step ultrasonic method. **b** PL and absorption spectra of $CsPbCl_3$ and Ni:$CsPbCl_3$ NCs. The inset shows a photo of the NC solution under UV illumination. **c** PL spectra of $FAPbX_3$ NCs with different halide compositions. **d** Evolution of PL time-resolved decay and PLQY. **e**, **f** UV-visible absorption spectra and PL emission spectra of $CsPbBr_3$ NCs synthesized under different ultrasonic powers. **a**, **b** Reproduced with permission from ref. 94. Copyright 2023, John Wiley and Sons; **c**, **d** Reproduced with permission from ref. 95. Copyright 2020, John Wiley and Sons; **e**, **f** Reproduced with permission from ref. 100. Copyright 2022, Elsevier.

consumption[96]. Unlike traditional batch synthesis, microfluidic reactors provide a highly controlled environment for nucleation and growth, leading to uniform NCs size and tunable optical properties[97]. This technique also enables continuous production, which is critical for practical applications. Abdel-Latif et al. reported a method for rapid halide ion exchange in perovskite QDs at room temperature, utilizing a modular microfluidic platform, the QDs Exchanger, which enables precise control and real-time monitoring of the ion exchange process[98]. This method provides a new approach for efficient bandgap tuning and QD performance optimization. In further research, Jha et al. proposed a new method for bandgap tuning of perovskite QDs through photo-induced halide exchange reaction, utilizing an automated microfluidic platform combined with a single-droplet photoflow reactor, which significantly improves the reaction rate and material efficiency[99]. In addition, Li et al. used an ultrasonic cavitation-enabled microfluidic approach to prepare $CsPbBr_3$ NCs continuously under low-temperature conditions. Adjusting the ultrasound power and mixing time effectively solved the problem of uneven particle size caused by poor mixing in batch reactions. The synthesized $CsPbBr_3$ NCs exhibited significantly enhanced light absorption and PL intensity (Fig. 5e, f), and the NCs were smaller in size[100]. Compared to traditional batch reaction methods, the ultrasonic cavitation-enabled microfluidic approach demonstrated significant advantages in experimental reproducibility and the optical performance of the NCs, providing a new technological pathway for large-scale, high-efficiency synthesis of high-quality perovskite NCs.

Optoelectronic applications

Light-emitting diodes. Halide perovskite QDs and NCs have demonstrated tremendous potential in LED applications due to their exceptional

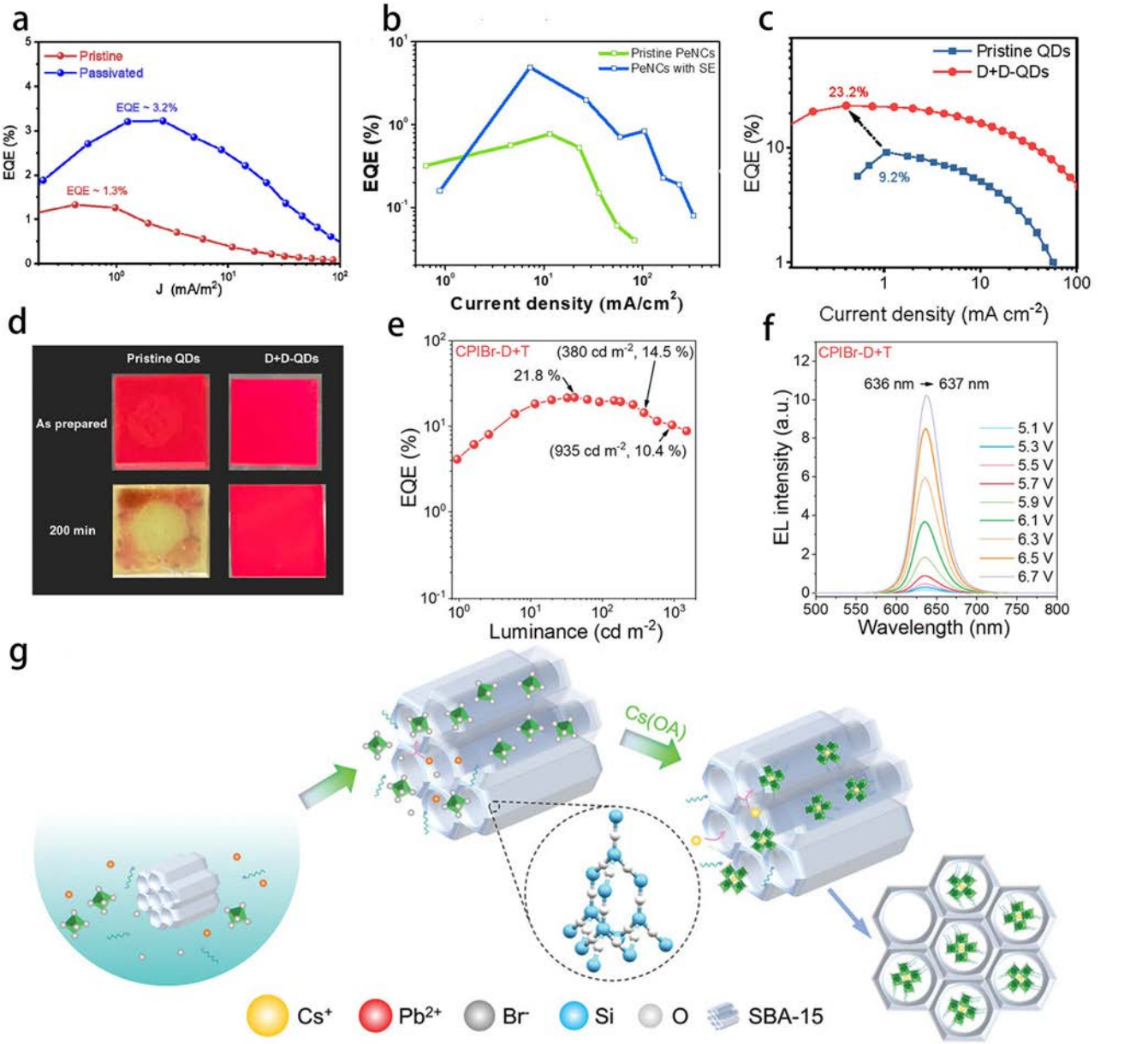

Fig. 6 | Application of perovskite NCs in LEDs. a EQE of LEDs at different current densities. **b** EQE of LEDs after BF^{4-} passivation and under normal conditions. **c** EQE of LEDs with D + D-QD and original QDs. **d** Photos of original QDs and D + D-QD films under 365 nm UV light excitation at different times. **e** EQE versus brightness curve. **f** EL spectra as the applied voltage increases from 5.1 to 6.7 V. **g** Schematic diagram of in-situ synthesis of $CsPbBr_3$/SBA-15 composites. **a** Reproduced with permission from ref. 109. Copyright 2024, American Chemical Society; **b** Reproduced with permission from ref. 110. Copyright 2022, Elsevier; **c, d** Reproduced with permission from ref. 111. Copyright 2024, American Chemical Society; **e, f** Reproduced with permission from ref. 112. Copyright 2023, John Wiley and Sons; **g** Reproduced with permission from ref. 113. Copyright 2023, John Wiley and Sons.

optoelectronic properties, including narrow emission spectra, tunable bandgaps, and high PLQY[101–103]. However, their practical application is hindered by challenges such as poor spectral stability, ion migration, and insufficient environmental stability[104]. To address these issues, recent research has proposed various optimization strategies, including doping engineering, surface passivation, and structural design[105,106].

For blue perovskite LEDs, optimizing stability and efficiency remains a significant challenge in current research[107]. Ye et al. successfully fabricated pure blue perovskite LEDs with stable electroluminescence (EL) spectra by co-doping copper and potassium ions into mixed-halide perovskite QDs. Their study demonstrated that even at a high current density of 1617 mA/cm^2, the emission spectrum remained stable at 469 nm, indicating that the synergistic doping of copper and potassium effectively suppressed halide migration and reduced non-radiative recombination. The optimized device achieved an EQE of 2.0% and an average luminance of 393 cd/m^2[,108]. Similarly, Chen et al. proposed a tetrafluoroborate passivation strategy to enhance the spectral stability of blue perovskite LEDs by passivating the surface of $CsPbBr_xCl_{3-x}$ NCs and filling halide vacancies. This technique significantly inhibited halide migration, resulting in blue LEDs with an emission wavelength of 468 nm, a maximum luminance of 275 cd/m^2, and an EQE of 3.2% (Fig. 6a)[109]. Baek et al. further improved the performance of blue perovskite LEDs by introducing pseudohalide (SCN^-) to passivate chloride vacancies and replacing traditional long-chain ligands with short octylphosphonic acid (OPA) and 3,3-diphenylpropyl amine (DPPA). This approach effectively addressed the low quantum efficiency caused by chloride vacancies and the high resistance associated with long-chain organic ligands in mixed-halide perovskite QDs. As a result, their blue perovskite

LEDs achieved an EQE of 4.9% (Fig. 6b) with a maximum luminance of 1874 cd/m^2[110].

In red LEDs, ion migration and spectral stability are major obstacles to performance enhancement. Zhou et al. proposed a synchronous post-treatment strategy that involved polishing the lead-rich surface of QDs using the chelating agent 1,4,7,10-tetraazacyclododecane-1,4,7,10-tetraacetic acid hydrate (DOTA) while passivating surface defects with 2,3-dimercapto-succinic acid molecules. This approach effectively reduced halide migration and non-radiative recombination, leading to pure red perovskite LEDs with an EQE of 23.2% (Fig. 6c, d)[111]. Xie et al. further optimized the stability of red perovskite QDs by replacing conventional long-chain ligands with 1-dodecanethiol (1-DT). The strong binding of 1-DT to the QD's surface significantly suppressed halide migration, resulting in a device that exhibited pure red emission at 637 nm with an EQE of 21.8% (Fig. 6e) and a peak luminance of 2653 cd/m^2. Additionally, at a high voltage of 6.7 V, the EL spectrum of the device remained stable (Fig. 6f)[112].

Perovskite QD LEDs emitting at wavelengths beyond red and blue have also garnered significant attention. Fan et al. employed an in-situ growth strategy to embed perovskite QDs into mesoporous silica (SBA-15) (Fig. 6g). The ordered mesoporous structure of SBA-15 reduced light reabsorption among QDs via a waveguiding effect, significantly lowering the non-radiative recombination rate while enhancing light emission intensity and stability. The LED fabricated using the $CsPbBr_3$/SBA-15 composite achieved green light emission at 520 nm, with a maximum luminous efficiency of 183 lm/W. Furthermore, a white LED was constructed by integrating a commercial blue LED (460 nm) with green-emitting ($CsPbBr_3$/SBA-15) and red-emitting ($CsPb(Br_{1-x}/I_x)_3$/SBA-15) composites, demonstrating a luminous efficiency of 116 lm/W. The color gamut coverage of this white LED notably surpassed that of conventional phosphor-based systems[113]. Fang et al. developed a strategy using 4-dodecylbenzenesulfonic acid (DBSA) to regulate the crystallization process of perovskite QDs. This approach suppressed halide vacancies and interstitial defects, significantly increasing the migration activation energy of QDs. The study revealed that the LED devices fabricated with the optimized Perovskite QDs exhibited green light emission at 522 nm, achieved an EQE of 20.4%, and demonstrated an operational lifetime exceeding 100 hours[114].

Solar cells. Halide perovskite NCs exhibit significant potential in solar cell applications due to their excellent light absorption capability, tunable bandgap, and high photovoltaic conversion efficiency; their outstanding optoelectronic properties and low-cost fabrication processes make them important candidates for next-generation photovoltaic materials[115,116]. The lead-free perovskite Cs_2AgBiI_6 has gained attention due to its environmentally friendly characteristics and higher thermal stability. Liu et al. were the first to fabricate solar cells based on hexagonal Cs_2AgBiI_6 NCs. They found the Cs_2AgBiI_6 NCs had a bandgap of 2.29 eV, exhibiting a high absorption coefficient and a narrow PL peak. Furthermore, Cs_2AgBiI_6 NC films demonstrated good stability under thermal, humidity, and light exposure conditions. However, the photovoltaic conversion efficiency of the solar cells was only 0.076% (Fig. 7a, b), which is far below that of current mainstream lead-based perovskite materials[117]. This result indicates that although lead-free perovskites have potential in environmentally friendly solar cells, their optoelectronic performance still needs optimization. To address the surface defect issues of perovskite NCs, Song et al. used deprotonated cysteine (Cys-S$^-$) as a ligand to passivate the surface of $CsPbI_3$ NCs (Fig. 7c). The results showed that this method effectively passivated surface iodine vacancies and significantly improved the performance of the perovskite NCs. The study indicated that thiol salt ligands have a much stronger binding affinity for iodine vacancies on the surface of $CsPbI_3$ NCs than traditional carboxylate ligands, effectively repairing surface defects. With this surface passivation treatment, solar cells based on the material achieved a power conversion efficiency (PCE) of 15.5% (Fig. 7d). After two months of testing under conventional environmental conditions, they still retained 77% of their initial PCE (Fig. 7e)[118]. In further research, Wang et al. introduced a short-chain ligand, 2-methoxyphenylethylammonium iodide (2-MeO-PEAI), to in situ modify $CsPbBr_3$ perovskite NCs. Through halide exchange, $CsPbBr_3$ was induced to transition from the cubic phase to the Ruddlesden-Popper phase (RPP). The synergistic passivation of the RPP NCs and 2-MeO-PEA$^+$ inhibited surface defects and improved the stability of the NCs. The study showed that perovskite solar cells modified with 2-MeO-PEAI achieved the highest PCE of 24.39% (Fig. 7f). Moreover, the device retained 80% of its initial PCE after continuous illumination for 340 h. Still, it maintained 94% of its initial efficiency after being stored for 3000 h in a nitrogen atmosphere in the dark[119].

Recent studies have found that perovskite NC heterojunction technology could significantly enhance the performance of solar cells[120]. Wieliczka et al. investigated the construction of perovskite NC heterojunctions and proposed a layer-by-layer deposition technique using non-polar solvents. This method allows for the deposition of perovskite NCs without damaging the underlying perovskite film, resulting in heterostructures with highly tunable optoelectronic properties. The research showed that these perovskite NCs heterojunctions significantly improved charge separation and transport efficiency, thus enhancing PCE[121]. However, further improving photovoltaic efficiency remains challenging due to the susceptible surface and inevitable vacancies of perovskite NCs. As a result, core-shell structures have become one of the key strategies to enhance the performance of perovskite NCs. Goldreich et al. coated $CsPbBr_3$ NCs with MoS_2 to construct a core-shell structure (Fig. 7g, h), which improved light absorption and significantly enhanced the material's stability under humidity and thermal conditions. The study showed that $CsPbBr_3$@MoS_2 core-shell nanostructures exhibited much greater stability in polar solvents. While $CsPbBr_3$ NCs decompose in water within just a few minutes, $CsPbBr_3$@MoS_2 remained stable for over a week. Regarding photovoltaic performance, the short-circuit current (J_{sc}) of $CsPbBr_3$@MoS_2 was 220% higher than that of pure $CsPbBr_3$ devices[122].

Photodetectors. 0D halide perovskites have attracted widespread attention in the field of photodetectors due to their excellent optoelectronic properties and good material tunability, showing great potential in enhancing the responsivity, detectivity, and stability of photodetectors[123,124]. Patra et al. proposed an amine-free hot injection method for synthesizing $CsPbBr_3$ NCs, using 1,3-dibromopropane (DBP) as the halogen source. The synthesized NCs exhibited an extremely high PLQY (98.5%). Photodetectors based on these QDs demonstrated ultrafast photodetection capability with rise/fall times of 104/35 μs (Fig. 8a) while maintaining good environmental stability[125]. Sulaman et al. developed a composite material of PbSe QDs and mixed halide perovskite $CsPbBr_{1.5}I_{1.5}$ NCs. They created a self-powered photodetector with the structure ITO/ZnO/PbSe:$CsPbBr_{1.5}I_{1.5}$/P3HT/Au. By using ZnO and P3HT as electron and hole extraction layers, they successfully enhanced the transport efficiency of photo-generated charge carriers. They reduced the loss from non-radiative recombination, significantly improving the optoelectronic performance of the photodetector. This device achieved a responsivity of 6.16 A/W at a wavelength of 532 nm, a detectivity as high as 5.96×10^{13} Jones (Fig. 8b, c), and exhibited a good on/off current ratio. However, the poor environmental stability of PbSe QDs limits their application range[126].

To further optimize device structures for enhanced performance, Jeong et al. designed a 0D-2D heterojunction photodetector by integrating $CsPbI_3$ QDs with multilayer MoS_2. The built-in electric field improved the separation efficiency of photogenerated carriers, resulting in a detectivity of 10^{13} Jones. Although this structure significantly enhanced optoelectronic performance through energy level matching at the material interface, its complex fabrication limited its potential for large-scale production[127]. Yang et al. investigated a high-performance self-powered photodetector combining $CsPbBr_3$ QDs with the organic semiconductor PQT-12 (poly(3,3"-didodecyl-quarterthiophene)). The device exhibited a detectivity as high as 5.8×10^{12} Jones and a light-to-dark current ratio of 10^5 in self-powered mode (Fig. 8d, e). Additionally, it demonstrated a clear photoresponse to weak

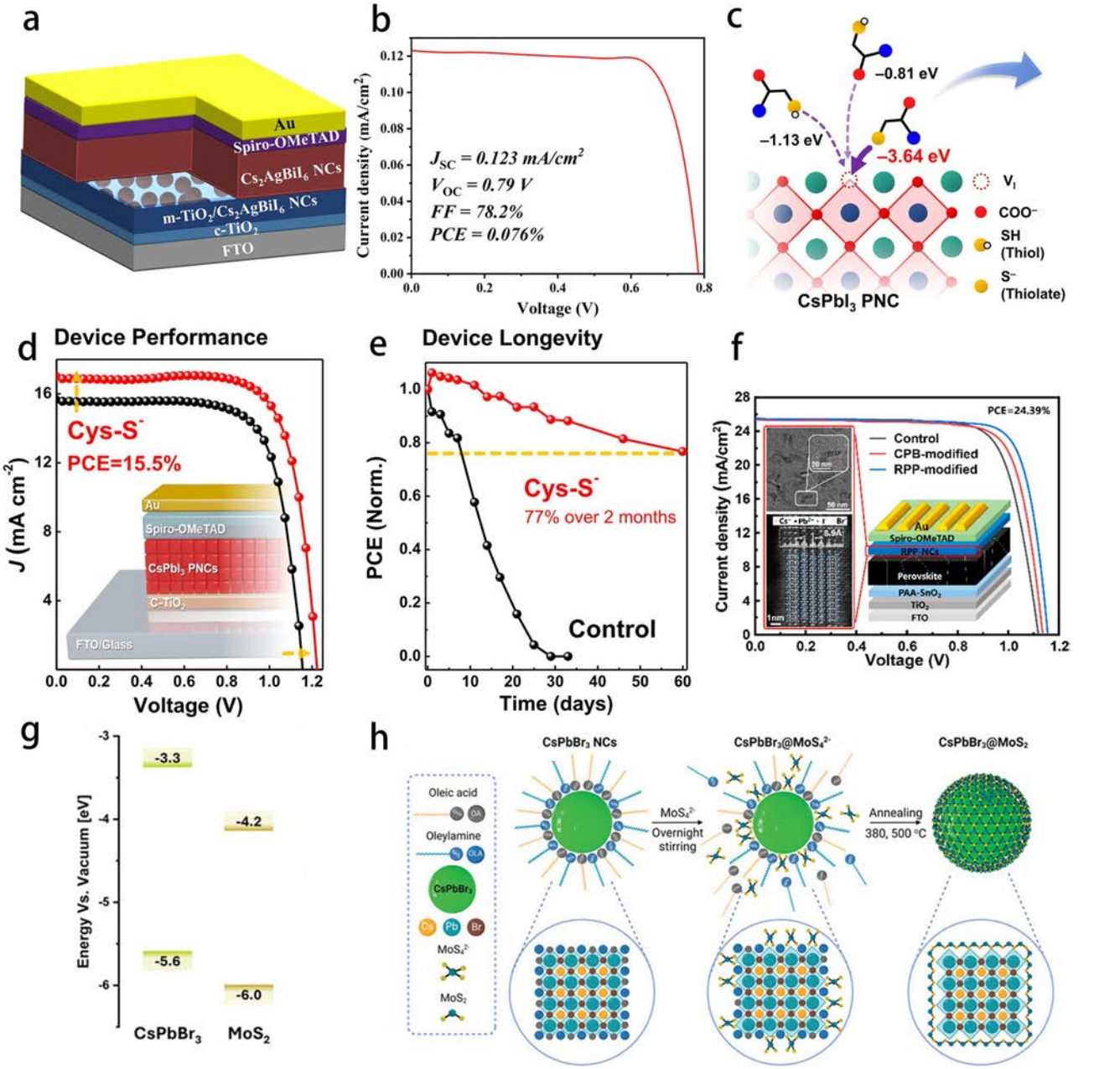

Fig. 7 | Application of perovskite NCs in solar cells. **a** Schematic diagram of the device structure FTO/c-TiO_2/mTiO_2/Cs_2AgBiI_6/ Spiro-OMeTAD/Au. **b** Current density-voltage (J-V) characteristics of the best device. **c** Schematic diagram of the interaction between cysteine and the surface of NCs. **d** Schematic diagram of the device structure and its J-V characteristics. **e** Data plot showing the variation in device PCE over time. **f** Schematic diagram of the PSC structure with in-situ modified RPP NCs and its (J-V) characteristics. **g** Schematic diagram of the interface energy levels of $CsPbBr_3$/MoS_2. **h** Schematic diagram of the reaction mechanism of $CsPbBr_3$@MoS_2 at different synthesis stages. **a**, **b** Reproduced with permission from ref. 117. Copyright 2023, American Chemical Society; **c**–**e** Reproduced with permission from ref. 118. Copyright 2022, Elsevier; **f** Reproduced with permission from ref. 119. Copyright 2024, American Chemical Society; **g**, **h** Reproduced with permission from ref. 122. Copyright 2024, John Wiley and Sons.

light intensities as low as 3 nW cm^{-2}, indicating its superior performance in low-light environments[128]. Wei et al. reported a vertically structured photodetector with the configuration of Si^{++}/SiO_2/Au/monolayer graphene/$CsPbI_3$ QDs (Fig. 8f). Leveraging the Frenkel-Poole emission effect induced by the high trap-state density within the SiO_2 layer, the device exhibited significantly enhanced carrier transport and separation efficiency. It achieved a remarkable responsivity of 2319 A/W and a detectivity of 1.15×10^{14} Jones at a wavelength of 365 nm, demonstrating outstanding performance in ultraviolet photodetection[129].

To enhance the stability of QDs, Moon et al. passivated $CsPbBr_3$ QDs using a quaternary ammonium ligand, didodecyl dimethyl ammonium bromide (DDAB). This passivation reduced surface defects, effectively suppressed non-radiative recombination, and extended the carrier lifetime. The passivated QDs exhibited an average carrier lifetime of 14.88 ns. A 2D-0D hybrid photodetector was fabricated by depositing DDAB-capped QDs onto a WSe_2 thin film, achieving a responsivity of 1.4×10^3 A/W and a detectivity of 3.1×10^{13} Jones under a 405 nm laser illumination at 40.0 μW cm^{-2}. Furthermore, the DDAB-passivated QDs demonstrated excellent water stability, with only a 25.8% loss in PL intensity after 16 hours of water exposure. This highlights the potential of quaternary ammonium ligands in reducing surface defect states and improving material stability[130]. Saleem et al. introduced a simple ligand

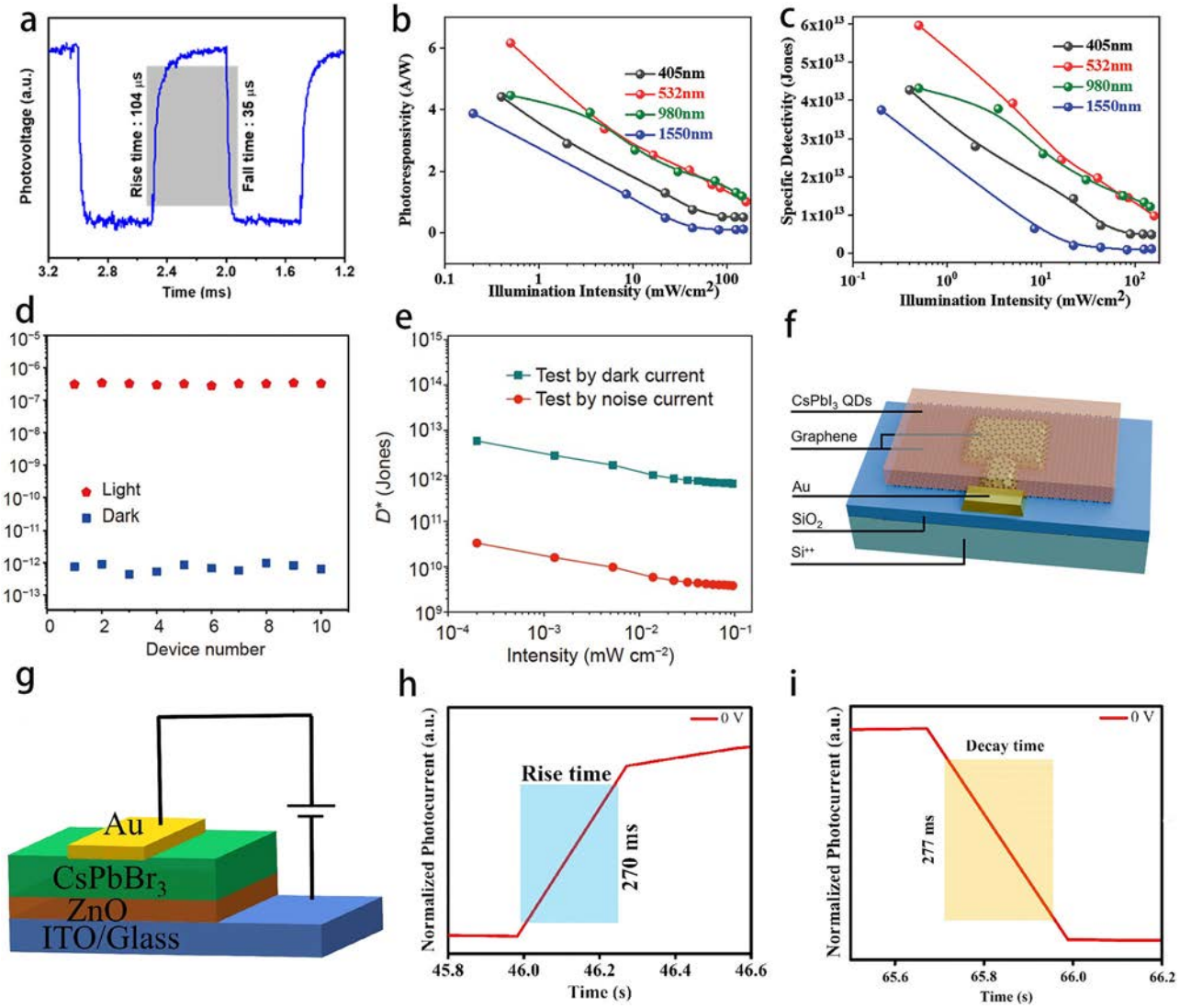

Fig. 8 | Application of perovskite NCs in photodetectors. **a** Rise and fall times of the $CsPbBr_3$ QD photodetector. **b**, **c** Dependence of photodetector responsivity and detectivity on light intensity under illumination at different wavelengths. **d** Dark and photocurrent measurements of ten batch-fabricated self-powered photodetectors. **e** Detectivity of the photodetector was measured using different methods. **f** Schematic illustration of the Si^{++}/SiO_2/Au/graphene/$CsPbI_3$ QD device. **g** Schematic diagram of the heterojunction photodetector based on the ITO/ZnO/$CsPbBr_3$-CsBr/Au structure. **h**, **i** Rise time and decay time of the device at 0 V. **a** Reproduced with permission from ref. 125. Copyright 2024, American Chemical Society; **b**, **c** Reproduced with permission from ref. 126. Copyright 2022, John Wiley and Sons; **d**, **e** Reproduced with permission from ref. 128. Copyright 2022, Springer Nature; **f** Reproduced with permission from ref. 129. Copyright 2024, American Chemical Society; **g**, **h**, **i** Reproduced with permission from ref. 131. Copyright 2023, John Wiley and Sons.

exchange method by rinsing $CsPbBr_3$ NCs films with an excess CsBr solution. This process effectively reduced mid-gap trap states and suppressed non-radiative recombination. A photodetector based on the ITO/ZnO/$CsPbBr_3$-CsBr/Au structure (Fig. 8g) exhibited a responsivity of 6.38 A/W and a detectivity of 2.6×10^{13} Jones, along with a fast response time of 270/277 ms (Fig. 8h, i)[131]. This technique effectively addressed surface defect issues in QDs and enhanced device stability.

Other applications. Compared to 2D and 3D perovskite materials, 0D perovskite NCs exhibit more pronounced quantum effects, leading to higher optical gain, lower lasing thresholds, and longer carrier lifetimes in laser applications; these advantages make 0D perovskite NCs an ideal gain medium for next-generation lasers[132,133]. Lu et al. integrated $MAPbBr_3$ NCs with titanium nitride (TiN) plasmonic nanocavities to achieve a low-threshold upconversion plasmonic laser (Fig.9a). The TiN plasmonic nanocavity enhanced both the absorption of pump photons and the upconversion photon emission rate. Under 800 nm laser excitation at a cryogenic temperature of 6 K, a single-mode upconversion lasing emission was successfully realized, with a lasing peak at 554 nm (Fig. 9b) and an ultralow threshold of 10 μJ/cm^2. Additionally, this laser exhibited an extremely small mode volume (~ 0.06 λ^3), highlighting its potential for ultra-compact size, low power consumption, and fast switching times in practical applications[134]. In another study, Xie et al. demonstrated a solution-processed $CsPbBr_3$ NCs-based laser by integrating it with silica microspheres (Fig. 9c). This hybrid system successfully enabled a low-threshold, spectrally tunable whispering-gallery-mode (WGM) laser, achieving a lasing threshold as low as approximately 3.1 μJ/cm^2 (Fig. 9d) with a cavity quality factor of 1193. Furthermore, long-term laser excitation tests (>10^7 laser pulses) confirmed the exceptional stability of this laser at room temperature, surpassing that of most conventional NC-based lasers[135]. In summary, these studies highlight the outstanding optical properties of perovskite NCs and validate their potential in laser applications through various laser designs.

Halide perovskite NCs have emerged as core materials in sensor research due to their exceptional optoelectronic properties; sensors based on perovskite NCs not only exhibit high sensitivity and rapid response capabilities but also demonstrate significant potential for environmental

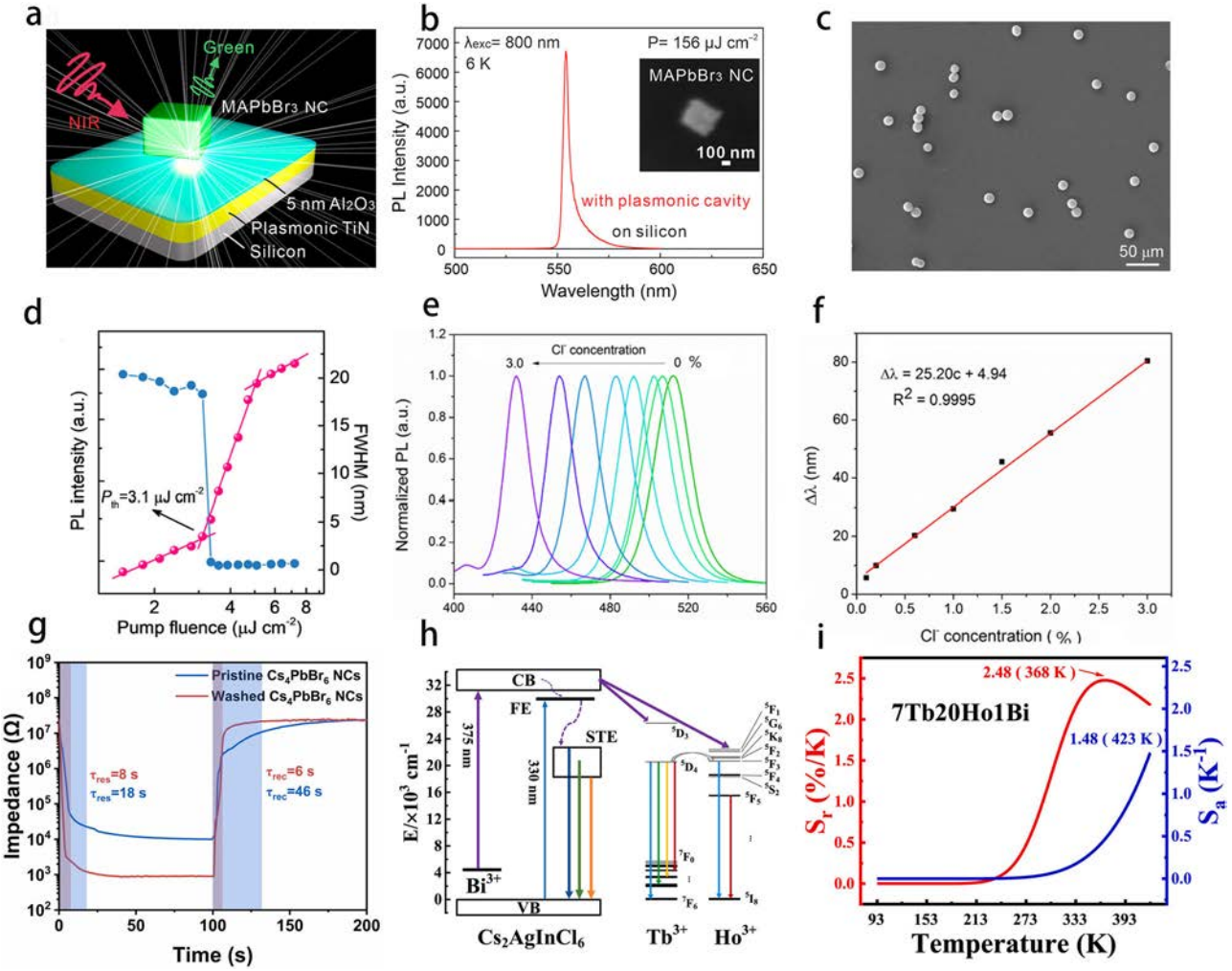

Fig. 9 | Application of perovskite NCs lasers and sensors. a Schematic diagram of the $MAPbBr_3$ NCs-based laser device. **b** PL emission spectrum of the laser under 800 nm laser excitation. **c** Typical SEM image of silica microspheres coated with $CsPbBr_3$ NCs on a glass substrate. **d** Emission intensity and linewidth of the dominant emission peak as a function of pump fluence. **e** Fluorescence spectra of chloride solutions with concentrations ranging from 0 to 3.0% under 365 nm UV excitation. **f** Working curve illustrating the fluorescence wavelength shift of chloride detection in the concentration range of 0-3.0%. **g** Response and recovery curves of pristine Cs_4PbBr_6 NCs and washed Cs_4PbBr_6 NCs. **h** Schematic of the luminescence mechanism in co-doped $Cs_2AgInCl_6$ NCs. **i** S_a and S_r values for $Cs_2AgInCl_6$ NCs co-doped with 7% Tb^{3+}, 20% Ho^{3+}, and 1% Bi^{3+}. **a**, **b** Reproduced with permission from ref. 134. Copyright 2021, American Chemical Society; **c**, **d** Reproduced with permission from ref. 135. Copyright 2021, IOP Publishing; **e**, **f** Reprinted under the terms of the Creative Commons CC-BY License from ref. 138; **g** Reproduced with permission from ref. 139. Copyright 2024, Elsevier; **h**, **i** Reproduced with permission from ref. 140. Copyright 2024, Elsevier.

stability and long-term applications[136,137]. Li et al. synthesized a $CsPbBr_3$@SiO_2 perovskite NC composite ($CsPbBr_3$@SiO_2 PNCCs) and employed a halide exchange strategy to determine the Cl^- concentration in marine sand samples. Through uniform halide exchange between sodium chloride solution and$CsPbBr_3$@SiO_2 PNCCs, the PL wavelength of the composite shifted from 447 nm to 506 nm, with the corresponding PL color changing from green to blue, reflecting variations in Cl^- concentration (Fig. 9e). Furthermore, a linear relationship was established between the PL wavelength and Cl^- concentration (0–3.0%) (Fig. 9f), demonstrating the effectiveness of this method in Cl^- concentration measurement in marine sand samples[138]. Liu et al. reported a high-performance humidity sensor based on fully inorganic Cs_4PbBr_6 NCs. Their study revealed that bromine vacancies in Cs_4PbBr_6 NCs serve as active sites that enhance water molecule adsorption, significantly improving humidity sensing performance. The sensor exhibited a response exceeding four orders of magnitude across a humidity range of 11% to 98% relative humidity, with rapid response and recovery times of 8 s and 6 s (Fig. 9g). Additionally, this humidity sensor demonstrated outstanding selectivity, reproducibility, and long-term stability, showing great potential for applications in respiratory monitoring and non-contact switching[139]. Wu et al. explored the temperature sensing applications of Tb^{3+}/Ho^{3+}/Bi^{3+} co-doped lead-free double perovskite $Cs_2AgInCl_6$ NCs (Fig. 9h). Using a hot-injection method, Tb^{3+}, Ho^{3+}, and Bi^{3+} were successfully incorporated into $Cs_2AgInCl_6$ NCs, and the fluorescence intensity ratio (FIR) technique was used to analyze the effect of temperature on emission spectra. The study found that $Cs_2AgInCl_6$ NCs co-doped with 7% Tb^{3+}, 20% Ho^{3+}, and 1% Bi^{3+} exhibited excellent temperature sensing performance, with an absolute sensitivity (S_a) of 1.48 K^{-1} and a relative sensitivity (S_r) of 2.48% K^{-1} (Fig. 9i)[140]. This study provides new insights into the potential application of lead-free double perovskite NCs in non-contact temperature measurement.

It is worth mentioning that perovskite NCs also have broad applications in color display. Park et al. proposed an interactive deformable colored sound display based on electrostrictive fluoropolymer and perovskite materials. In terms of color display, electroluminescent microparticles (ZnS:Cu) were mixed with a fluoropolymer to form a composite layer, which emits blue light when an alternating electric field is applied. Meanwhile, the perovskite NC films ($CsPbBr_3$ and $CsPbI_3$) convert the blue light into red and green light, enabling color modulation[28]. This study breaks through the low-voltage and multi-color bottleneck of flexible optoacoustic devices, providing a new platform for human-machine interaction.

One-dimensional nanostructure

Properties and advantages

1D halide perovskites include key types such as NWs and NRs. These materials have attracted extensive attention in optoelectronics due to their unique structural characteristics and excellent light absorption capabilities, particularly in visible and near-infrared regions[25,141,142]. Compared to 0D materials, 1D perovskites possess a broader absorption range and can convert absorbed light energy into electrical current more efficiently, significantly enhancing the photoelectric conversion efficiency[143,144]. This property originates from their unique chain-like structure, where corner-sharing $[BX_6]^{4-}$ octahedra extend along the 1D direction, forming a structure that facilitates efficient charge transport[145]. Due to the confinement of the 1D structure, the movement direction of charge carriers is effectively controlled, leading to highly efficient charge carrier transport and superior charge mobility in optoelectronic devices[146]. Furthermore, the weak van der Waals interactions between chains in the 1D structure significantly reduce defect state density and suppress non-radiative recombination processes, further optimizing optoelectronic performance and enhancing device stability[147].

In terms of environmental stability, 1D perovskite NWs exhibit strong moisture resistance and thermal stability, primarily due to the role of large organic cations as spatial isolation units; through hydrophobic effects and hydrogen bonding interactions, organic cations effectively prevent the infiltration of water and oxygen, thereby enhancing the material's stability under various environmental conditions[148,149]. This is of critical importance for their practical applications in optoelectronic devices. Notably, the optoelectronic properties and mechanical performance of 1D perovskite NWs can be precisely tuned by adjusting their dimensions, halide composition, and the type of organic cations[150,151]. By modifying the halide composition (Cl^-, Br^-, I^-), the bandgap can be tailored to cover a spectral range from visible to near-infrared[152]. Additionally, controlling the diameter and length of NWs allows for the modulation of their optical response characteristics, further optimizing their performance in optoelectronic devices[153]. This tunability grants 1D perovskite NWs extensive adaptability across multiple application domains, particularly demonstrating immense potential in optoelectronics.

Synthesis methods

Chemical vapor deposition. CVD has become one of the important methods for synthesizing halide perovskite NWs due to its high efficiency, controllability, and flexibility[154]. By adjusting reaction conditions such as temperature, flow rate, and substrate properties, the CVD method allows precise control over the growth direction, size, and morphology of the NWs. Its excellent control capabilities enable the synthesized perovskite NWs to typically have a lower defect density and higher crystal quality, resulting in outstanding optoelectronic properties[155]. Compared to other synthesis methods, CVD enables the production of high-purity, uniform, and high-performance perovskite NWs and facilitates large-scale production in a short time[156]. This makes it highly promising for the commercial application of halide perovskite NWs. Meng et al., for the first time, synthesized $CsPbX_3$ (X = Cl, Br, and I) NWs using the vapor−liquid−solid method with precise control over the microstructural morphology, NW density, and chemical composition. The high-quality NWs obtained by this method enable their corresponding optoelectronic devices to demonstrate exceptional performance[157,158]. Hossain et al. investigated the mechanism of non-catalytic CVD growth of $CsPbX_3$ NWs. Using techniques such as electron microscopy and time-resolved PL, they studied the influence of different substrates on NW growth. The results showed that these NWs could reach lengths of up to 10 μm and have a diameter of approximately 39 nm on sapphire substrates (Fig. 10a–c). Their optical properties were consistent with the final NWs, exhibiting a lower defect density. The research team revealed the growth process of the NWs, including the nucleation of halide particles, axial extension, and eventual merging into NWs, offering a new approach for catalyst-free CVD growth methods[159]. Furthermore, Li et al. proposed a surface-energy-mediated self-catalytic method, where the CVD-grown $CsPbBr_3$ NWs were optimized by adjusting the substrate surface roughness. The optimal NWs were about 5 μm in length and approximately 90 nm in diameter (Fig. 10d). The photodetector based on these NWs exhibited a responsivity of about 2000 A/W and a response time of 362 μs (Fig. 10e, f), demonstrating excellent optoelectronic performance[160]. This self-catalytic method avoids the introduction of metal impurities by eliminating the need for external metal catalysts, thereby improving the optoelectronic performance and stability of the NWs. Yadav et al. investigated the morphological control of RP BA_2PbBr_4 (BA = butylammonium) via the CVD method and found that temperature plays a crucial role in regulating morphology. At high temperatures, RP perovskites grow in the form of thin NSs. In contrast, at moderate temperatures, they exhibit a three-dimensional pyramidal shape, which further extends into NWs (Fig. 10g). Experiments showed that these RP perovskite NWs exhibit an exciton binding energy of approximately 279 meV and a radiative decay time of 1.7 ns, much lower than the 8.7 ns of conventional 3D $CsPbBr_3$ NWs (Fig. 10h)[161]. The strong absorption and radiative emission characteristics make RP BA_2PbBr_4 NWs a promising candidate for high-efficiency light sources with potential nanophotonics and optical communication applications. In summary, these studies reveal the key role of the CVD method in synthesizing halide perovskite NWs and demonstrate the wide application potential of perovskite NWs with different morphologies and structures in optoelectronic devices.

Hot injection method. The hot-injection method is also commonly used for synthesizing halide perovskite NWs. During the synthesis process, researchers can precisely control the size, morphology, and optoelectronic properties of the NWs by adjusting various factors such as reaction temperature, solvent, precursor concentration, and halide species[162,163]. For example, Li et al. improved the hot-injection method and synthesized $CsPbBr_3$ NWs using a solvent system rich in oleylamine. By controlling the reaction temperature (ranging from 120 °C to 180 °C), they successfully obtained pure nanostructures with different Pb/Br ratios (CsBr, Cs_4PbBr_6, and $CsPbBr_3$). When the reaction temperature was set at 120 °C, lead-free CsBr NCs were synthesized. As the temperature increased, the product gradually transformed into Cs_4PbBr_6, and eventually, $CsPbBr_3$ NWs with a PLQY of 64.9% were produced, with an emission peak at 521 nm (Fig. 11a, b). These NWs exhibited high-intensity stability in white LEDs and maintained excellent performance without encapsulation[164]. In another study, Gokul et al. explored the synthesis process of $CsPbI_3$ NWs using the hot-injection method, focusing on their phase transition. They found that $CsPbI_3$ NWs exist in the non-perovskite δ-$CsPbI_3$ phase from the moment of synthesis rather than initially forming the perovskite phase and subsequently transitioning to the non-perovskite phase, as previously expected (Fig. 11c). The synthesized $CsPbI_3$ NWs have a length of approximately 10 μm (Fig. 11d)[165]. This study demonstrates that the hot-injection method enables precise control over the morphology and phase of NWs under high-temperature conditions, thereby enhancing the controllability of the synthesis process. Furthermore, He et al. successfully synthesized $CsPbX_3$ NWs with a high aspect ratio and an orthorhombic crystal phase using the hot-injection method by controlling the reaction conditions and surface ligands. Through an ion exchange process, they precisely tuned the halide composition and bandgap, achieving luminescence modulation of $CsPbX_3$ NWs. As the halide ratio varied, the PL of the NWs covered a broad range of the visible spectrum (Fig. 11e, f), exhibiting excellent optoelectronic properties[31].

Template-assisted growth method. The template-assisted growth method can control the size and orientation of halide perovskite NWs by using a template material with a uniform channel structure[166,167]. This method provides unique capabilities for synthesizing high-quality NWs with exceptional uniformity, achieved through simultaneous regulation of nucleation dynamics and crystal growth pathways[168]. Furthermore, the inherent versatility of template materials combined with their structural

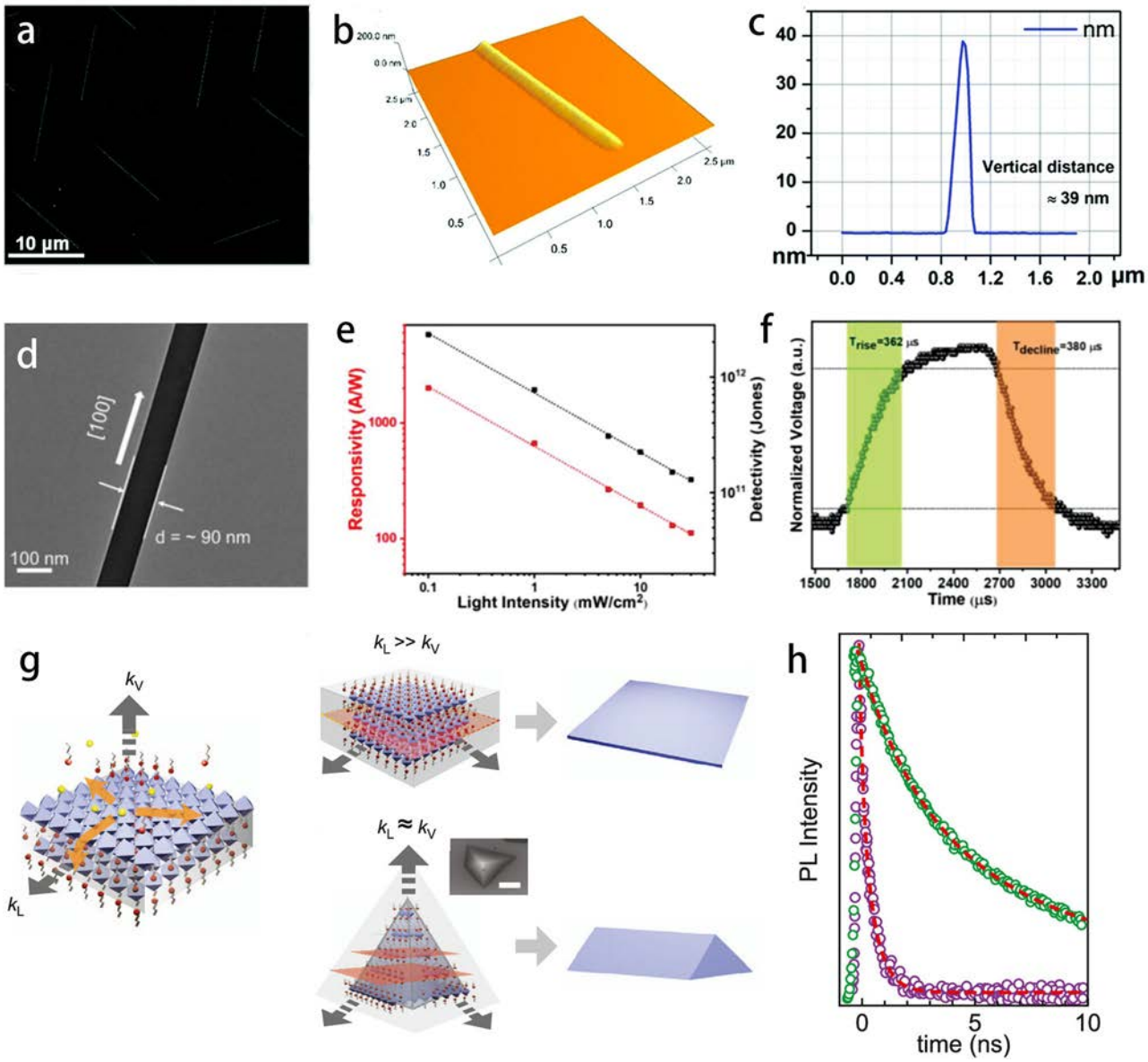

Fig. 10 | CVD method for synthesizing perovskite NWs. a FESEM image of $CsPbBr_3$ NWs grown on c-Al_2O_3. **b, c** The AFM image of $CsPbBr_3$ NWs and the corresponding line scan showing the NW height. **d** TEM image of self-catalyzed $CsPbBr_3$ NWs. **e** The variation of responsivity and detection rate with light intensity. **f** Rise and decay times of the photodetector. **g** Schematic diagram of the growth mechanism of BA_2PbBr_4. **h** Time-resolved PL spectra of BA_2PbBr_4 (purple circles) and $CsPbBr_3$ (green circles), along with double-exponential fitting (red dashed line). **a, b, c** Reproduced with permission from ref. 159. Copyright 2021, Royal Society of Chemistry; **d, e, f** Reproduced with permission from ref. 160. Copyright 2022, John Wiley and Sons; **g, h** Reproduced with permission from ref. 161. Copyright 2023, American Chemical Society.

tunability endows this approach with scalable manufacturing potential, addressing critical requirements for industrial-scale nanomaterial production[169]. Lin et al. successfully prepared perovskite NWs by combining inkjet printing with AAO templates (Fig. 12a), achieving tunable emission across a wide color gamut by adjusting the halide components (Cl, Br, I). In their study, the researchers precisely controlled the ratio of halide components, tuning the emission wavelength from 439 nm to 760 nm, demonstrating an exceptionally wide color gamut. Through PMMA encapsulation, the NW arrays exhibited only a 19% decrease in PL intensity after 250 h of laser excitation. After three months of storage in 50% humidity air, they degraded by 30% (Fig. 12b, c), demonstrating excellent stability[170]. The results of this study represent significant progress in long-term stability and tunable luminescence capabilities, providing the theoretical foundation and practical support for perovskite NW-based LEDs. Chu et al. successfully fabricated $CsPbBr_3$ NW arrays (Fig. 12d, e) on Au substrates using a polydimethylsiloxane (PDMS) template to control the NW size precisely and developed a low-threshold plasmonic laser. The threshold power of the fabricated NWs laser was 10 μJ/cm^2, significantly lower than the threshold of conventional perovskite lasers[171]. This work provides new insights for the large-scale production of perovskite NWs plasmonic nano-lasers. Song et al. synthesized $CsPbBr_3$ perovskite columnar crystalline thin films with controllable diameters (50-400 nm) using the AAO template method (Fig. 12f) and applied them in X-ray detectors. The passivated surface between the AAO and $CsPbBr_3$ NWs led to reduced ion migration. The X-ray detector based on $CsPbBr_3$ exhibited a dark current drift of only 2.185×10^{-6} nA·cm^{-1}·s^{-1}·V^{-1} (Fig. 12g), showing excellent stability and low noise levels, making it suitable for high-sensitivity radiation detection[172]. Despite these advancements, the template-assisted growth method still faces several challenges, including potential NW damage

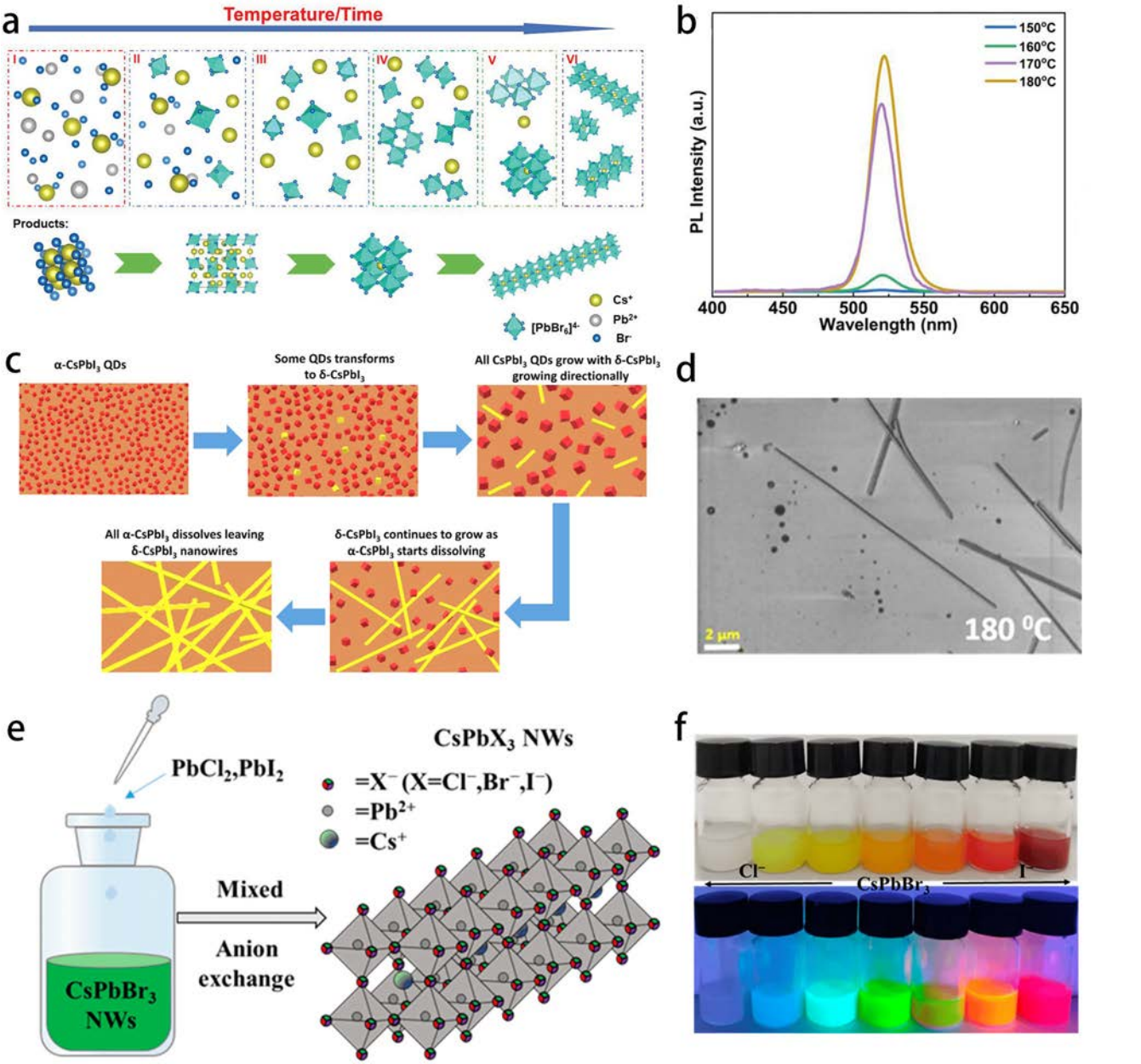

Fig. 11 | Hot injection method for synthesizing perovskite NWs. a Schematic diagram of the formation mechanism of CsBr, Cs_4PbBr_6, and $CsPbBr_3$ nanostructures. **b** PL spectra of samples at different reaction temperatures[164]. **c** Schematic diagram showing the growth of δ-$CsPbI_3$ NWs. **d** FESEM images of $CsPbI_3$ NWs synthesized at 180 °C for 10 minutes[165]. **e** Schematic diagram of the anion exchange reaction of all-inorganic $CsPbX_3$ NWs. **f** Images of $CsPbX_3$ NWs solutions taken under sunlight and a 365 nm UV lamp, respectively[31]. **a**, **b** Reprinted under the terms of the Creative Commons CC-BY License from ref. 164; **c**, **d** Reproduced with permission from ref. 165. Copyright 2021, IOP Publishing; **e**, **f** Reprinted under the terms of the Creative Commons CC-BY License from ref. 31.

during the template removal process, incomplete template removal leading to contamination of perovskite NWs, and difficulties in precisely controlling the length of the NWs[173].

Self-assembly method. The self-assembly method provides a low-energy consumption and simple synthesis route for halide perovskite NWs. This approach guides the spontaneous assembly of perovskite precursors into ordered nanostructures through interactions between molecules or nanoparticles, such as hydrogen bonding, van der Waals forces, or electrostatic interactions[174]. The assembly process involves careful modulation of solution thermodynamics through solvent selection, thermal management, and concentration gradients, which collectively regulate precursor solubility and interfacial interaction dynamics to drive the anisotropic growth of NWs architectures[175,176].

Pan et al. successfully synthesized $CsPbBr_3$ NWs with excellent optoelectronic properties by introducing halide vacancies and combining a ligand-assisted self-assembly method. The study showed that when oleic acid and didodecyldimethylammonium sulfate (DDAS) were used as ligands, $CsPbBr_3$ QDs could self-assemble into NWs with widths ranging from 20 to 60 nm and lengths of several millimeters, driven by a surface rich in bromine vacancies (Fig. 13a). The PL peak of these NWs was located at 525 nm, with a full width at half maximum of 18 nm. The synthesized NWs exhibited excellent optical performance, good crystallinity, and fewer defects[177]. Zhang et al. fabricated perovskite/insulator/organic semiconductor (PIO) radial heterostructure NWs using a self-assembly method (Fig. 13b). The synthesized NWs have diameters ranging from 500 nm to 2 μm, lengths reaching several millimeters, and a uniform radial distribution, demonstrating good morphological

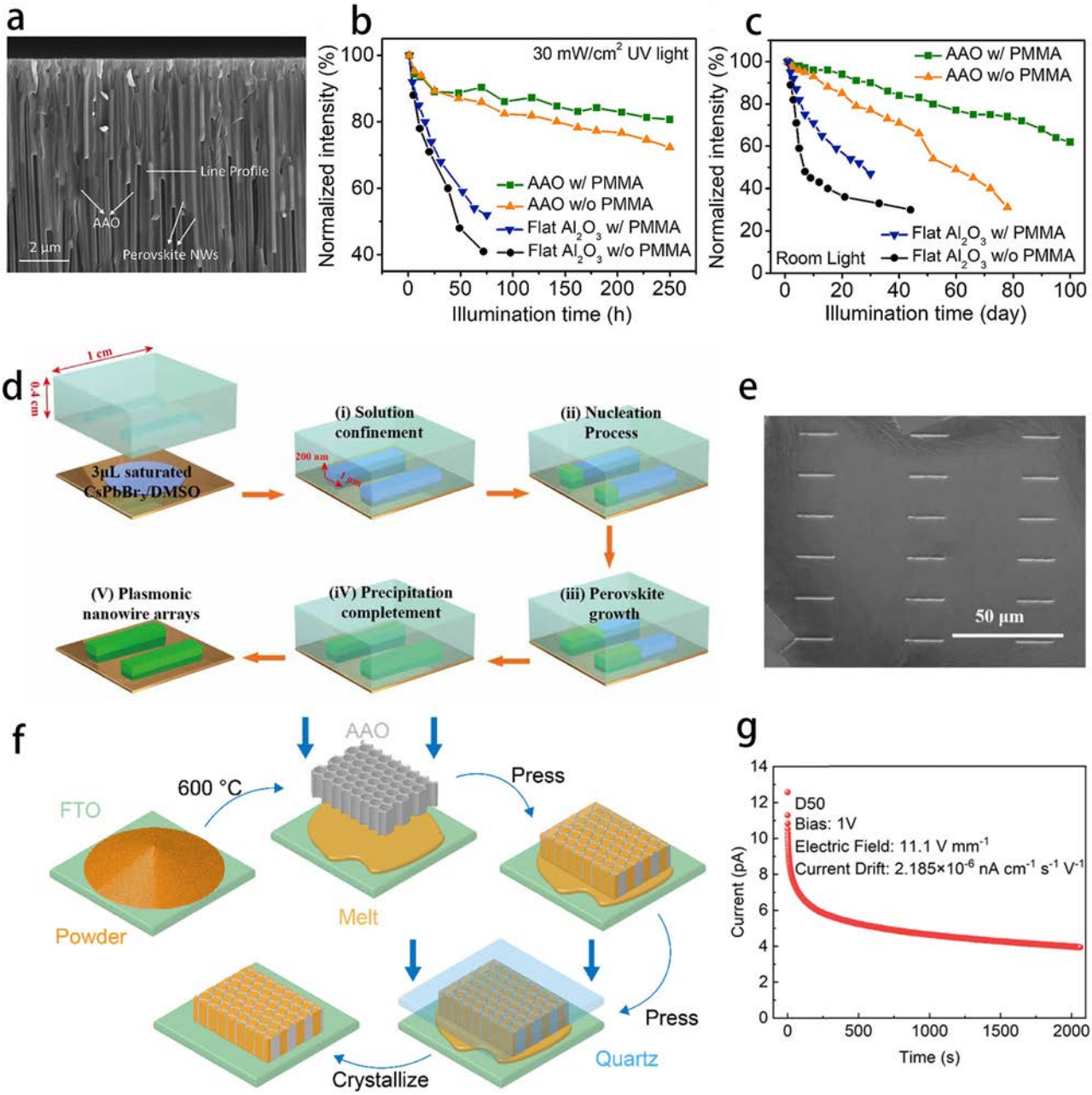

Fig. 12 | Template-assisted growth method for synthesizing perovskite NWs. **a** Cross-sectional SEM image of perovskite NWs in AAO nanopores. **b, c** The variation of PL intensity of the sample with time under 30 mW/cm^2 UV excitation and indoor illumination. **d** Schematic diagram of the preparation of $CsPbBr_3$ NW array using a PDMS template. **e** Large-scale $CsPbBr_3$ NW array. **f** Process flow diagram of the AAO template-assisted melt-pressing method. **g** Dark current drift of $CsPbBr_3$ NW film. **a**–**c** Reproduced with permission from ref. 170. Copyright 2020, Elsevier; **d, e** Reproduced with permission from ref. 171. Copyright 2022, IOP Publishing; **f, g** Reproduced with permission from ref. 172. Copyright 2024, Royal Society of Chemistry.

consistency (Fig. 13c). Additionally, the smooth surface of the NWs indicates a low defect density; these excellent morphological characteristics make $MAPbI_3$ NWs ideal candidates for the fabrication of dual-ended single-wire photodetectors[178]. Peng et al. prepared ultrafine $CsPbBr_3$ NWs using a two-step solvothermal and self-assembly method for polarized light detection. By adjusting the solution conditions, they synthesized perovskite NWs with diameters below 20 nm, exhibiting excellent polarized light response capabilities. Their study demonstrated a strong polarization dependence in the self-assembled $CsPbBr_3$ NWs arrays, with a polarization degree as high as ~0.49 (Fig. 13d, e)[179]. This NW array effectively detects low-intensity polarized light, showing promising potential for future applications. In addition, Ghorai et al. proposed an innovative method for repairing degraded CsPbI3 NCs through a self-assembly approach in a recent study. By adding diphenyl diselenide (DPhDSe) as a ligand to the dispersion of degraded $CsPbI_3$ NCs, the π-π stacking interaction of DPhDSe successfully enabled the $CsPbI_3$ NCs to self-assemble into microfibers. This method restored the optical properties of $CsPbI_3$, increasing its PLQY from 12% to 57%, and demonstrated excellent optical stability, with the microfibers maintaining good optical properties after 15 days of ambient storage[180]. This study provides new insights into the stability and self-assembly applications of $CsPbI_3$ materials.

Despite the many advantages of the self-assembly method, challenges remain, including unstable yield, difficulties in morphology control, and scalability issues for large-scale production. Further research and optimization are needed to address these challenges[181].

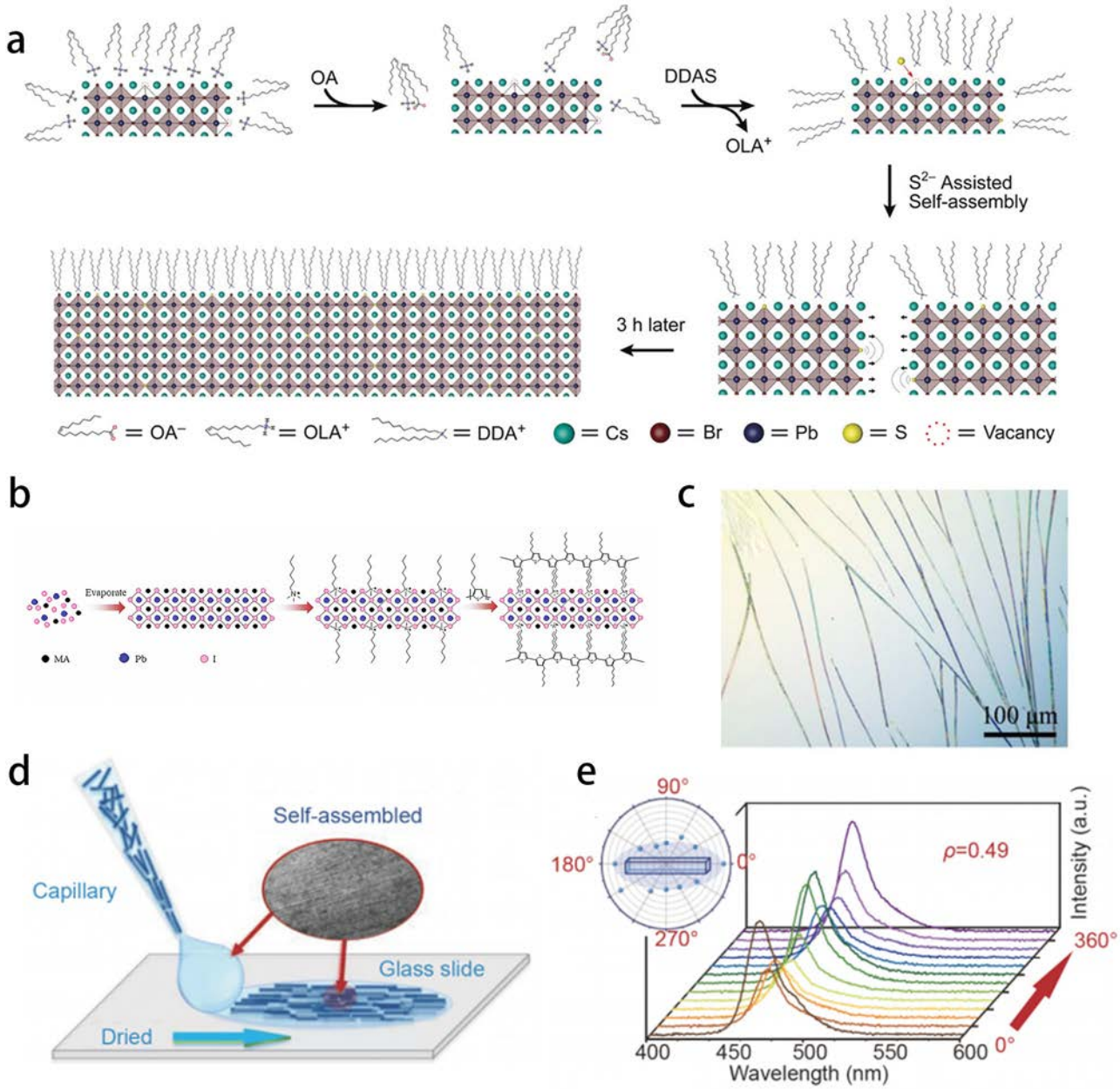

Fig. 13 | Self-assembly method for synthesizing perovskite NWs. a Schematic illustration of the self-assembly process of $CsPbBr_3$ QDs into NWs. **b** The schematic illustration of the self-assembly process of the PIO MWs. **c** Optical microscopy image of PIO-MWs. **d** Schematic diagram of the large-scale self-assembled $CsPbBr_3$ NWs array. **e** Upconversion PL spectra of the self-assembled $CsPbBr_3$ NWs array recorded under excitation polarization angles from 0° to 360°. **a** Reproduced with permission from ref. 177. Copyright 2019, John Wiley and Sons; **b, c** Reproduced with permission from ref. 178. Copyright 2021, John Wiley and Sons; **d, e** Reproduced with permission from ref. 179. Copyright 2021, Springer Nature.

Optoelectronic applications

Photodetectors. The application of perovskite NWs in photodetectors has gained widespread attention due to their long carrier diffusion lengths and high carrier mobilities, which allow them to efficiently convert light signals into electrical signals, offering significant performance advantages in photodetectors[182]. Additionally, the tunable bandgap of perovskite NWs provides adjustable spectral response capabilities, enabling photodetectors to operate across multiple wavelength ranges[183]. Chen et al. proposed a chemical potential-dependent surface energy difference amplification strategy to achieve the anisotropic growth of $CsPbBr_3$. Using this method, they successfully synthesized ultra-long single-crystal $CsPbBr_3$ NWs with an aspect ratio exceeding 10^5 through a one-pot process. The photodetector based on these NWs demonstrated an extremely high responsivity, reaching up to 4923 A W^{-1}, with an EQE exceeding 13784%, and a detectivity of 3.6×10^{13} Jones (Fig. 14a, b), showcasing their tremendous potential in devices such as photodetectors[184]. To further enhance the performance of perovskite NWs in photodetectors, Chen et al. developed a stable α-$FAPbI_3$ perovskite 1D structure array with high crystallinity and ordered crystal orientation through controllable nucleation and growth in capillary bridges. To improve its stability, the researchers functionalized the surface of the $FAPbI_3$ NWs with phenylethylammonium ions (PEA^+). After 28 days of storage in an environment with a relative humidity of 50%, the treated $FAPbI_3$ NWs maintained their stable α-phase. The study showed that the photodetector based on this material exhibited a responsivity of 5282 A/W and a detectivity of 1.45×10^{14} Jones (Fig. 14c, d)[185]. This significant improvement in optoelectronic performance indicates that fine control over the growth of perovskite NWs can substantially enhance their performance in photodetector applications.

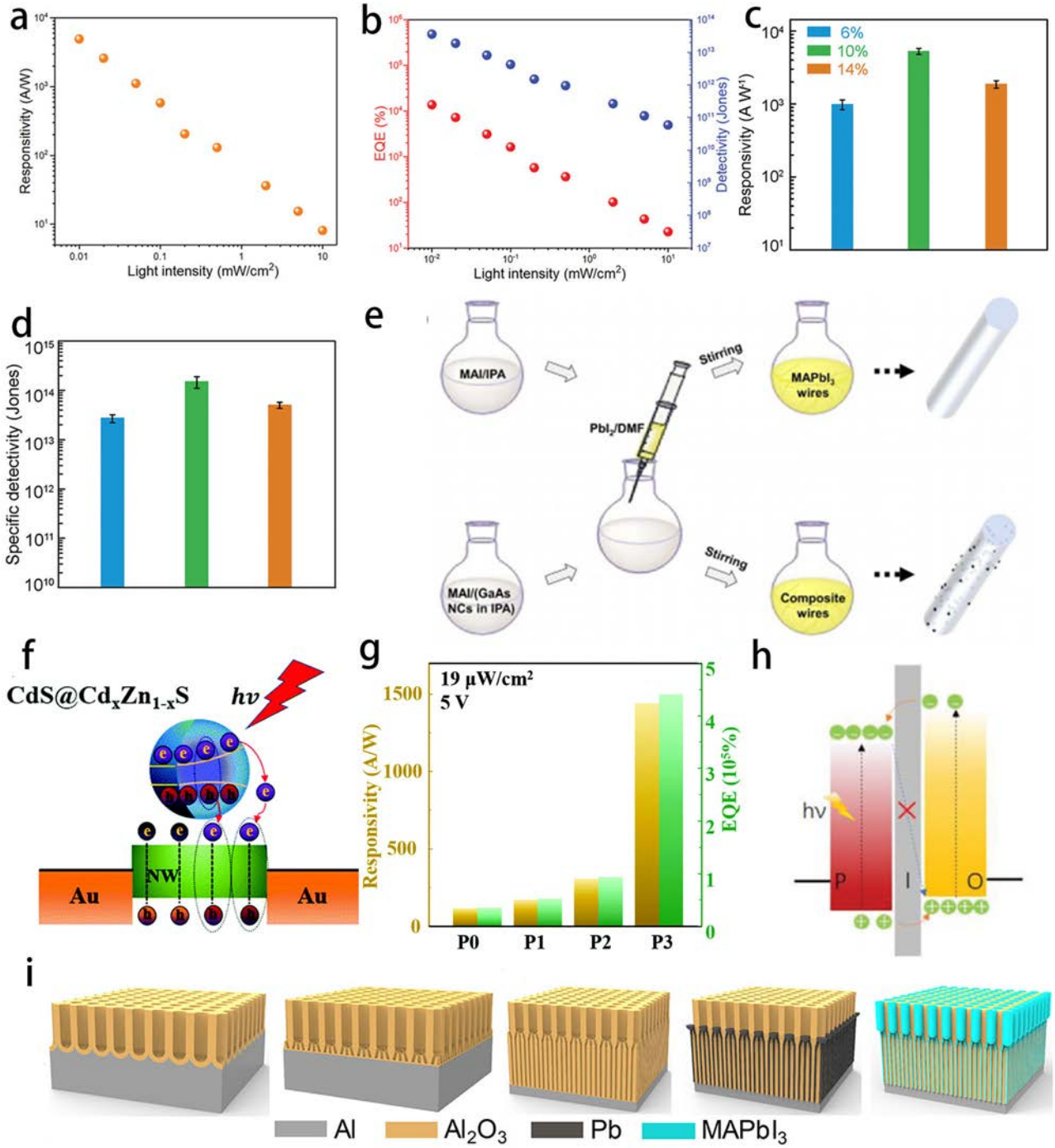

Fig. 14 | Application of perovskite NWs in photodetectors. a The variation of photodetector responsivity with light intensity. **b** The variation of photodetector EQE and detection rate with light intensity. **c**, **d** Responsivity and detection rate of devices with different PEA^+ contents **e** Schematic illustration of the fabrication process of $MAPbI_3$ NWs and GaAs-$MAPbI_3$ NWs. **f** Schematic diagram of the channel current transport mechanism of a photodetector based on $CdS@Cd_xZn_{1-x}S$ QDs modification under illumination. **g** Photodetector responsivity and EQE. **h** Energy level diagram of the PIO heterojunction and schematic illustration of the photoinduced charge generation mechanism. **i** Schematic diagram of the fabrication process of $MAPbI_3$ QW/NW arrays. **a**, **b** Reproduced with permission from ref. 184. Copyright 2021, John Wiley and Sons; **c**, **d** Reproduced with permission from ref. 185. Copyright 2020, John Wiley and Sons; **e** Reproduced with permission from ref. 186. Copyright 2022, Springer Nature; **f, g** Reproduced with permission from ref. 187. Copyright 2022, Royal Society of Chemistry; **h** Reproduced with permission from ref. 178. Copyright 2021, John Wiley and Sons; **i** Reproduced with permission from ref. 188. Copyright 2022, American Chemical Society.

Doping NCs into halide perovskite NWs is also an effective strategy to enhance optoelectronic performance and optimize device performance. Guo et al. embedded GaAs NCs into perovskite NWs (Fig. 14e) and studied the advantages of this composite structure in improving charge transport properties. By incorporating GaAs NCs into $CsPbI_3$ NWs, the carrier mobility was significantly increased from 1.13 to 3.67 $cm^2 \cdot V^{-1} \cdot s^{-1}$, leading to a notable improvement in the performance of photodetectors based on this material[186]. Additionally, Wei et al. modified the surface of $CsPbBr_3$ NWs by embedding $CdS@Cd_xZn_{1-x}S$ gradient alloy QDs (Fig. 14f), which significantly enhanced the responsivity of photodetectors. The study showed that, compared to the original $CsPbBr_3$ NWs device, the photodetector responsivity of the QDs-modified $CsPbBr_3$ NWs increased from 116.9 to

1442 A/W, with the detectivity improving by more than ten times (Fig. 14g)[187]. Zhang et al. proposed an innovative radial heterostructure of perovskite/insulator/organic semiconductor (PIO) NWs (Fig. 14h). The photodetector based on this heterostructure exhibited a responsivity exceeding 400 A/W in the visible light range, with a response time of 50 ms. It also demonstrated a high bright/dark current switching ratio ($>2 \times 10^5$) and excellent flexibility, maintaining high performance even in a bent state[178]. Additionally, Zhang et al. introduced a vertical heterostructure integration method for MHP quantum wire/nanowire(QW/NW), where $CsPbBr_3$ QW/NW arrays were integrated into a porous alumina film (Fig. 14i). The photodetector based on this $CsPbBr_3$ QW/NW array showed a broad spectral response, high sensitivity, and good bending performance[188]. This innovative heterostructure integration method provides new insights for applying perovskite NWs in photodetectors. In another study, Wang et al. developed a strategy for spraying perovskite intermediate suspensions, achieving the controllable fabrication of inch-scale (15×15 mm^2) perovskite MW films. Through the rapid evaporation of tiny droplets, this method avoids the issue of MWs re-dissolution and structural collapse caused by solvent residue in traditional spin-coating or drop-casting methods. The 7×7 photodetector array fabricated from this film exhibited excellent uniformity, with the champion device's detection rate surpassing that of polycrystalline films by an order of magnitude, reaching top performance in its category[189]. This method addresses the core challenge of scaling up the integration of perovskite MW films, providing a scalable fabrication solution for high-performance photodetector arrays.

Solar cells. Perovskite NWs exhibit significant application potential in solar cells due to their excellent light absorption capability and high PCE[190]. Additionally, the bandgap of perovskite NWs can be tuned by adjusting the type of halogen or the ratio of mixed halides, enabling effective absorption of sunlight across a broad spectral range and thereby enhancing the PCE of solar cells[191]. Swain et al. synthesized $CH_3NH_3PbI_{3-x}Br_x$ NWs with different I/Br ratios using a two-step deposition (TSD) method and evaluated their potential applications in solar cells. Their study revealed that Br doping modified the material's bandgap and energy levels, leading to significant improvements in the photovoltaic performance of $CH_3NH_3PbI_{3-x}Br_x$-based solar cells (Fig. 15a). Notably, when $x = 0.3$, the device exhibited a PCE of 13.6% under forward scanning and 16.07% under reverse scanning, demonstrating excellent performance (Fig. 15b)[192].

The large surface-to-volume ratio of NWs also makes surface defect passivation a particularly effective strategy for enhancing their optoelectronic performance. Zardari et al. investigated the effect of Urotropin (UTP) as a surface passivation agent on the stability and optoelectronic properties of 1D NWs. The introduction of UTP effectively passivated surface defects of NWs and improved crystallinity. Perovskite solar cells fabricated using a two-step spin-coating method achieved an optimal PCE of 19.15% under the best passivation conditions (5 mol %) (Fig. 15c). Furthermore, after 42 days of testing under a relative humidity of $38 \pm 2\%$, the PCE of the passivated solar cells decreased by only 5.08%, indicating that UTP passivation significantly enhances device stability[176]. Shin et al. proposed a biphasic passivation strategy by introducing a small amount of the $CsPb_2Br_5$ phase into $CsPbBr_3$ NWs, achieving structural optimization and defect passivation (Fig. 15d). The synthesized biphasic $CsPbBr_3/CsPb_2Br_5$ NWs were used as an interfacial layer in perovskite solar cells. Compared to devices based on single-phase $CsPbBr_3$, the PCE increased from 20.74% to 22.87%, while the PLQY of the NWs improved from 31% to 55% (Fig. 15e). Furthermore, after storage in an air environment for some time, the PCE retained 95.3% of its initial value (Fig. 15f)[193]. This strategy effectively reduced defects and significantly enhanced the performance and stability of solar cells. Cha et al. further investigated the dual role of perovskite NWs in photovoltaic devices, serving as defect passivation agents and charge transport networks (Fig. 15g) to improve the optoelectronic performance and stability of the devices. This approach significantly reduced non-radiative recombination losses and enhanced charge transport efficiency, enabling NW-based solar cells to achieve a PCE of 21.56% (Fig. 15h). In long-term stability tests, the device maintained 80% of its initial efficiency even after 3500 hours, demonstrating excellent long-term stability[194].

In conclusion, researchers have significantly enhanced the photovoltaic conversion efficiency and stability of NWs in photovoltaic devices through doping, surface passivation, and phase stability optimization. However, challenges remain in terms of scalability and long-term stability. Future studies could further integrate carrier dynamics, interface optimization, and device integration to advance the commercialization of perovskite NW-based photovoltaic devices[195].

Lasers and LEDs. Apart from photodetectors and solar cells, perovskite NWs can also be applied to lasers due to their high exciton binding energy and excellent optoelectronic properties[196]. Researchers have successfully enhanced their laser emission efficiency and stability through structural optimization and doping strategies. Tang et al. proposed a solid-solid anion diffusion process to construct $CsPbCl_{3-3x}Br_{3x}$ NWs, enabling the realization of single-NW lasers with tunable laser emission over a wide spectral range. The $CsPbCl_{3-3x}Br_{3x}$ NWs synthesized using this method exhibit a wide tunable bandgap ranging from 2.41 to 2.82 eV, and based on this material, a continuous tunable nanolaser with a wavelength range from 480 to 525 nm was achieved (Fig. 16a). The laser threshold of this wavelength range varies from 35.0 to 11.7 μJ/cm^2 (Fig. 16b), showing good stability in laser output[197]. In further studies, Sun et al. synthesized $CsPbBr_3$ NWs with high crystal quality using an improved physical vapor deposition process. These NWs demonstrated excellent laser performance under two different pump modes (Fig. 16c). Under single-photon pumping, the threshold of the NWs laser was 12.2 μJ/cm2 (Fig. 16d). The quality factor (Q) reached 1078. Under two-photon pumping, although the threshold increased to 26.9 μJ/cm^2 (Fig. 16e), the quality factor remained high at 772. Temperature-dependent fluorescence spectroscopy tests showed that the high exciton binding energy of $CsPbBr_3$ NWs is the main reason for maintaining laser stability under high-energy injection conditions[198]. In addition, Guo et al. proposed an improved CVD method to directly grow high-quality heterojunction $CsPbCl_3/CsPbI_3$ NWs (Fig. 16f). The synthesized NWs possess a single-crystal structure with a sharp interface at the junction and low defect density. Based on these perovskite NWs, they fabricated a monolithic dual-wavelength laser and successfully achieved blue (425.5 nm) and red (687.4 nm) emissions (Fig. 16g, h)[199]. These studies demonstrate the tremendous potential of perovskite NWs in the field of lasers, especially in tunable and multi-wavelength lasers. Regarding device integration, Zhao et al. introduced a technique for fabricating ultra-thin, size-controllable perovskite surface plasmon polariton lasers using PDMS-assisted imprinting. Through this technique, the researchers could precisely control the size and arrangement of $CsPbBr_3$ NWs, thereby developing a plasmonic laser array that significantly enhanced the performance of the lasers[200]. This breakthrough provides a solution for applying plasmonic laser arrays in optoelectronic integration.

Significant progress has also been made in applying perovskite NWs in LEDs, particularly in color tunability and efficient light emission. Wu et al. reported a self-assembled green-to-white switchable LED based on $CsPbBr_3$ NWs. By adjusting the NWs concentration and applying different bias voltages, the device can switch between green and white light emission. In high-concentration NWs devices, the LEDs emit pure green light, with the EL peak located around 522 nm (Fig. 16i). In low-concentration NWs devices, as the voltage increases, the EL spectrum gradually transitions from green to white (Fig. 16j), indicating that the perovskite NWs device has good color-tuning capability and optoelectronic performance[181]. Zhang et al. further expanded the application of perovskite NWs in LEDs by reporting an LED based on large-area, highly uniform perovskite QWs arrays (Fig. 16l). By optimizing conditions such as the length of the perovskite QWs and the array structure, the emission spectrum of the device covered the entire visible light range, with a PLQY of 92% for $MAPbBr_3$ QWs (Fig. 16k). The device also exhibited excellent stability under ambient conditions, with the PL intensity decreasing to 50% of its initial value after

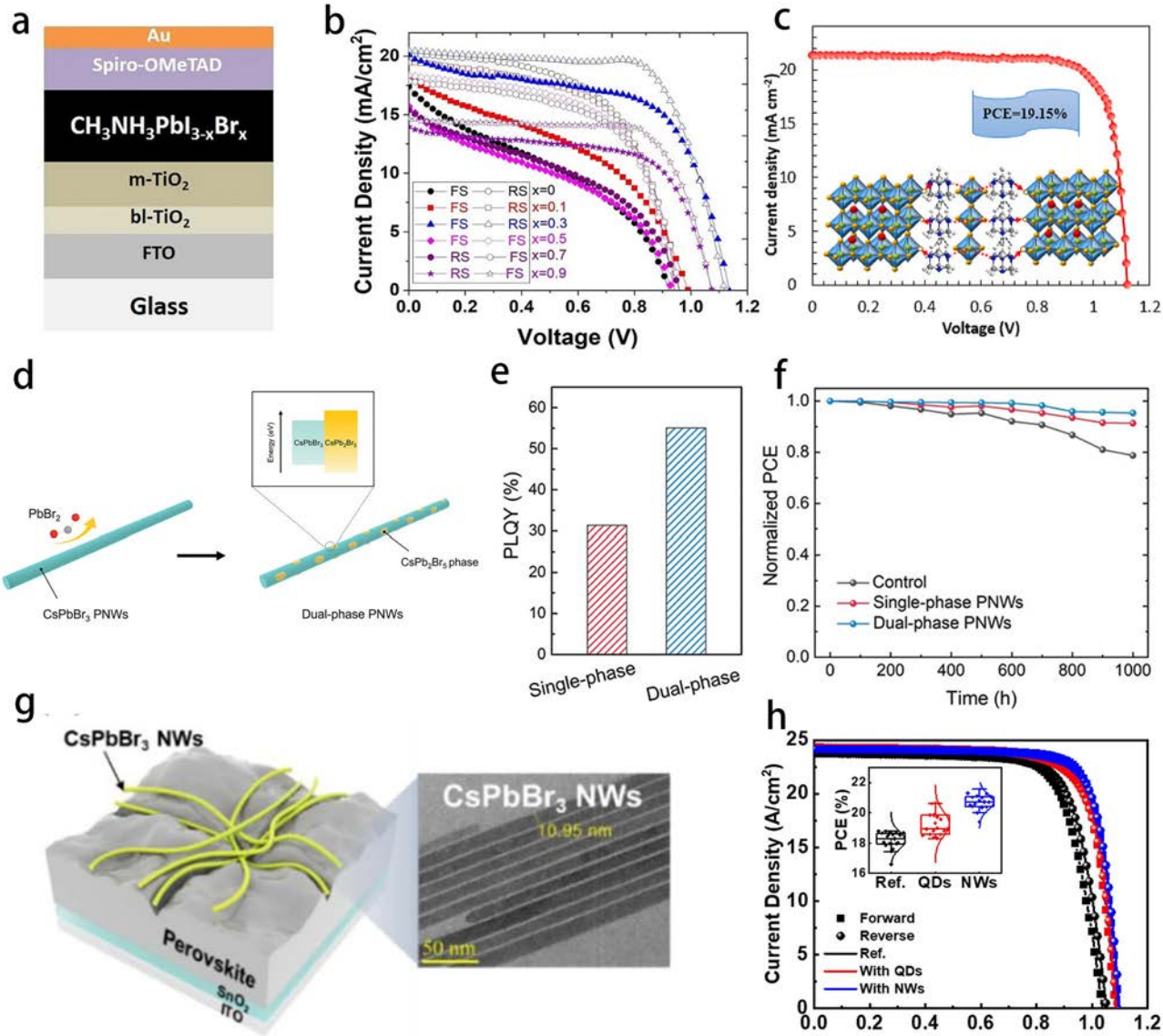

Fig. 15 | Application of perovskite NWs in solar cells. a Schematic diagram of the structure of $CH_3NH_3PbI_{3-x}Br_x$ perovskite solar cells. **b** J-V characteristics of a $CH_3NH_3PbI_{3-x}Br_x$-based solar cell under a single simulation of solar irradiation. **c** J-V characteristics and PCE of the solar cell, with an inset showing the interaction mechanism between UTP and the perovskite layer. **d** Schematic diagram of the synthesis of biphasic $CsPbBr_3/CsPb_2Br_5$ NWs. **e** PLQY of single-phase and biphasic NW solutions. **f** The variation of PCE of unencapsulated solar cells with time under a relative humidity of 25-35% and 25-35 °C. **g** Schematic diagram of the TEM image of NW-passivated perovskite solar cells. **h** J-V characteristics of perovskite solar cells passivated with QDs and NWs, with an inset showing the PCE. **a, b** Reproduced with permission from ref. 192. Copyright 2021, Springer Nature; **c** Reproduced with permission from ref. 176. Copyright 2021, Elsevier; **d, e, f** Reproduced with permission from ref. 193. Copyright 2022, John Wiley and Sons; **g, h** Reproduced with permission from ref. 194. Copyright 2022, Elsevier.

5644 hours[201]. This study provides strong support for the large-scale application of perovskite NWs in LEDs.

Two-dimensional nanostructure

Properties and advantages

2D halide perovskite NSs have emerged as promising optoelectronic materials, attracting significant attention in optoelectronics and photovoltaics in recent years[202,203]. These materials possess a unique layered structure, typically consisting of multiple 2D perovskite monolayers interacting via van der Waals forces, which grants them high tunability in the vertical direction[204]. By adjusting the thickness, crystal structure, and surface modifications of the NSs, researchers can tailor their band structure and optical properties to meet various application requirements[205]. The bandgap of 2D perovskite NSs generally falls within the ultraviolet to visible range, and by modifying their thickness and composition, their emission can be extended from the ultraviolet to the near-infrared spectrum; this property makes them highly promising for optoelectronic devices, particularly in solar cells, LEDs, and lasers[206,207]. Due to quantum confinement effects, the layered structure of 2D perovskites allows charge carriers to move freely within the 2D plane, unlike in 3D materials, where they are more susceptible to lattice defects and impurity scattering; this reduced carrier scattering perpendicular to the layers enhances carrier mobility, resulting in outstanding optoelectronic conversion efficiency[208]. This advantage is particularly significant in photovoltaic cells and photodetectors, where 2D perovskite NSs can deliver higher conversion efficiencies and faster response times[209,210]. Additionally, compared to conventional organic optoelectronic materials, 2D perovskite NSs typically exhibit longer carrier diffusion lengths, improving efficiency and stability in optoelectronic devices[211].

Synthesis methods

Solution-based methods. Solution-based methods are widely used to prepare halide perovskite NSs due to their advantages, such as low cost,

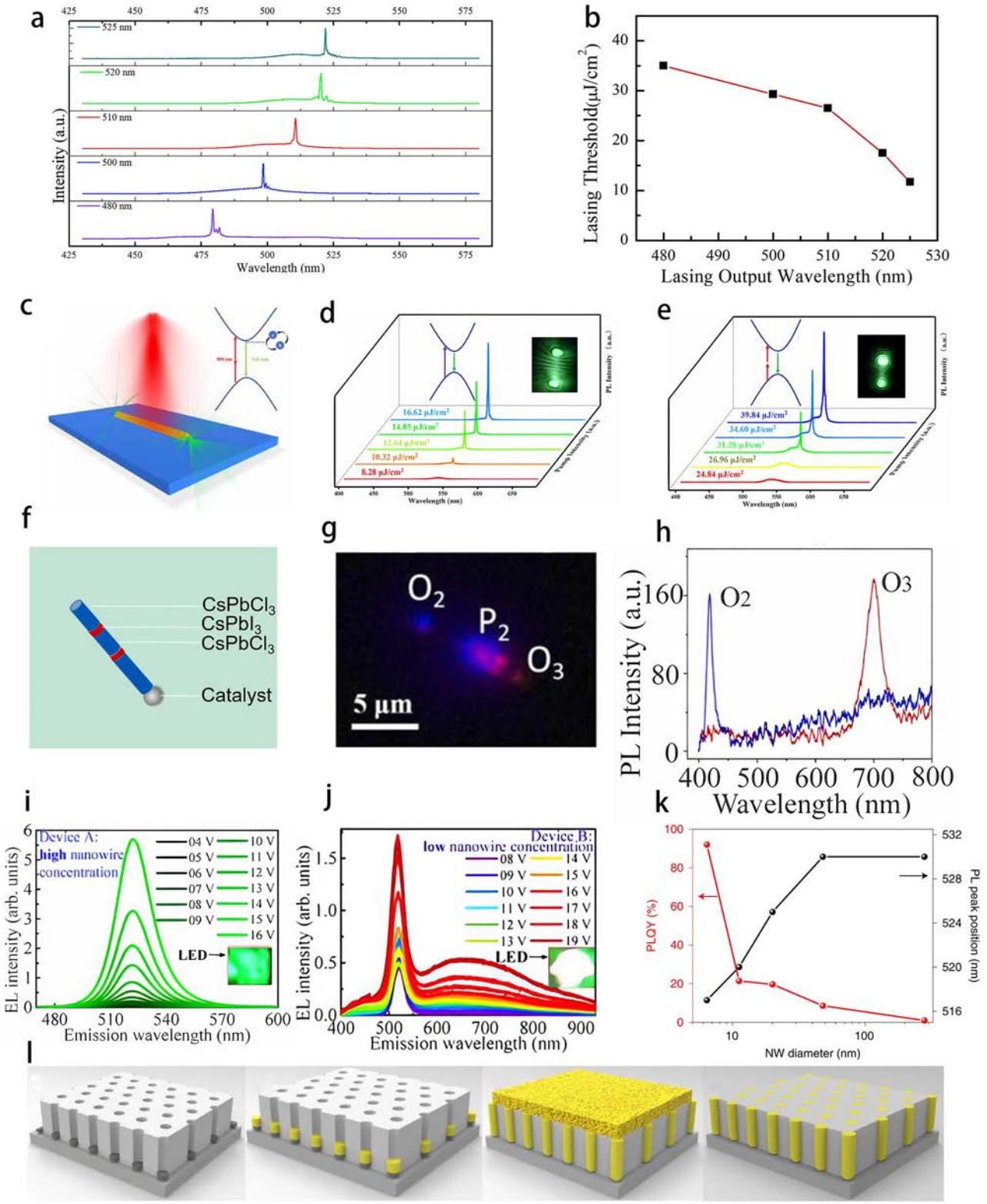

Fig. 16 | Application of perovskite NWs in Lasers and LEDs. a Laser spectrum of $CsPbCl_{3-3x}Br_{3x}$ NW-based laser. **b** The relationship between laser threshold and laser wavelength. **c** Schematic diagram of a two-photon pumped NW laser. **d**, **e** PL spectra at different energy densities under single-photon and two-photon pumping conditions, with an inset photo of the NW laser. **f** Schematic diagram of the structure of a heterojunction NW. **g** A real-color photo of the laser beam from the heterojunction NW. **h** PL spectrum of the heterojunction NW. **i** EL spectra of low-concentration NW devices at different bias voltages. **j** EL spectra of high-concentration NW devices at different bias voltages. **k** PLQY and PL spectra of QW arrays. **l** Schematic diagram of the synthesis of $MAPbBr_3$ QW arrays.
a, **b** Reproduced with permission from ref. 197. Copyright 2020, Elsevier;
c–**e** Reproduced with permission from ref. 198. Copyright 2021, IOP Publishing;
f–**h** Reproduced with permission from ref. 199. Copyright 2021, Elsevier;
i, **j** Reproduced with permission from ref. 181. Copyright 2021, AIP Publishing;
k, **l** Reproduced with permission from ref. 201. Copyright 2022, Springer Nature.

ease of operation, precise tunability, and strong adaptability[212,213]. This method has become one of the key synthesis techniques in the field, as it enables rapid synthesis and low-temperature processing, along with high yield and consistent reproducibility[204]. Moreover, the flexibility of solution-based methods allows for optimization according to specific requirements. By precisely adjusting parameters such as solvent type, concentration, chemical composition, and environmental conditions, researchers can fine-tune the physical and chemical properties of perovskite NSs to meet the demands of various applications[214]. For example, Huang et al. successfully synthesized lead-free double perovskite $Cs_2AgBiBr_6$ NSs using a solution-based approach. They dissolved the precursors in a solvent system consisting of 1-octene (ODE), oleic acid, and oleylamine and then reacted the mixture at 150 °C for 4 h. Finally, the NSs were collected through acetone precipitation (Fig. 17a). The synthesized $Cs_2AgBiBr_6$ NSs exhibited a 3-5 nm thickness and lateral dimensions around 200 nm. Regarding optical properties, the $Cs_2AgBiBr_6$ NSs showed a strong absorption peak at 430 nm (Fig. 17b) and a distinct PL peak at 630 nm (Fig. 17c), demonstrating excellent humidity and thermal stability[205].

By adjusting reaction conditions, the hot-injection method can also be used to synthesize NSs. For instance, Malani S et al. employed a colloidal hot-injection method to synthesize quasi-2D perovskite $(C_{12}H_{27}N)_2(MA)_{n-1}(Pb)_n(Br)_{3n+1}$ and investigated its application in photodetectors. By controlling reaction time, temperature, and solvent types, they could produce NSs, nanostripes, and NPLs (Fig. 17d–f) with lateral dimensions of approximately 50-150 nm and thicknesses between 2 and 5 nm. Upon applying these materials to photodetectors, they discovered that the $MAPbBr_3$ nanostripes exhibited the best optoelectronic performance compared to the NSs and NPLs[215]. Wang et al. successfully synthesized $CsPbBr_3$ perovskite nanomaterials of different sizes via a colloidal synthesis method. By adjusting precursor concentration, solvent type, and reaction temperature, they controlled the morphology of the nanomaterials, resulting in NRs, NSs, and NPLs with sizes of 4-10 nm for NRs and 10-100 nm for NSs (Fig. 17g, h). As the size increased, from NRs to NSs and finally NPLs, a significant redshift in the optical emission wavelength occurred, with the emission peak shifting from 485 nm to 530 nm (Fig. 17i). This shift indicates that the change in size has a significant impact on the optical properties of the materials[216]. Ruan et al. synthesized manganese-doped $CsPb_2Cl_5$ tetragonal perovskite NSs using a new ligand-mediated solvent-induced precipitation method (Fig. 17j). By controlling the Pb/Mn ratio and reaction conditions, they achieved Mn-doped $CsPb_2Cl_5$ NSs with bright PL and strong ferromagnetism. These NSs, with lateral dimensions of around 50–100 nm and 5–10 nm thicknesses, exhibited excellent optical properties and long-term stability, providing vast research prospects for their application in optoelectronic, magnetic, and photonic devices[217].

Exfoliation method. The mechanical exfoliation method is a technique that utilizes physical forces to separate perovskite crystals or thin films into monolayer or few-layer NSs[218]. This method is simple to operate, requires minimal equipment, and can produce high-quality NSs with clean surfaces, no contamination, and excellent electronic properties[219]. Li et al. successfully synthesized a series of $(C_4H_9NH_3)_2(CH_3NH_3)_{n-1}Pb_nI_{3n+1}$ perovskite NSs with n values ranging from 1 to 5 via mechanical exfoliation (Fig. 18a). These NSs had a thickness of approximately 20 nm. Using XRD and absorption spectroscopy, characterization revealed that materials with $n = 1$ and $n = 2$ exhibited a single-phase structure. In contrast, those with $n > 2$ contained mixed-phase structures with different n values (Fig. 18b). Furthermore, their application in photodetectors demonstrated promising optoelectronic performance[220]. Dhanabalan et al. further optimized the mechanical exfoliation method. They synthesized $(C_nH_{2n+1}NH_3)_2PbBr_4$ NSs with different organic cations (Fig. 18c). By varying the type of organic cation, they successfully enhanced the luminescence efficiency of the NSs, particularly in the blue-light region, where the PLQY of $(PEA)_2PbI_4$ perovskite NSs reached 42% (Fig. 18d)[221]. However, the mechanical exfoliation method has limitations, such as difficulty controlling the NS dimensions and significant material waste[222]. As a result, this method is more suitable for small-scale applications.

The liquid-phase exfoliation method enables the efficient production of large quantities of 2D perovskite NSs, which involves mixing halide perovskite materials with solvents or surfactants and using ultrasound, shear forces, or high pressure to exfoliate them from bulk materials into 2D NSs[223,224]. Hintermayr et al. proposed a ligand-assisted liquid-phase exfoliation technique, where they successfully exfoliated large-sized perovskite crystals into NPLs by grinding methylammonium halides with lead halides and then applying ultrasonic treatment with the assistance of an organic ligand (Fig. 18e). By adjusting the halide composition and the thickness of the NPLs, they achieved a broad spectral tunability from blue to red light (395–770 nm). Additionally, the perovskite NPLs prepared using this method exhibited a quantum yield of up to 70%. They demonstrated excellent stability, with nearly unchanged optical properties after months of storage in the dark at room temperature[225]. In further studies, Xie et al. successfully synthesized quasi-2D $CsPbBr_3$ NSs with ultra-high water stability using liquid-phase exfoliation (Fig. 18g). These NSs exhibited thicknesses ranging from a few nanometers to several tens of nanometers. They demonstrated good dispersion (Fig. 18f). The PLQY reached 82.3%. Furthermore, the PL intensity of the quasi-2D $CsPbBr_3$ NSs retained 87% of its initial value after 168 hours of immersion and 85% after 2 h of exposure to 365 nm UV light, indicating excellent environmental stability[226]. This method provides a new approach to enhancing the environmental stability of perovskite NSs and demonstrates their potential for optoelectronic applications.

Chemical vapor deposition. The CVD method is also an effective approach for synthesizing high-quality 2D halide perovskite NSs; by adjusting process parameters such as temperature, growth time, and gas flow rate, researchers can precisely control the composition, thickness, size, and morphology of perovskite NSs[227,228]. NSs synthesized through CVD typically exhibit excellent crystallinity and superior quality, making them ideal for demanding applications[208]. He et al. proposed a CVD strategy combining spatial confinement and van der Waals epitaxy (Fig. 19a) to synthesize large-sized, ultrathin inorganic perovskite NSs. The synthesized $CsPbI_3$ NSs exhibited a large lateral size exceeding 50 μm, with a minimum thickness of 3 nm (Fig. 19b). These NSs demonstrated long carrier lifetimes, high resistivity, and good stability, indicating their potential for high-performance integrated optoelectronic applications[229]. Using a solid-source CVD method, Liu et al. successfully synthesized lead-free, fully inorganic CsSnBr3 NSs on a mica substrate. By tuning the growth time, the thickness of the $CsSnBr_3$ NSs could be effectively controlled (Fig. 19c), which significantly influenced their optical properties. Studies have shown that as the thickness increases, the crystallinity and PL intensity of the NSs improve (Fig. 19d) while their nonlinear optical response decreases[230]. Shi et al. synthesized air-stable $FAPbBr_3$ single-crystal perovskite NSs via a vapor growth method (Fig. 19e). These NSs reached a maximum lateral size of 50 μm and a minimum thickness of 20 nm. This method significantly enhanced the air stability of perovskite NSs (Fig. 19f) and enabled exceptionally high photoresponsivity and on/off ratios in photodetectors[231]. Additionally, Yin et al. utilized a spatially confined CVD method to synthesize fully inorganic $CsSnI_3$ perovskite NSs (Fig. 19g) with dimensions of 4 × 4 μm^2 and a thickness of 10 nm (Fig. 19h). These NSs exhibited outstanding response performance in infrared photodetection. Moreover, by adjusting the gap distance within the confined space and the growth temperature, the size and thickness of the NSs could be precisely controlled[232].

Optoelectronic applications

Photodetectors. 2D halide perovskite NSs have attracted significant attention in photodetector research due to their outstanding

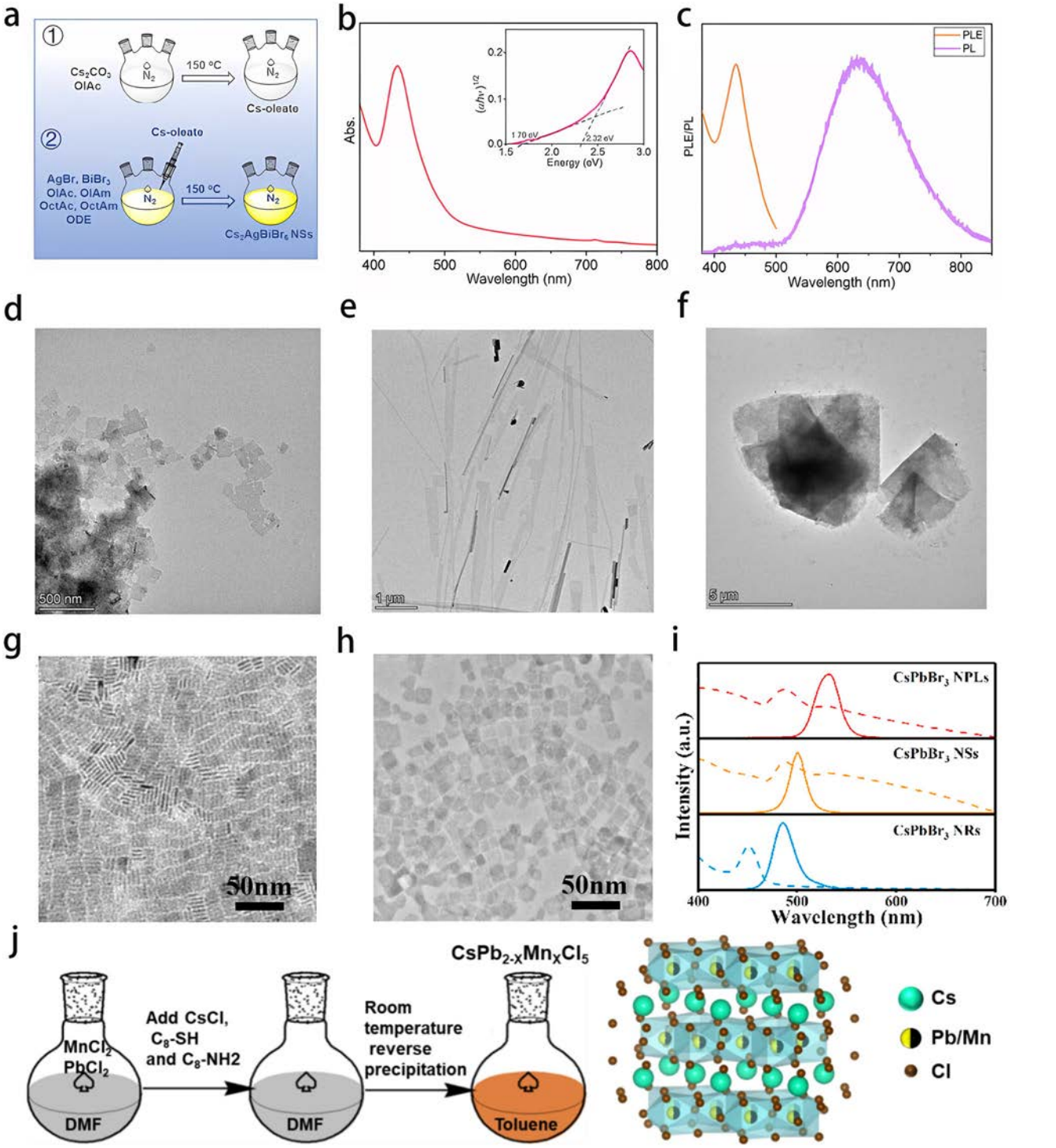

Fig. 17 | Solution-based methods for synthesizing perovskite NSs. a Schematic illustration of the synthesis of $Cs_2AgBiBr_6$ NSs. **b** Optical absorption and Tauc plot (inset) of $Cs_2AgBiBr_6$ NSs. **c** PL and PLE spectra of $Cs_2AgBiBr_6$ NSs. **d**–**f** TEM images of $(C_{12}H_{27}N)_2(MA)_{n-1}(Pb)_n(Br)_{3n+1}$ NSs, nanostripes, and NPLs, respectively. **g**, **h** TEM images of $CsPbBr_3$ NRs and $CsPbBr_3$ NSs. **i** PL spectra (solid lines) and UV absorption spectra (dashed lines) of $CsPbBr_3$ NRs, NSs, and NPLs. **j** Schematic illustration of the synthesis and crystal structure of Mn^{2+}-doped $CsPb_2Cl_5$ NCs. **a**–**c** Reproduced with permission from ref. 205. Copyright 2021, Springer Nature; **d**–**f** Reproduced with permission from ref. 215. Copyright 2024, John Wiley and Sons; **g**–**i** Reproduced with permission from ref. 216. Copyright 2024, Elsevier; **j** Reproduced with permission from ref. 217. Copyright 2024, Elsevier.

optoelectronic properties, tunability, and ease of processing[233]. Their large specific surface area effectively enhances photon absorption, improving photoelectric conversion efficiency and increasing detector sensitivity[214]. Moreover, their optical and electrical properties can be modulated by adjusting chemical composition, structure, and material thickness, allowing for performance optimization across different wavelength ranges to meet various photodetector application requirements[234].

Regarding thickness control in halide perovskite materials, Mandal et al. proposed optimizing the optoelectronic performance of $CsPbX_3$ (X = Br, Br/I, I) NSs by tailoring their thickness. Their study revealed that $CsPbBr_{1.5}I_{1.5}$ NSs with a thickness of 4.9 nm exhibited better structural stability than

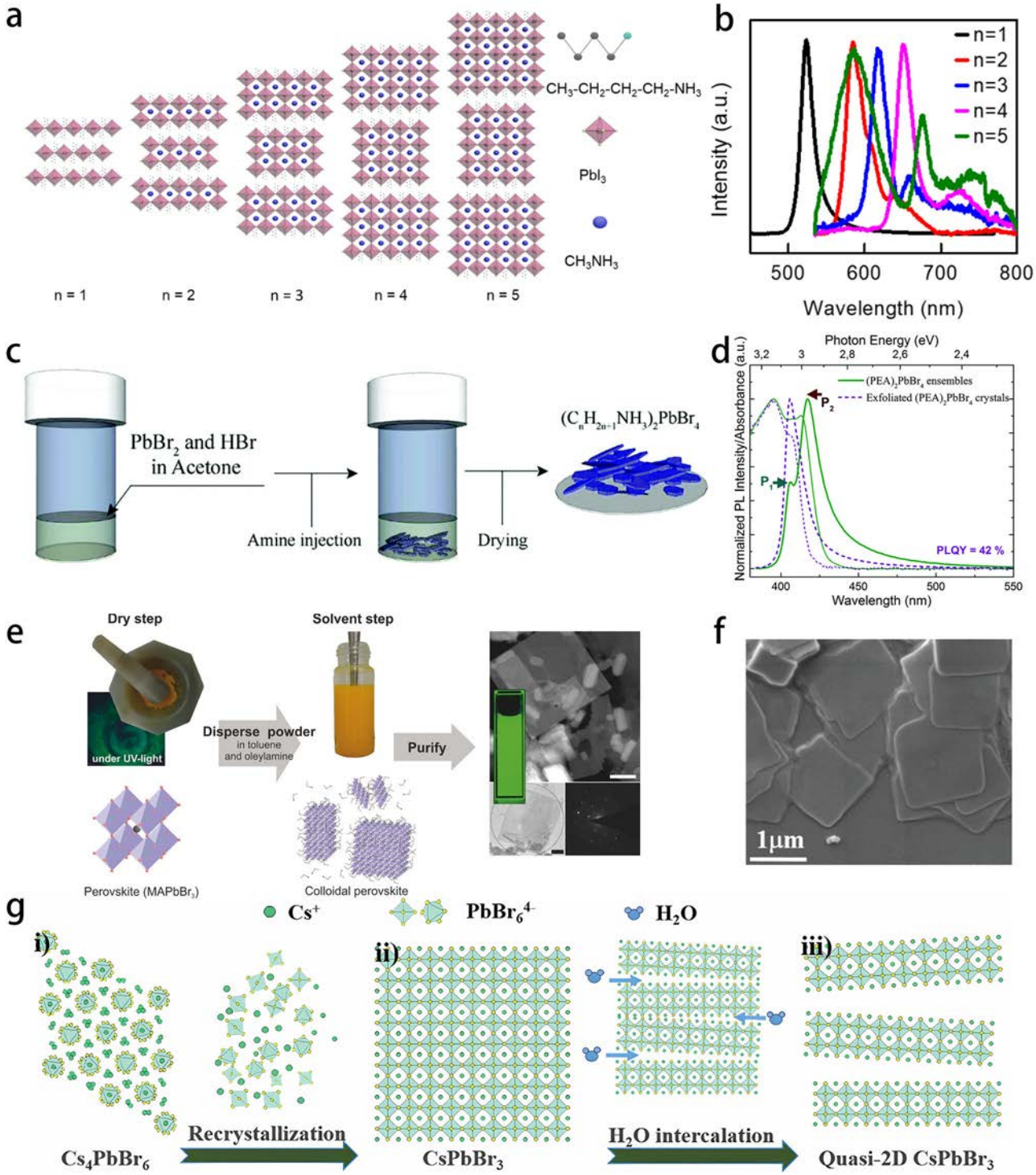

Fig. 18 | Exfoliation method for synthesizing perovskite NSs. a Schematic illustration of the crystal structure of $(C_4H_9NH_3)_2(CH_3NH_3)_{n-1}Pb_nI_{3n+1}$ for $n = 1–5$. **b** Normalized PL spectra of $(C_4H_9NH_3)_2(CH_3NH_3)_{n-1}Pb_nI_{3n+1}$ NPLs synthesized with $n = 1–5$. **c** Schematic illustration of the synthesis of $(C_nH_{2n+1}NH_3)_2PbBr_4$ NSs. **d** Normalized PL and absorption spectra of $(PEA)_2PbBr_4$ crystals before and after exfoliation. **e** Schematic Illustration of the Synthesis Process for $MAPbX_3$ (X = Cl, Br, I) NPL **f** SEM image of quasi-2D $CsPbBr_3$ NSs. **g** Schematic illustration of the aqueous-phase exfoliation process of quasi-2D $CsPbBr_3$ NSs. **a**, **b** Reproduced with permission from ref. 220. Copyright 2018, IOP Publishing; **c**, **d** Reprinted under the terms of the Creative Commons CC-BY-NC License from ref. 221; **e** Reproduced with permission from ref. 225. Copyright 2016, John Wiley and Sons; **f**, **g** Reproduced with permission from ref. 226. Copyright 2019, John Wiley and Sons.

$CsPbI_3$ NSs with a thickness of 6.8 nm. Additionally, compared to 3.7 nm $CsPbBr_3$ NSs, the $CsPbBr_{1.5}I_{1.5}$ NSs exhibited higher hole mobility. The photodetector based on these NSs demonstrated a remarkable responsivity of 3313 A/W at a 1.5 V bias (Fig. 20a) and excellent detection capabilities[235]. Ion doping is another crucial strategy for modulating the optoelectronic properties of perovskite materials and enabling various applications. Sun et al. reported $CsPbClBr_2$ NSs doped with ytterbium (Yb^{3+}) ions, where the passivation effect of Yb^{3+} ions significantly reduced defect density and improved photostability. A photodetector based on this material exhibited dual-band response in the ultraviolet and near-infrared regions. The study showed that the device achieved a responsivity of 1.96 A/W at 440 nm and 0.12 mA/W at 980 nm, corresponding detectivities of 5×10^{12} and 2.15×10^{9} Jones,

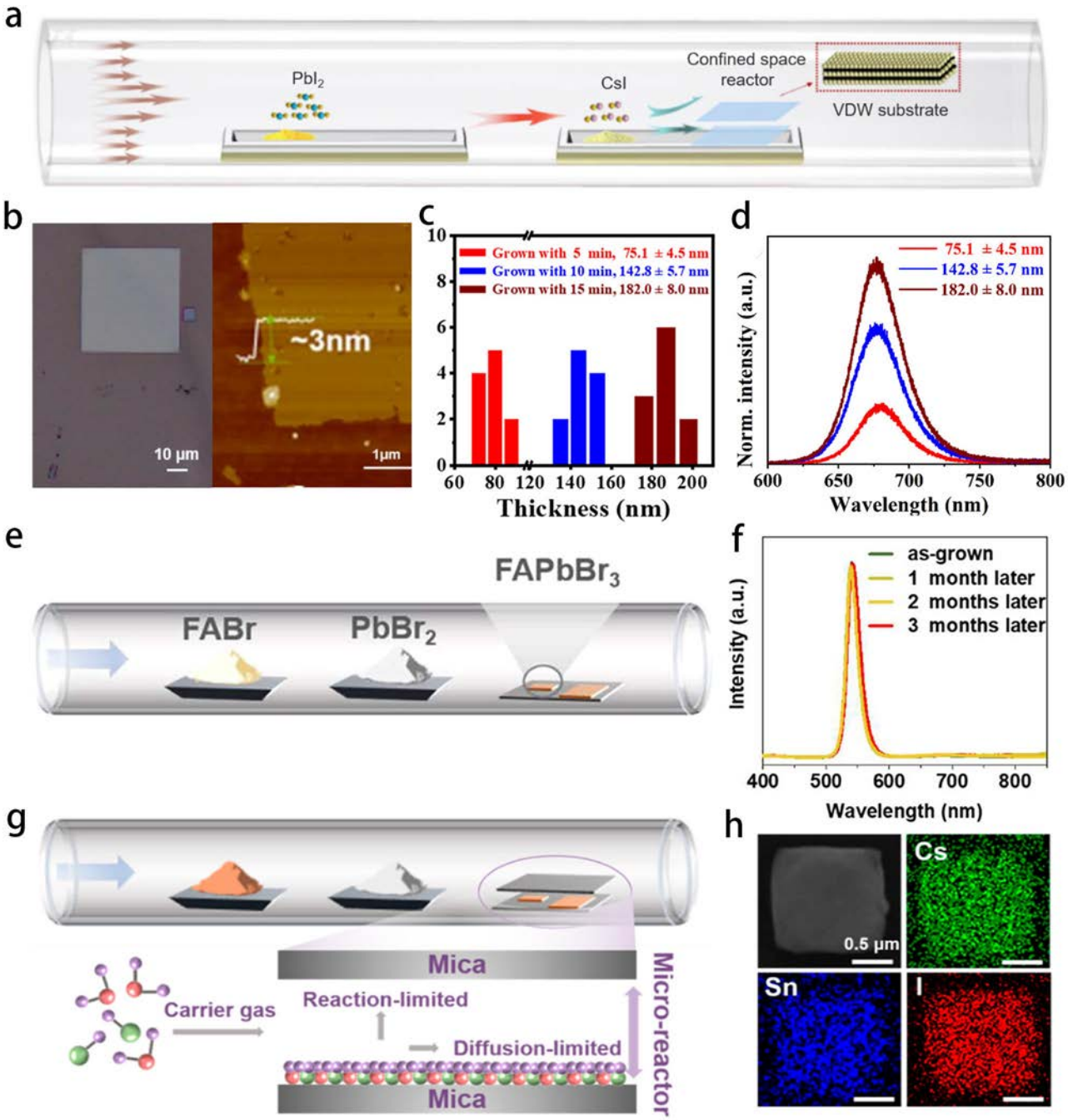

Fig. 19 | CVD method for synthesizing perovskite NSs. a Schematic illustration of the CVD synthesis process for $CsPbI_3$ NSs. **b** Optical image and typical AFM image of $CsPbI_3$ perovskite NSs. **c** Thickness distribution statistics of the synthesized $CsSnBr_3$ NSs. **d** PL spectra of $CsSnBr_3$ NSs with different thicknesses. **e** Schematic illustration of the CVD synthesis of $FAPbBr_3$ NSs. **f** PL spectra of $FAPbBr_3$ NSs after exposure to air for different durations. **g** Schematic representation of the spatially confined CVD growth process of $CsSnI_3$ NSs. **h** SEM and EDS images of $CsSnI_3$ NSs. **a, b** Reproduced with permission from ref. 229. Copyright 2021, American Chemical Society; **c**, **d** Reproduced with permission from ref. 230. Copyright 2021, American Chemical Society; **e**, **f** Reproduced with permission from ref. 231. Copyright 2024, American Chemical Society; **g**, h Reproduced with permission from ref. 232. Copyright 2024, American Chemical Society.

respectively[236]. These results highlight the material's excellent multi-wavelength response capability and long-term photostability.

In addition, research on ultraviolet photodetectors has also received widespread attention. Lv et al. reported lead-free $Cs_3Cu_2I_5$ perovskite NSs and applied them to ultraviolet photodetectors. The study demonstrated that the device exhibited a responsivity of 2.06 A/W at a wavelength of 365 nm (Fig. 20b), along with fast response speeds (142/182 ms) (Fig. 20c) and good stability. Compared to traditional lead-based perovskite materials, $Cs_3Cu_2I_5$ is non-toxic and exhibits high optoelectronic performance, showing great potential for environmental applications[237]. In further research, Ba et al. successfully prepared $Cs_2PbI_2Cl_2$ NSs using a two-step dipping method (Fig. 20d) and applied them to self-powered ultraviolet photodetectors (Fig. 20e), demonstrating outstanding optoelectronic performance. The detector's responsivity was 35.01 mA/W, with a detectivity of 2.45×10^{12} Jones and a response time of only 80 μs, indicating excellent ultraviolet light detection capability. These performance improvements were primarily attributed to the suppression of carrier recombination and the enhanced built-in electric potential[238].

Combining perovskites with other materials has significantly enhanced the photodetectors' performance. Chen et al. developed a photodetector

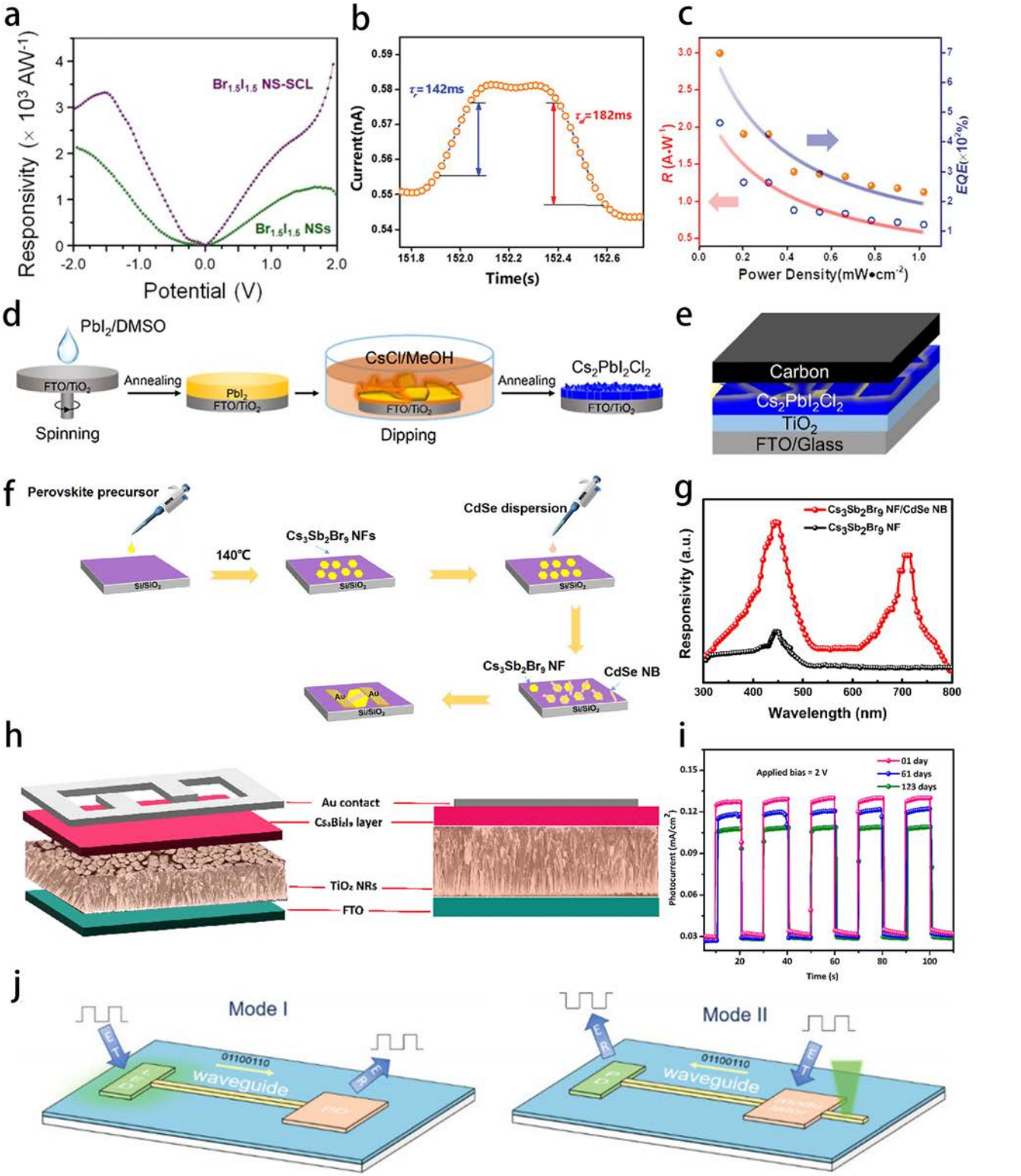

Fig. 20 | Application of perovskite NSs in photodetectors. a Response rate of the device based on $CsPbBr_{1.5}I_{1.5}$ NSs. **b** Rise and fall times of the device. **c** The relationship between responsivity, EQE, and light intensity. **d** Schematic diagram of the preparation process for $Cs_2PbI_2Cl_2$ NSs. **e** Schematic diagram of the self-powered photodetector structure based on $Cs_2PbI_2Cl_2$ NSs. **f** Preparation flowchart for $Cs_3Sb_2Br_9$/CdSe photodetector. **g** Spectral response rates of the Cs3Sb2Br9 device and the $Cs_3Sb_2Br_9$/CdSe device under a 3 V bias. **h** Schematic of the $Cs_3Bi_2I_9/TiO_2$ heterostructure perovskite photodetector. **i** Long-term stability test of the device. **j** Schematic diagram of the design of a bidirectional optoelectronic device. **a** Reproduced with permission from ref. 235. Copyright 2021, American Chemical Society; **b**, **c** Reproduced with permission from ref. 237. Copyright 2022, John Wiley and Sons; **d**, **e** Reproduced with permission from ref. 238. Copyright 2025, American Chemical Society; **f**, **g** Reproduced with permission from ref. 239. Copyright 2022, American Chemical Society; **h**, **i** Reproduced with permission from ref. 227. Copyright 2025, Royal Society of Chemistry; **j** Reproduced with permission from ref. 241. Copyright 2024, AIP Publishing.

with a broad spectral response from 300 to 780 nm by combining lead-free $Cs_3Sb_2Br_9$ perovskite NSs with CdSe nanoribbons (Fig. 20f, g). The heterostructure facilitated the efficient separation of electron-hole pairs, significantly improving the optoelectronic performance. Under illumination at 448 nm, the device exhibited a responsivity of up to 174 A/W and a detectivity of 1.1×10^{14} Jones[239]. Ansari et al. proposed a photodetector based on a heterojunction of RP perovskite $(BA)_2(MA)_{n-1}Pb_nI_{3n+1}$ with MoS_2 NSs. Including MoS_2 effectively improved the crystallinity and surface morphology of the RP perovskite NSs films, enhancing light absorption and charge transport properties by reducing defects and voids. Under 1 sun illumination, the photogenerated current density was 9.8 μA/cm^2, 16 times higher than that of the photodetector without MoS_2[240]. Additionally, Ashokan et al. grew 2D $Cs_3Bi_2I_9$ perovskite NSs on TiO_2 NR arrays using CVD to form a heterojunction and studied its application in photodetectors (Fig. 20h). This photodetector exhibited a wide spectral response in the visible light range from 450 to 750 nm, with a responsivity of 1.1 A/W and a detectivity of 1.969×10^{11} Jones. In terms of temperature stability, the device maintained good optoelectronic performance even at temperatures as high as 75 °C, and after 123 days of testing, the photocurrent decayed by only 15.63% (Fig. 20i), demonstrating its excellent long-term stability[227]. In terms of device integration, Tan et al. designed a bidirectional optoelectronic device that not only emits light but also has modulation and detection functions (Fig. 20j). By integrating $CsPbBr_3$ NPLs for light emission with CdS nanobelts as optical waveguides, the researchers successfully achieved both light signal emission and reception. This bidirectional optoelectronic device demonstrates excellent modulation depth and response speed, showcasing its potential for applications in optoelectronic integrated circuits[241]. Wang et al. reported a 10×10 flexible photodetector array based on quasi-2D $(BA)_2FAPb_2I_7$ for optical imaging. By annealing with gold nanoparticles to enhance crystallinity and using formamidinium chloride post-treatment to reduce defects, combined with SiO_2-assisted hydrophilic-hydrophobic patterning, a large-area, highly uniform pixel array was realized on a flexible substrate. The array exhibits high responsivity, a broad spectral response range, and excellent mechanical stability[242]. This research provides strong support for the large-scale integration and application of perovskite photodetector arrays.

Photocatalysis. 2D halide perovskite NSs have also shown numerous unique advantages in photocatalytic CO_2 reduction reactions[243]. Their large specific surface area and high light absorption capability allow for efficient photon absorption in the visible light region[244]. Besides, the unique layered structure provides more active sites, enhancing the contact between reactants and the catalyst, thereby facilitating CO_2 adsorption and activation[245]. Furthermore, 2D halide perovskite materials can also improve catalytic efficiency and stability by designing heterojunction structures or introducing auxiliary materials[246].

Wu et al. investigated the application of 2D MHP NSs in photocatalytic CO_2 reduction. They synthesized $CsPbBr_{3-3x}I_{3x}$ NSs at room temperature using a simple method. The study showed that compared to traditional MHP NCs, the synthesized NSs exhibited higher stability and stronger photocatalytic CO_2 reduction activity. Through a halide ion regulation strategy, it was found that $CsPbBr_{2.4}I_{0.6}$ NSs had the highest electron consumption rate of 87.8 μmol g^{-1} h^{-1} (Fig. 21a), which is seven times higher than that of traditional MHP NCs[247]. Liu et al. reported a novel method for synthesizing lead-free perovskite material Cs_2AgBiX_6 (X = Cl, Br, I) NSs and investigated their application in CO_2 photocatalytic reduction. The results showed that $Cs_2AgBiBr_6$ (CABB) NSs exhibited higher CO_2 reduction activity than traditional nanocubes. This study represents the first lead-free double perovskite materials application in 2D photocatalysis, offering a more environmentally friendly option for photocatalytic applications[33]. In further research, Zhao et al. reported a method for anchoring a series of cobalt phthalocyanine catalysts onto lead-free perovskite $Cs_2AgBiBr_6$ NSs. They finely controlled the anchoring of the cobalt catalysts to enhance the CO_2 photocatalytic reduction efficiency (Fig. 21b). The study demonstrated that the photogenerated electrons at the Bi sites in $Cs_2AgBiBr_6$ were transferred to the cobalt catalysts via carboxyl group anchoring (Fig. 21c), thereby improving the interfacial electron transfer efficiency and significantly enhancing the photocatalytic performance. The CoTCPc@CABB composite catalyst assembled by carboxyl group anchoring achieved optimal performance, exhibiting an electron consumption rate of 300 μmol g^{-1} h^{-1} in CO_2 reduction (Fig. 21d), which is eight times higher than that of unmodified $Cs_2AgBiBr_6$[248]. This study provides a new approach for enhancing the CO_2 catalytic performance of perovskite 2D materials.

The combination of perovskite materials with other semiconductors can further enhance the efficiency of CO_2 reduction. Yuan et al. employed an in situ growth strategy using $SrTiO_3$ NSs as a substrate to construct a 2D/2D $CsPbBr_3/SrTiO_3$ heterostructure. The lattice matching between $CsPbBr_3$ and $SrTiO_3$, as well as the alignment of their energy band structures, effectively promoted interfacial charge separation in the heterostructure (Fig. 21e). Additionally, NH_4F etching treatment of $SrTiO_3$ further accelerated the charge transfer rate. Ultimately, the constructed 2D/2D T-$SrTiO_3/CsPbBr_3$ heterostructure demonstrated excellent CO_2 photocatalytic reduction activity, with a CO production rate of 120.2 μmol g^{-1} h^{-1} under a light intensity of 100 mW/cm^2 (Fig. 21f), which is about 10 times and 7 times higher than that of pure $SrTiO_3$ and $CsPbBr_3$ NSs, respectively[249]. Furthermore, Feng et al. synthesized $Cs_3Bi_2I_9$ NSs using a self-template directional method. They formed a Z-scheme heterojunction catalyst by electrostatic self-assembly with CeO_2 NSs (Fig. 21g) to promote the CO_2 reduction reaction. The energy level matching between $Cs_3Bi_2I_9$ and CeO_2 NSs (Fig. 21h), along with their close interface contact, significantly improved the separation efficiency of photogenerated charge carriers. The study found that $Cs_3Bi_2I_9/CeO_2$-3:1 exhibited the highest efficiency in CO_2 reduction(Fig. 21i), leading the field in CO_2 reduction yields for bismuth-based perovskite photocatalysts[250]. In further research, Jiang et al. reported an S-type heterojunction catalyst combining $Cs_2AgBiBr_6$ NSs with 2D nickel-based metal-organic frameworks (Ni-MOFs) (Fig. 21j) to enhance CO_2 photocatalytic reduction performance. This structure facilitates the separation of photogenerated charge carriers, and Ni-MOF significantly enhances CO_2 adsorption capability by increasing surface active sites. Experimental results showed that the $Cs_2AgBiBr_6$/Ni-MOF heterojunction exhibited excellent catalytic performance in the photocatalytic CO_2 reduction reaction, being 6.43 times and 8.79 times more efficient than the individual $Cs_2AgBiBr_6$ and Ni-MOF, respectively (Fig. 21k). Additionally, it demonstrated excellent photocatalytic stability[251].

In summary, halide perovskite NSs have demonstrated immense potential in applying photocatalytic CO_2 reduction. Researchers have made significant progress in enhancing photocatalytic efficiency and stability by optimizing material structures, preparation methods, and catalyst combinations.

Solar cells and LEDs. 2D halide perovskite NSs, with their efficient optoelectronic conversion properties, excellent processability, good flexibility, and high stability, are promising in solar cell application[252,253]. Bathula et al. synthesized quasi-2D perovskite NSs $(DDA)_2[FAPbI_3]_{n-1}PbI_4$ (Fig. 22a) using a mechanochemical method and studied their application in perovskite solar cells. They successfully reduced phase separation and improved stability through a solvent-free synthesis strategy. Based on this material, the solar cell achieved an open-circuit voltage (V_{OC}) of 0.961 V, a short-circuit current density (J_{SC}) of 23.41 mA cm^{-2}, and a PCE of 15.23%. However, compared to current high-efficiency perovskite solar cells, there is still room for improvement[254]. In interface engineering, Zhu et al. reported a strategy for optimizing the interface of 3D/2D perovskite solar cells by introducing ultrathin $(PEA)_2PbI_4$ NSs between the 3D $MAPbI_3$ and the hole transport layer. They found that the 2D perovskite NSs effectively optimized the energy band structure (Fig. 22b), improving hole extraction efficiency and reducing interfacial charge recombination. Using this method, the PCE of the perovskite solar cell increased from 15.40% to 18.53% (Fig. 22c)[253]. Liu et al. proposed a method for passivating $CsPbI_3$

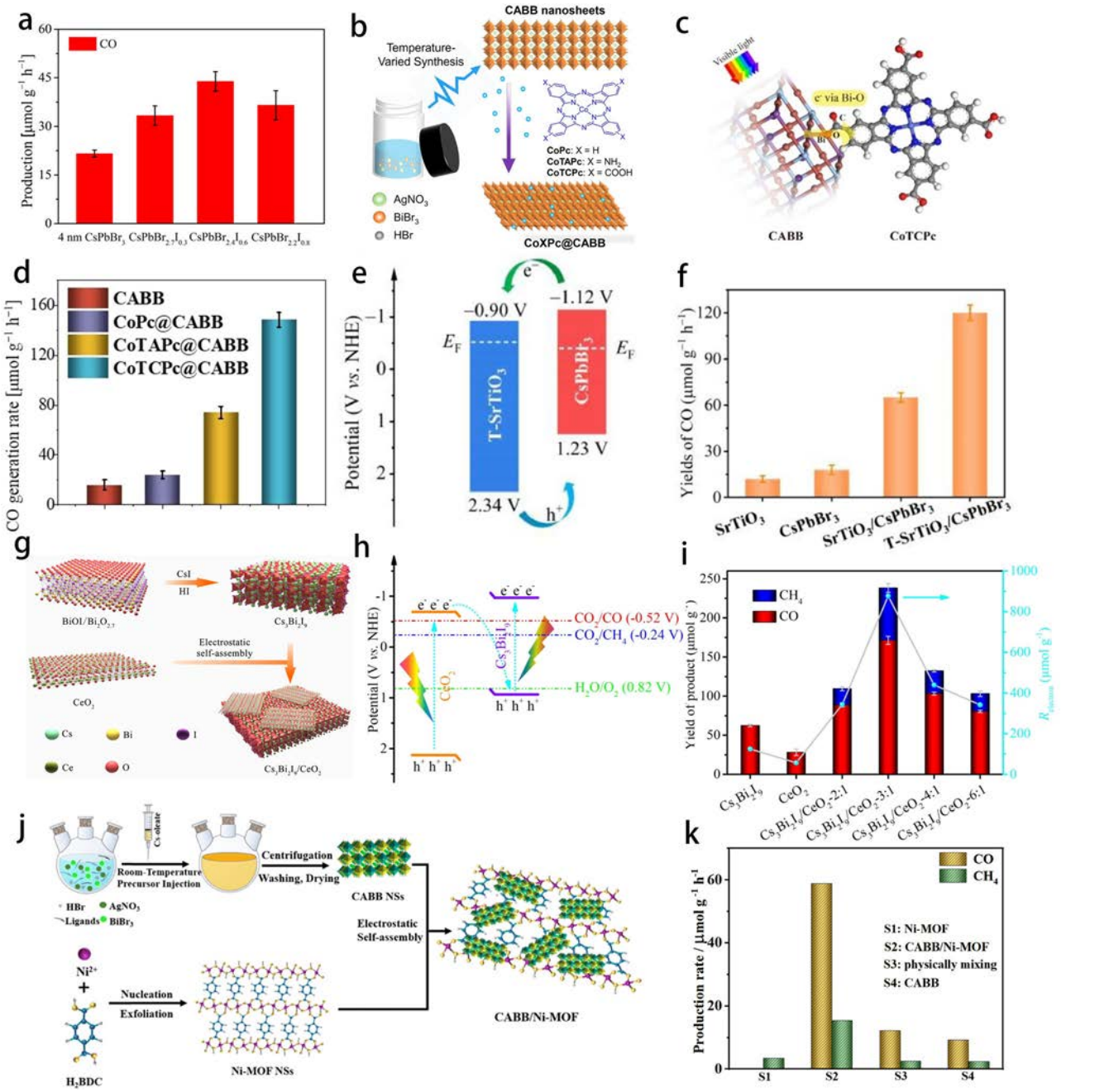

Fig. 21 | Application of perovskite NSs in photocatalysis. **a** Comparison of CO release from $CsPbBr_{3-3x}I_{3x}$ NSs. **b** Synthesis scheme for the combination of CABB and cobalt catalysts. **c** Expected binding model for CoTCPc@CABB. **d** Photocatalytic CO production rates for CABB, CoPc@CABB, CoTAPc@CABB, and CoTCPc@CABB. **e** Energy band diagrams of T-$SrTiO_3$ and $CsPbBr_3$ before contact. **f** CO production rates for $SrTiO_3$, $CsPbBr_3$, $SrTiO_3$/$CsPbBr_3$, and T-$SrTiO_3$/$CsPbBr_3$ as photocatalysts. **g** Preparation of $Cs_3Bi_2I_9$ NSs and their self-assembly with CeO_2 NSs. **h** Schematic illustration of the band alignment between $Cs_3Bi_2I_9$ and CeO_2. **i** Catalytic CO_2 production of $Cs_3Bi_2I_9$, CeO_2, and $Cs_3Bi_2I_9$/CeO_2 − x:1. **j** Schematic diagram of the electrostatic self-assembly process of 2D/2D CABB/Ni-MOF hybrid materials. **k** CO_2 reduction photocatalytic performance of CABB, Ni-MOF, CABB/Ni-MOF, and physically mixed samples. **a** Reproduced with permission from ref. 247. Copyright 2021, John Wiley and Sons; **b**–**d** Reproduced with permission from ref. 248. Copyright 2024, John Wiley and Sons; **e**, **f** Reproduced with permission from ref. 249. Copyright 2023, Elsevier; **g**, **h**, **i** Reproduced with permission from ref. 250. Copyright 2021, Elsevier; **j**, **k** Reproduced with permission from ref. 251. Copyright 2023, Royal Society of Chemistry.

QD solar cells using 2D $Cs_2PbI_2Cl_2$ NSs (Fig. 22d). By introducing a $Cs_2PbI_2Cl_2$ NS-based overlayer, the surface properties of the $CsPbI_3$ QD thin films were significantly improved. The optimized $CsPbI_3$ QDs solar cell achieved a PCE of 14.73% (Fig. 22e), and after exposure to a humid environment for 432 hours, the efficiency loss was only 16% (Fig. 22f)[252]. Although this method enhanced the stability, further efficiency improvements are needed to compete with the current best perovskite solar cells. In another study, Liu et al. introduced an organic spacer molecule containing multiple nitrogen sites (1H-Pyrazole-1-carboxamidine hydrochloride, PAH) to form a 2D perovskite passivation layer on the surface of $FAPbI_3$. Due to the interaction between PAH and PbI_2, defects in the $FAPbI_3$ perovskite were effectively passivated. Additionally, the multiple-site interactions facilitated the vertical growth of the NSs on the substrate (Fig. 22g), which promoted charge transfer. This strategy enabled the 2D/3D solar cell to achieve a PCE of 24.6% and excellent stability (Fig. 22h, i)[255].

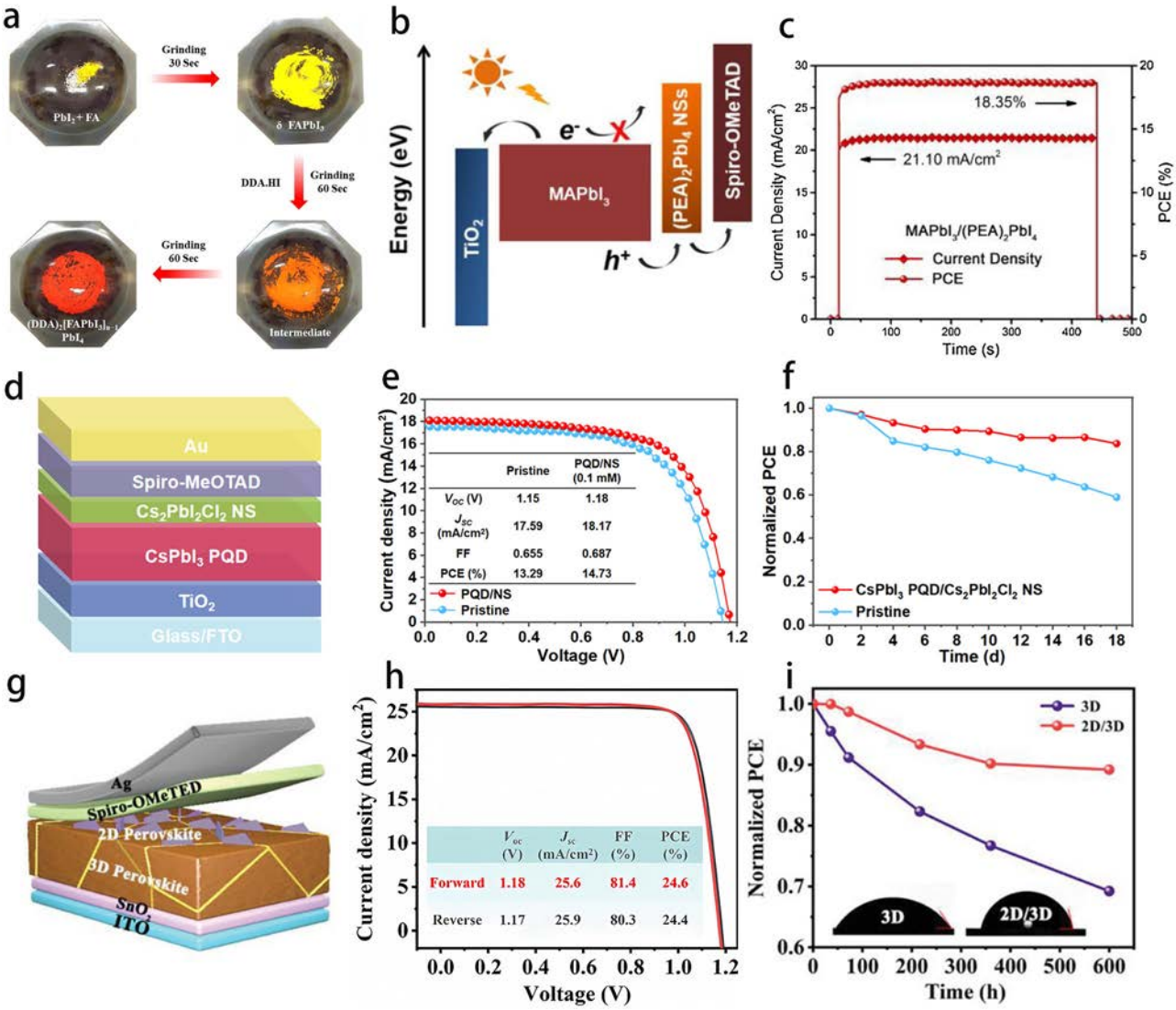

Fig. 22 | Application of perovskite NSs in Solar cells. a Schematic diagram of the solvent-free solid-state synthesis of $(DDA)_2[FAPbI_3]_{n-1}PbI_4$ NSs. **b** Energy level diagram of the 3D/2D $MAPbI_3/(PEA)_2PbI_4$ perovskite solar cell. **c** Photocurrent density and PCE of the $MAPbI_3/(PEA)_2PbI_4$ perovskite solar cell. **d** Schematic perovskite solar cell structure diagram with FTO/TiO_2/$CsPbI_3$ PQD/$Cs_2PbI_2Cl_2$ NS/Spiro-MeOTAD/Au conFiguration. **e** J-V curves and other data of the perovskite solar cell, including PCE. **f** Stability test of the original $CsPbI_3$ and $CsPbI_3$ PQD/$Cs_2PbI_2Cl_2$ NS perovskite solar cell under storage conditions at 30 ± 5% RH. **g** Schematic diagram of the 2D/3D perovskite solar cell structure. **h** J-V curves and other data of the 3D and 2D/3D devices, including PCE. **i** Long-term stability test of the unencapsulated 3D and 2D/3D devices. **a** Reproduced with permission from ref. 254. Copyright 2021, Elsevier; **b**, **c** Reproduced with permission from ref. 253. Copyright 2021, Elsevier; **d**–**f** Reproduced with permission from ref. 252. Copyright 2024, American Chemical Society; **g**, **h**, **i** Reproduced with permission from ref. 255. Copyright 2023, John Wiley and Sons.

Compared to traditional 3D perovskite materials, 2D perovskite NSs exhibit stronger quantum confinement effects, higher PLQY, and lower ion migration, making them highly promising for efficient and stable LEDs[256]. Additionally, the emission wavelength of 2D perovskite materials can be easily tuned by adjusting the number of layers and incorporating different organic ligands or inorganic ions, enabling their application in LEDs of various colors[257]. Wang et al. synthesized a series of alkylammonium lead iodide perovskite monolayer NSs ($(RNH_3)_3PbI_4$, R = $C_{18}H_{35}^-$, $C_{12}H_{25}^-$, $C_8H_{17}^-$) via a self-assembly method (Fig. 23a). These NSs exhibit tunable green PL with emission wavelengths ranging from 505 to 536 nm (Fig. 23b) and a narrow emission linewidth of less than 16 nm, as well as excellent water stability. Studies have shown that the synthesized monolayer NSs are highly compatible with $CsPbI_3$ red-emitting QDs, thereby mitigating the common issue of halide ion exchange. By combining these green monolayer NSs with red-emitting $CsPbI_3$ QDs, a white-light LED device was fabricated (Fig. 23c), achieving chromaticity coordinates of (0.32, 0.33) and a correlated color temperature of 6000 K. The resulting device exhibited a color gamut coverage of 117% NTSC, demonstrating outstanding performance[258]. Additionally, Gao et al. proposed a strategy combining copper (Cu^{2+}) doping and post-treatment Br- anion exchange to address the issues of low PLQY and environmental instability in deep blue LEDs. Cu^{2+} doping significantly reduced chlorine defects in the material and successfully transformed the originally inefficient $CsPbCl_3$ QDs into two-dimensional NSs with high PL. Through post-treatment bromine ion exchange, the resulting $CsPb(Br/Cl)_3$ NSs exhibited increased radiative recombination and reduced ionic migration, which improved the PLQY to 94% and significantly enhanced humidity stability. The deep blue LEDs fabricated from this material had an emission wavelength of 462 nm, with a maximum brightness of 761 cd/m^2 and a current density of 205 mA/cm^2 (Fig. 22d, e, f)[204]. In further studies, Xu et al. proposed a strategy to enhance the performance and stability of deep blue LEDs by processing perovskite NSs films with choline chloride (ChCl) and rubidium bromide (RbBr) (Fig. 23g). ChCl served as an effective chlorine

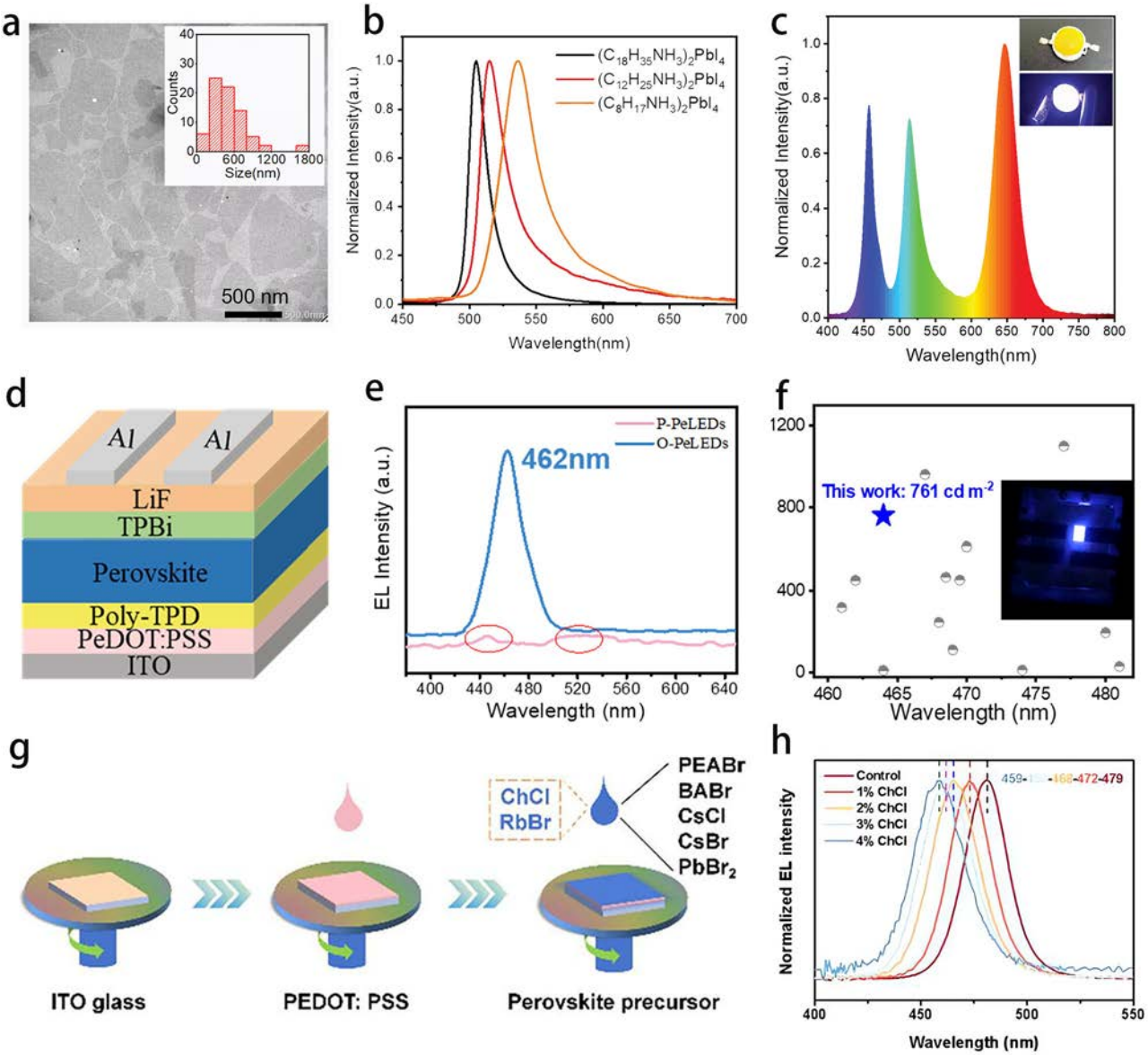

Fig. 23 | Application of perovskite NSs in LEDs. a TEM image of $(C_{18}H_{35}NH_3)_2PbI_4$ NSs. **b** PL spectra of $(C_{18}H_{35}NH_3)_2PbI_4$, $(C_{12}H_{25}NH_3)_2PbI_4$ and and$(C_8H1_7NH_3)_2PbB_4$. **c** EL spectrum of a WLED device made from a monolayer $(C_{12}H_{25}NH_3)_2PbI_4$ sheet and $CsPbI_3$ QDs on a 450 nm blue-emitting chip. **d** Schematic diagram of the device structure of a perovskite LED. **e** EL spectra of P-PeLED and O-PeLED. **f** Comparison of the brightness of this work with that of previously reported works. **g** Schematic diagram of the perovskite NSs film preparation process. **h** EL spectra of LEDs treated with different concentrations of ChCl. **a**–**c** Reproduced with permission from ref. 258. Copyright 2022, John Wiley and Sons; **d**–**f** Reproduced with permission from ref. 204. Copyright 2021, Elsevier; **g**, **h** Reproduced with permission from ref. 256. Copyright 2024, American Chemical Society.

source to fill halogen vacancies and acted as a passivator to suppress deep-level defects in the perovskite NSs, thereby reducing non-radiative recombination and significantly improving PLQY. Moreover, introducing RbBr reduced ionic migration and stabilized the perovskite phase, further enhancing the photoluminescent properties and device stability. The LEDs based on this material successfully achieved deep blue emission, with a maximum EQE of 3.58% (Fig. 23h)[256]. In summary, applying 2D halide perovskite NSs in LEDs demonstrates significant advantages. By adjusting the material size, doping strategy, and passivation methods, researchers have successfully enhanced the luminescent efficiency and stability of the devices.

Theoretical design strategies

Density functional theory

Understanding the relationship between the atomic structure of halide perovskites and their resulting electronic and optical properties is crucial for optimizing their performance. Density Functional Theory (DFT), a quantum mechanical computational method, has become an invaluable tool in this regard[259]. DFT enables detailed simulations of atomic and electronic interactions in halide perovskites, providing essential insights into their structural stability, electronic properties, and defects[260,261]. This computational approach also allows for predicting key characteristics such as band gaps, density of states, charge transport, and exciton dynamics, which are critical for designing more efficient devices[262,263]. Ahmed et al. studied lead-free mixed halide perovskites based on gallium, $Cs_3GaI_{6-x}Br_x$, and explored their structural, electronic, and optical properties for photovoltaic applications using DFT. These compounds exhibit good structural stability, with band gaps ranging from 1.319 to 1.779 eV. The optical absorption coefficients suggest that these materials have potential for use in solar cells, with $Cs_3GaI_4Br_2$ and Cs_3GaI_5Br emerging as the most promising materials[264]. Bouhmaidi et al.

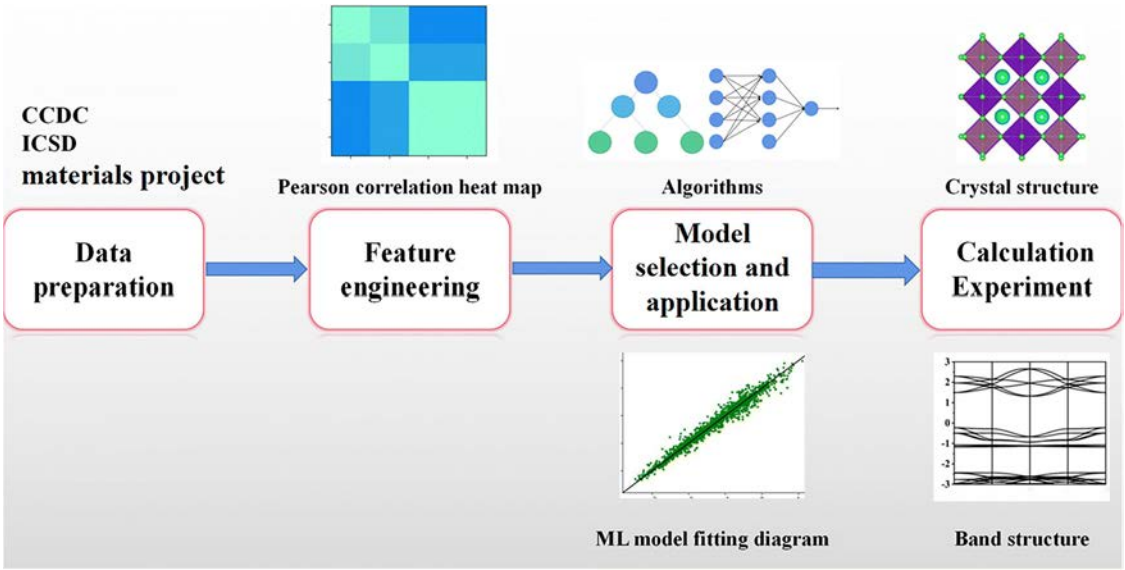

Fig. 24 | Research process of machine learning for perovskite materials. Schematic diagram of a typical workflow for studying perovskite materials using ML methods. Reproduced with permission from ref. 274. Copyright 2022, Royal Society of Chemistry.

investigated the structural, electronic, optical, and thermoelectric properties of germanium-based halide perovskites, $CsGeX_3$ (X = F, Cl, Br). Through DFT calculations and semi-classical Boltzmann transport theory, the study found that these perovskites possess direct band gaps and strong ultraviolet absorption, with $CsGeBr_3$ exhibiting a high Seebeck coefficient, indicating its potential for thermoelectric applications[265]. The optimization of device performance using DFT has also been widely studied. Chen et al. examined the effects of pseudo-halogen anions on the surface of $FAPbI_3$ and the $SnO_2/FAPbI_3$ heterostructure, exploring their application in solar cells. DFT calculations revealed that pseudo-halogen anions can enhance the stability of the $FAPbI_3$ surface and improve the light absorption and charge transport properties at the $SnO_2/FAPbI_3$ interface, thus boosting the device performance[266]. In further research, Adam et al. combined experimental and DFT analysis to investigate the impact of potassium halides on the $SnO_2/MAPbI_3$ interface. The study found that potassium halides can passivate surface defects, increase the perovskite grain size, and improve the adhesion and charge extraction properties of the SnO_2/perovskite interface. Moreover, devices treated with potassium halides exhibited higher PCE and stability[267].

DFT has proven to be a powerful tool for understanding the complex properties of LHPs. By offering in-depth insights into the electronic structure, defects, exciton dynamics, and other key features, DFT has contributed to optimizing and designing more efficient and stable perovskite devices[268,269]. As computational power continues to grow, DFT will remain indispensable in the future development of LHPs, enabling the exploration of new materials and guiding the design of next-generation optoelectronic devices.

Machine learning

Perovskite nanomaterials, owing to their tunable bandgap, high charge carrier mobility, and solution processability, have emerged as promising candidates for next-generation optoelectronic devices such as solar cells, LEDs, and photodetectors[19,209,270]. However, their performance is governed by multiple factors, including composition, lattice structure, defect states, and processing parameters[271]. This multidimensional coupling poses significant challenges to the conventional trial-and-error research paradigm, which suffers from low efficiency and high costs. As a core branch of artificial intelligence, machine learning (ML) offers a transformative tool for the full spectrum of perovskite material research—from design and synthesis to device application—by uncovering hidden patterns in high-dimensional data[272,273]. This shift is catalyzing a paradigm transition from experience-driven to data-driven scientific discovery.

ML demonstrates remarkable advantages in predicting the optoelectronic properties of perovskite nanomaterials by constructing structure-property mapping models, leveraging feature engineering, and selecting appropriate algorithms[274]. The core workflow (Fig. 24) involves collecting material composition data from experimental or computational databases, identifying key descriptors through feature engineering, training predictive models using supervised learning algorithms, optimizing performance based on validation metrics, and ultimately deploying the models to predict the properties of new materials or devices[275,276]. Compared with traditional approaches, ML excels in high-throughput virtual screening, nonlinear relationship analysis, and inverse design capabilities, significantly accelerating the discovery and design of materials with desired functionalities[277,278]. In terms of precise predictions at the material level, ML has achieved in-depth analysis of stability, optoelectronic properties, and defect behaviors[271]. Hu et al. combined high-throughput calculations with machine learning to study the ion adsorption characteristics of 2D halide perovskites for energy storage applications. Using multiple ML algorithms for prediction and screening, they found that the Xgboost algorithm performed best in prediction accuracy and successfully identified promising lead-free perovskites for energy storage applications[279]. Gupta et al. used ML and experimental databases to explore novel oxide and halide perovskites, focusing on their formability and stability. They trained machine learning models on 1962 oxide perovskites and 4,075 halide perovskites, successfully predicting 591 materials with both formability and stability, and analyzed their potential applications in batteries, further advancing the use of perovskite materials in energy storage[280]. In subsequent research, Mishra et al. combined experimental and ML approaches by establishing a comprehensive database of perovskites and using it to predict 10,920 possible perovskite combinations. They then selected Cs_2PbSnI_6 for synthesis, prepared its NCs using a hot-injection method, and characterized their optical properties using XRD and TEM. The experimental results were consistent with the machine learning-predicted band gap, demonstrating the effectiveness of this approach in material design[281]. Furthermore, the application of ML can be extended to the prediction of optoelectronic device performance. Meftahi et al. optimized the fabrication process of quasi-2D RP perovskite films using automated robotic manufacturing technology. They combined it with a ML model to predict photovoltaic performance, successfully increasing the PCE to 16.9%[282].

These studies show that the combination of high-throughput calculations and ML accelerates the screening and optimization of perovskite materials and provides valuable guidance in material design and

performance prediction, laying a solid foundation for the future development of optoelectronic devices.

Summary and outlook

Summary

In conclusion, LHPs have shown significant potential for applications in optoelectronics due to their unique quantum confinement effects, tunable band gaps, and excellent carrier dynamics properties[283]. In this review, we comprehensively discuss the properties and advantages of LHPs. Additionally, we summarize the commonly used synthesis methods for LHPs, including hot injection, ligand-assisted reprecipitation, and vapor deposition techniques, which enable control over the morphology and size of the nanostructures. Finally, we introduce the recent research on the applications of low-dimensional halide perovskites in LEDs, solar cells, photodetectors, and lasers.

Challenges and prospects

However, the commercialization of LHPs and their devices still faces several core challenges:

1. Although LHPs exhibit better stability than conventional 3D perovskites in certain aspects, their long-term environmental stability remains a major obstacle to commercial application. Under prolonged bias or continuous illumination, devices are prone to ion migration, enhanced non-radiative recombination, and local phase transitions, ultimately leading to performance degradation[284]. Moreover, the high specific surface area of LHPs intensifies interfacial reactions with environmental species, particularly moisture and oxygen, resulting in irreversible processes such as photo-oxidation, hydrolysis, or ligand dissociation[285]. These degradation pathways often produce amorphous phases or intermediate states, causing bandgap shifts and reduced photoelectric conversion efficiency[286]. To systematically address these stability challenges, future research should proceed on multiple fronts: on one hand, by employing precise ligand engineering, elemental doping, and defect passivation strategies to enhance ionic migration barriers and improve both structural and electronic stability within the crystal; on the other hand, by developing compact, interface-compatible encapsulation materials or dynamic ligand systems to restrict the ingress and reactivity of external environmental factors effectively.
2. Lead-based LHPs, especially those composed of Pb^{2+}, such as NCs, NWs, and NSs, offer distinct performance advantages. However, lead is a heavy metal with high bioaccumulation potential and water-soluble toxicity, and the risk of lead leakage after the end-of-life of devices has raised widespread concerns[287]. In terms of lead leakage prevention, constructing multilayer inorganic/organic composite encapsulation structures can significantly enhance the device's stability in humid environments and prevent the migration and release of lead ions[288]. Additionally, incorporating lead chelating agents or phosphate-based fixatives within the material can effectively capture any released lead by forming stable complexes or precipitates, thereby reducing its bioavailability[111]. The development of lead-free perovskites has also become an important research direction. Typical substitution strategies involve partially or fully replacing Pb^{2+} with low-toxicity or non-toxic ions such as Sn^{2+}, Bi^{3+}, Sb^{3+}, Cu^{+}, or Mn^{2+}. However, Sn^{2+} is highly prone to oxidation into Sn^{4+}, which greatly compromises stability and device performance[289]. Although Bi^{3+} and Sb^{3+} perovskites offer higher stability, their indirect band gaps and low carrier mobility limit their optoelectronic properties[290]. Therefore, future research should continue to advance fundamental studies on lead-free perovskite alternatives while also accelerating the development of efficient, low-cost, and scalable lead leakage prevention technologies.
3. The optoelectronic properties of LHPs are strongly dependent on their dimensionality, size, and anisotropy. However, precise control over the nanostructure dimensions (such as diameter, thickness, and aspect ratio) during the synthesis process remains a significant challenge[291]. Although widely used for preparing perovskite nanomaterials, traditional colloidal synthesis methods struggle to achieve monodispersity due to the fast crystallization kinetics[292]. The high-temperature environment of CVD processes directly conflicts with the low thermal stability of perovskites, often resulting in the formation of amorphous or mixed phases. Furthermore, the difference in thermal expansion coefficients between the substrate and the perovskite can lead to lattice distortion at the interface[293]. Therefore, further investigation into the nucleation and growth mechanisms of LHP nanomaterials is needed, focusing on kinetic regulation, ligand engineering, and template design to control their size precisely.
4. Significant progress has been made in studying surface passivation of 0D perovskite NCs through ligand engineering. However, the interaction between the ligand and the surface of perovskite NCs is relatively weak, and this interaction is highly dynamic[294]. As a result, ligands are prone to detachment during solution processing, exposing surface dangling bonds and forming deep-level defects, significantly reducing carrier mobility by 1-2 orders of magnitude[295]. Therefore, exploring novel ligands and gaining a deeper understanding of their functions will remain key areas of future research.
5. The interfacial issues between LHPs and other functional layers often determine the device's overall performance. Due to interfacial defects and inhomogeneities, charge injection and extraction are frequently limited, resulting in lower device efficiency and poor stability[296]. To address this problem, future research should focus on optimizing interface engineering. Introducing novel interfacial materials allows it to effectively tune energy level alignment and improve charge carrier injection and transport[297]. Additionally, surface modification or self-assembly techniques can reduce interfacial defect density and suppress non-radiative recombination[298]. Moreover, designing interfacial dipole layers or energy gradient layers can further optimize electron transport and interfacial electric field distribution, thereby enhancing the device's efficiency and stability.
6. In the multilayer structure of LHP devices, interlayer compatibility is a major challenge. Due to differences in the physicochemical properties of various materials, especially mismatches in solvents, thermal expansion coefficients, and lattice structures, issues such as solvent incompatibility, chemical reactions, or thermal stress accumulation may occur between layers, affecting the overall performance and stability of the device[299]. To address these challenges, researchers are exploring novel interlayer compatibility strategies, particularly between different types of perovskite and non-perovskite materials[300]. The mutual impact between layers can be effectively avoided by selecting appropriate solvent systems, interfacial materials, and buffer layers. Additionally, heterojunctions in multi-dimensional structures (such as 0D/2D and 1D/3D) have enhanced photoelectric conversion efficiency[8].
7. Due to the high sensitivity of LHPs to external environments, encapsulation technology is particularly critical. Traditional encapsulation methods, such as glass or resin encapsulation, often fail to meet the application requirements of low-dimensional perovskite devices in areas like flexible electronics and wearable devices[301]. In particular, under harsh conditions such as humidity, high temperatures, and UV exposure, conventional encapsulation materials often cannot provide sufficient protection[302]. Future encapsulation strategies should place greater emphasis on material compatibility and multifunctionality. For example, ultra-thin inorganic gas barrier films prepared via atomic layer deposition can effectively prevent the penetration of moisture and oxygen, thereby ensuring device stability[303]. At the same time, developing self-healing encapsulation materials that can automatically repair microcracks can help prevent performance degradation during prolonged exposure[304]. Additionally, innovations in flexible encapsulation materials can significantly extend device lifespan and reduce manufacturing costs.

8. Currently, the large-scale production of LHPs remains a major challenge limiting their commercial application. Although solution-based methods and hot-injection techniques have achieved significant progress at the laboratory scale, these approaches are difficult to adapt to industrial production due to high demands for cost-effectiveness, efficiency, and consistency[305]. A key unresolved issue is maintaining uniformity and high quality of materials during scale-up. To address this, researchers are developing fabrication techniques compatible with roll-to-roll processing, such as hot pressing and inkjet printing, to improve manufacturing throughput[306]. Additionally, the compatibility between solvents and substrates used in the fabrication process, especially from an environmental and sustainability perspective, is another critical aspect that requires optimization[307]. By further refining these processes, the production cost and scalability of LHPs are expected to improve significantly.
9. The potential applications of LHPs in flexible electronics, sensors, and intelligent systems are gradually emerging, and how to achieve compatibility and integration of these materials with other material systems has become a new research direction[308]. Large-scale integration requires excellent optoelectronic performance from LHPs and good thermal stability, electrical compatibility, and processability[309]. Therefore, future research will focus on integrating these materials under low-temperature or low-pressure conditions in a manner compatible with existing CMOS processes and developing multifunctional systems that combine sensing, energy harvesting, and communication[310]. Moreover, new opportunities can be created for future smart electronics and wearable technologies by designing multilayer devices with nanostructured architectures, such as vertically stacked photodetectors and micro-LED arrays.
10. In addition to the inherent toxicity of the materials themselves, the current synthesis processes for LHPs still largely rely on high temperatures, highly toxic solvents, harmful ligands, and heavy metal precursors. This poses safety risks during operation and imposes significant burdens in energy consumption, environmental emissions, and waste management. Therefore, developing green synthesis techniques for perovskite materials is of great importance. The core objectives of green synthesis include using low-toxicity or non-toxic precursors, developing aqueous or alcohol-based synthesis systems, implementing ambient temperature and pressure conditions, reducing organic solvent usage, and improving yield[311]. Recent studies have attempted to synthesize lead-based NCs using water/ethanol solutions or to replace conventional long-chain amine ligands with plant-derived surfactants[312]. In addition, solvent recycling technologies, solid-state synthesis methods, and microwave or photocatalysis-assisted processes are emerging as promising green synthesis pathways[313]. These strategies reduce environmental impact and improve process controllability and reproducibility to some extent. However, green synthesis still faces several challenges. First, green systems' crystallization rate, morphology control, and ligand compatibility are often suboptimal, leading to reduced quantum efficiency or incomplete crystallization[314]. Second, alternative low-toxicity solvents exhibit complex and variable evaporation rates, polarities, and coordination abilities with precursors, and there is currently no unified standard[315]. Future research should focus on theoretical modeling and in situ characterization of crystal growth mechanisms in green systems, and aim to develop a set of general, scalable green synthesis processes.

In summary, further enhancement of the performance of LHPs will depend on the interdisciplinary collaboration between materials science, device integration, and computational simulations. More in-depth fundamental research is needed on carrier dynamics, exciton behavior, and defect physics at the nanoscale. By addressing core issues such as stability, toxicity, and scalable fabrication, LHPs are expected to transition from the laboratory to industrialization, laying the foundation for the next generation of efficient and environmentally friendly optoelectronic devices.

Data availability

No datasets were generated or analysed during the current study.

Received: 1 May 2025; Accepted: 11 September 2025;
Published online: 07 November 2025

References

1. da Cunha, T. R. et al. Transition from light-induced phase reconstruction to halide segregation in $CsPbBr_{3-x}I_x$ nanocrystal thin films. *Acs Appl. Mater. Interfaces* **17**, 14389–14403 (2025).
2. Isikgor, F. H. et al. Molecular engineering of contact interfaces for high-performance perovskite solar cells. *Nat. Rev. Mater* **8**, 89–108 (2023).
3. Chen, S. et al. Transmission electron microscopy of organic-inorganic hybrid perovskites: myths and truths. *Sci. Bull.* **65**, 1643–1649 (2020).
4. National Renewable Energy Laboratory. (n.d.). Best research-cell efficiency chart. Retrieved July 26, 2025, from https://www.nrel.gov/pv/interactive-cell-efficiency.html.
5. Green, M. A. et al. Solar cell efficiency tables (Version 64). *Prog. Photovolt.* **32**, 425–441 (2024).
6. Xiao, Y. & Zhou, C. Solution-processed lead halide perovskite films for application in perovskite solar cells: from coating methods to growth dynamics. *J. Phys. D. Appl. Phys.* **58**, 033001 (2025).
7. Mariotti, S. et al. Interface engineering for high-performance, triple-halide perovskite-silicon tandem solar cells. *Science* **381**, 63–69 (2023).
8. Metcalf, I. et al. Synergy of 3D and 2D perovskites for durable, efficient solar cells and beyond. *Chem. Rev.* **123**, 9565–9652 (2023).
9. Yu, W. et al. Advancements in halide perovskite photonics. *Adv. Opt. Photonics* **16**, 868–957 (2024).
10. Zhang, M. et al. High efficiency tin halide perovskite solar cells with over 1 micrometer carrier diffusion length. *Adv. Funct. Mater.* **34**, 2410772 (2024).
11. Elangovan, N. K. et al. Recent developments in perovskite materials, fabrication techniques, band gap engineering, and the stability of perovskite solar cells. *Energy Rep* **11**, 1171–1190 (2024).
12. Huang, Z. et al. Enhancing the performance of perovskite environmental sensors through the synergistic effect of the natural antioxidant. *Acs Appl. Mater. Interfaces* **17**, 11362–11369 (2025).
13. Li, T. et al. Inorganic wide-bandgap perovskite subcells with dipole bridge for all-perovskite tandems. *Nat. Energy* **8**, 610–620 (2023).
14. Li, X. et al. Exploring nanoscale perovskite materials for next-generation photodetectors: a comprehensive review and future directions. *Nano-Micro Lett* **17**, 28 (2025).
15. Zhu, H. et al. Long-term operating stability in perovskite photovoltaics. *Nat. Rev. Mater* **8**, 569–586 (2023).
16. Wang, S. et al. Perovskite nanocrystals: synthesis, stability, and optoelectronic applications. *Small Struct* **2**, 2000124 (2021).
17. Kong, L. et al. Fabrication of red-emitting perovskite LEDs by stabilizing their octahedral structure. *Nature* **631**, 73–79 (2024).
18. Kumar, V., Kathiravan, A. & Jhonsi, M. A. Beyond lead halide perovskites: Crystal structure, bandgaps, photovoltaic properties, and future stance of lead-free halide double perovskites. *Nano Energy* **125**, 109523 (2024).
19. Otero-Martinez, C. et al. Colloidal metal-halide perovskite nanoplatelets: thickness-controlled synthesis, properties, and application in light-emitting diodes. *Adv. Mater.* **34**, 2107105 (2022).
20. Hautzinger, M. P., Mihalyi-Koch, W. & Jin, S. A-site cation chemistry in halide perovskites. *Chem. Mater.* **36**, 10408–10420 (2024).
21. Yang, J., Fan, J. & Li, S. Mapping the room-temperature dynamic stabilities of inorganic halide double perovskites. *Chem. Mater.* **34**, 9072–9085 (2022).
22. Kim, J. S. et al. Ultra-bright, efficient and stable perovskite light-emitting diodes. *Nature* **611**, 688–694 (2022).

23. Kim, S. et al. 3D meniscus-guided evaporative assembly for rapid template-free synthesis of highly crystalline perovskite nanowire arrays. *Adv. Funct. Mater.* **32**, 2206264 (2022).
24. Sun, S., Yuan, D., Xu, Y., Wang, A. & Deng, Z. Ligand-mediated synthesis of shape-controlled cesium lead halide perovskite nanocrystals via reprecipitation process at room temperature. *ACS Nano* **10**, 3648–3657 (2016).
25. Dey, A. et al. State of the art and prospects for halide perovskite nanocrystals. *ACS Nano* **15**, 10775–10981 (2021).
26. Hassan, Y. et al. Ligand-engineered bandgap stability in mixed-halide perovskite LEDs. *Nature* **591**, 72–77 (2021).
27. Sun, W. et al. Resurfacing mixed-halide perovskite nanocrystal for efficient and spectral stable pure-red light-emitting diodes. *Nano Energy* **136**, 110760 (2025).
28. Park, D. et al. Interactive deformable colored sound display achieved with electrostrictive fluoropolymer and halide perovskite. *Small* **20**, 2402281 (2024).
29. Bai, W. et al. Perovskite light-emitting diodes with an external quantum efficiency exceeding 30%. *Adv. Mater.* **35**, 2302283 (2023).
30. Saleem, M. I., Batool, A. & Hur, J. Advancing perovskite light-emitting diodes: multifunctional role of polymer, organic, and inorganic ligands in stability and efficiency enhancement. *Nano Energy* **142**, 111272 (2025).
31. He, J. et al. Hot-injection synthesis of cesium lead halide perovskite nanowires with tunable optical properties. *Materials* **17**, 2173 (2024).
32. Chen, G. et al. Stable α-$CsPbI_3$ perovskite nanowire arrays with preferential crystallographic orientation for highly sensitive photodetectors. *Adv. Funct. Mater.* **29**, 1808741 (2019).
33. Liu, Z. et al. Synthesis of lead-free Cs_2AgBiX_6 (X = Cl, Br, I) double perovskite nanoplatelets and their application in CO_2 photocatalytic reduction. *Nano Lett* **21**, 1620–1627 (2021).
34. Yang, Z., Liu, Y. & Chen, W. A brief review of perovskite quantum dot solar cells: synthesis, property and defect passivation. *Chemsuschem* **18**, e202401587 (2025).
35. Wen, J.-R., Champ, A., Bauer, G. & Sheldon, M. T. Chemical and structural stability of $CsPbX_3$ nanorods during postsynthetic anion-exchange: implications for optoelectronic functionality. *ACS Appl. Nano Mater* **7**, 3024–3031 (2024).
36. Hu, X. et al. Scalable synthesis of efficiently luminescent and color-tunable $CsPbX_3$ (X=Cl, Br, I) nanocrystals by regulating the reaction parameters. *J. Lumin.* **251**, 4859–4867 (2022).
37. Hills-Kimball, K., Yang, H., Cai, T., Wang, J. & Chen, O. Recent advances in ligand design and engineering in lead halide perovskite nanocrystals. *Adv. Sci.* **8**, 2100214 (2021).
38. Liu, H., Li, T. & Wang, Y. 2-Bromohexadecanoic acid as a novel bidentate ligand for passivation of cesium lead halide perovskite nanocrystals with near-unity photoluminescence quantum yield and superior photostability. *ACS Appl. Mater. Interfaces* **17**, 24146–24156 (2025).
39. Shi, E. et al. Two-dimensional halide perovskite lateral epitaxial heterostructures. *Nature* **580**, 614–620 (2020).
40. Ye, J. et al. Strongly-confined colloidal lead-halide perovskite quantum dots: from synthesis to applications. *Chem. Soc. Rev.* **53**, 8095–8122 (2024).
41. Chen, X. et al. Recent progress and challenges of bismuth-based halide perovskites for emerging optoelectronic applications. *Adv. Opt. Mater.* **11**, 2202153 (2023).
42. Zhang, L. et al. Advances in the application of perovskite materials. *Nano-Micro Lett* **15**, 177 (2023).
43. Wu, J. et al. Regioselective multisite atomic-chlorine passivation enables efficient and stable perovskite solar cells. *J. Am. Chem. Soc* **145**, 5872–5879 (2023).
44. Zhou, W. et al. Manipulating ionic behavior with bifunctional additives for efficient sky-blue perovskite light-emitting diodes. *Adv. Funct. Mater.* **33**, 2301425 (2023).
45. Lopez-Fernandez, I. et al. Lead-free halide perovskite materials and optoelectronic devices: progress and prospective. *Adv. Funct. Mater.* **34**, 2307896 (2024).
46. Dong, H. et al. Metal Halide Perovskite for next-generation optoelectronics: progresses and prospects. *Elight* **3**, 3 (2023).
47. Aftab, S., Koyyada, G., Assiri, M. A., Rubab, N. & Kim, J. H. Perovskite nanocrystals: Synthesis, stability, and technological applications. *J. Alloy. Compd.* **1024**, 180302 (2025).
48. Aftab, S. et al. Perovskite quantum dots: fabrication, degradation, and enhanced performance across solar cells, optoelectronics, and quantum technologies. *Carbon Energy*, e70018 (2025).
49. Du, Y.-J. et al. Integration of perovskite/low-dimensional material heterostructures for optoelectronics and artificial visual systems. *Adv. Funct. Mater.* **35**, 2500953 (2025).
50. Anthony, A. M., Pandian, M. K., Pandurangan, P. & Bhagavathiachari, M. Zero- and one-dimensional lead-free perovskites for photoelectrochemical applications. *ACS Appl. Mater. Interfaces* **14**, 29735–29743 (2022).
51. Li, M. & Xia, Z. Recent progress of zero-dimensional luminescent metal halides. *Chem. Soc. Rev.* **50**, 2626–2662 (2021).
52. Maczka, M., Drozdowski, D., Stefanska, D. & Gagor, A. Zero-dimensional mixed-cation hybrid lead halides with broadband emissions. *Inorg. Chem. Front.* **10**, 7222–7230 (2023).
53. Sun, S. et al. 0D perovskites: unique properties, synthesis, and their applications. *Adv. Sci.* **8**, 2102689 (2021).
54. Yang, H., Cai, T., Dube, L. & Chen, O. Synthesis of double perovskite and quadruple perovskite nanocrystals through post-synthetic transformation reactions. *Chem. Sci.* **13**, 4874–4883 (2022).
55. Zhang, Y., Zhao, Z., Liu, Z. & Tang, A. The scale effects of organometal halide perovskites. *Nanomaterials* **13**, 2935 (2023).
56. Hu, H. et al. Enhanced photostability of lead halide perovskite nanocrystals with Mn^{3+} incorporation. *ACS Appl. Mater. Interfaces* **16**, 17946–17953 (2024).
57. Lyu, B. et al. Side-chain-promoted polymer architecture enabling stable mixed-halide perovskite light-emitting diodes. *ACS Energy Lett* **9**, 2118–2127 (2024).
58. Dai, S.-W. et al. Organic lead halide nanocrystals providing an ultra-wide color gamut with almost-unity photoluminescence quantum yield. *ACS Appl. Mater. Interfaces* **13**, 25202–25213 (2021).
59. Wani, T. A. A., Shamsi, J., Bai, X., Arora, N. & Dar, M. I. Advances in all-inorganic perovskite nanocrystal-based white light emitting devices. *ACS Omega* **8**, 17337–17349 (2023).
60. Hong, D. et al. Unveiling non-radiative center control in $CsPbBr_3$ nanocrystals: a comprehensive comparative analysis of hot injection and ligand-assisted reprecipitation approaches. *Nano Res* **17**, 4525–4534 (2024).
61. Wang, X., Liu, W., He, J., Li, Y. & Liu, Y. Synthesis of all-inorganic halide perovskite nanocrystals for potential photoelectric catalysis applications. *Catalysts* **13**, 1041 (2023).
62. Wang, X. et al. In situ siloxane passivation of colloidal lead halide perovskite via hot injection for light-emitting diodes. *Opt. Lett.* **47**, 593–596 (2022).
63. Wu, J. et al. Ultra-small cesium silver bismuth bromide quantum dots fabricated by modified hot-injection method for highly efficient degradation of contaminants in organic solvent. *J. Environ. Sci.* **152**, 577–583 (2025).
64. Leng, J. et al. Tuning the emission wavelength of lead halide perovskite NCs via size and shape control. *ACS Omega* **7**, 565–577 (2022).
65. Gao, F. et al. Deep-blue emissive $Cs_3Cu_2I_5$ perovskites nanocrystals with 96.6% quantum yield via InI3-assisted synthesis for light-emitting device and fluorescent ink applications. *Nano Energy* **98**, 107270 (2022).
66. Vighnesh, K., Wang, S., Liu, H. & Rogach, A. L. Hot-injection synthesis protocol for green-emitting cesium lead bromide perovskite nanocrystals. *ACS Nano* **16**, 19618–19625 (2022).

67. Fellner, M. & Lauria, A. Caesium manganese fluoride cubic-perovskite nanoparticles-synthesis, luminescence and magnetic properties. *J. Sol.-Gel Sci. Technol.* **107**, 259–268 (2023).
68. Chu, J. et al. One-pot and large-scale production of uniform ytterbium-doped perovskite nanocrystals with controllable optical properties. *J. Mater. Chem. C* **12**, 17647–17657 (2024).
69. Yu, Q., Zhang, P., Hao, S., Zhu, C. & Yang, C. Investigation of bandgap and optical properties of Ag^{+}/Al^{3+} co-alloyed lead-free double perovskite $Cs_2NaBiCl_6$. *Opt. Mater.* **160**, 116768 (2025).
70. Low, Y. J. et al. Synthesis of cesium silver bismuth bromide double perovskite nanoparticles via a microwave-assisted solvothermal method. *Mater. Today Chem.* **29**, 101477 (2023).
71. Zhang, Y. et al. Highly stable metal halides Cs_2ZnX_4 (X = Cl, Br) with Sn^{2+} as dopants for efficient deep-red photoluminescence. *Chin. Chem. Lett.* **34**, 107556 (2023).
72. Kou, T. et al. Heterovalent ion doped 0D Cs_3CdBr_5 with near-unity photoluminescence yield and multifunctional applications. *J. Mater. Sci. Technol* **225**, 87–94 (2025).
73. Li, H. et al. Core-shell structured$CsPbBr_3$/Sn-TiO_2 nanocrystals for visible-light-driven photocatalyst in aqueous solution. *Appl. Surf. Sci.* **599**, 153937 (2022).
74. Ye, S., Huang, M., Han, Q., Song, J. & Qu, J. Significantly enhanced thermal and water stability of heterostructured $CsPbBr_3$/Cs_4PbBr_6@PbS nanocrystals. *J. Alloy. Compd.* **965**, 171442 (2023).
75. Ng, C. K., Yin, W., Li, H. & Jasieniak, J. J. Scalable synthesis of colloidal $CsPbBr_3$ perovskite nanocrystals with high reaction yields through solvent and ligand engineering. *Nanoscale* **12**, 4859–4867 (2020).
76. Sanchez, S. L., Tang, Y., Hu, B., Yang, J. & Ahmadi, M. Understanding the ligand-assisted reprecipitation of $CsPbBr_3$ nanocrystals via high-throughput robotic synthesis approach. *Matter* **6**, 2900–2918 (2023).
77. Shankar, H., Bansal, P., Yu, W. W. & Kar, P. Aqueous precursor induced morphological change and improved water stability of $CsPbBr_3$ nanocrystals. *Chem. Eur. J* **26**, 12242–12248 (2020).
78. Treber, F., Frank, K., Nickel, B., Lampe, C. & Urban, A. S. Lead-free, luminescent perovskite nanocrystals obtained through ambient condition synthesis. *Small* **19**, 2300525 (2023).
79. Wang, S. et al. Room-temperature synthesis of lead-free copper(I)-antimony(III)-based double perovskite nanocrystals. *Apl. Mater.* **11**, 041110 (2023).
80. Makwana, K. P., Malek, N. I. & Kailasa, S. K. Colloidal perovskite nanomaterials: new insights on synthetic routes, properties and sensing applications. *Adv. Colloid Interface Sci* **344**, 103587–103587 (2025).
81. Li, Y., Cai, M., Shen, M., Cai, Y. & Xie, R.-J. Bidentate aliphatic quaternary ammonium ligand-stabilized $CsPbBr_3$ perovskite nanocrystals with high PLQY (92.3%) and superior stability. *J. Mater. Chem. C.* **10**, 8356–8363 (2022).
82. Kar, M. R. et al. Impact of Zn-doping on the composition, stability, luminescence properties of silica coated all-inorganic cesium lead bromide nanocrystals and their biocompatibility. *Mater. Today Chem.* **23**, 100753 (2022).
83. Chen, Z. & Dhakal, T. P. P. Room temperature synthesis of lead-free $FASnI_3$ perovskite nanocrystals with improved stability by SnF_2 additive. *Appl. Phys. Rev.* **10**, 011404 (2023).
84. Shen, W. et al. Ligand-assisted breaking crystal symmetry to achieve stable γ-$CsPbI_3$ nanorods with strong polarization response. *ACS Energy Lett* **8**, 2561–2569 (2023).
85. Wang, Y. et al. Cesium lead iodide perovskites: optically active crystal phase stability to surface engineering. *Micromachines* **13**, 1318 (2022).
86. Chen, X. et al. Phase regulation and surface passivation of stable α-$CsPbI_3$ nanocrystals with dual-mode luminescence via synergistic effects of ligands. *J. Phys. Chem. C* **126**, 5233–5243 (2022).
87. Bai, F. et al. Synthesis and application of lead iodine-based perovskite nanomaterials. *Chem. Phys. Lett.* **860**, 141776 (2025).
88. Lai, H. M. et al. Direct room temperature synthesis of α-$CsPbI_3$ perovskite nanocrystals with high photoluminescence quantum yields: implications for lighting and photovoltaic applications. *Acs Appl. Nano Mater* **5**, 12366–12373 (2022).
89. Uddin, M. A. et al. Multifunctional thiol-containing additives for improved photoluminescence and photovoltaic performance of $Cs_{0.15}FA_{0.85}PbI_3$ perovskites. *ACS Appl. Electron. Mater* **4**, 903–909 (2022).
90. Ghorai, A. et al. Ligand-mediated revival of degraded α-$CsPbI_3$ to stable highly luminescent perovskite. *Angew. Chem.-Int. Ed.* **62**, e202302852 (2023).
91. Lee, S. Y. et al. Investigation of highly luminescent inorganic perovskite nanocrystals synthesized using optimized ultrasonication method. *Ultrason. Sonochem.* **89**, 106145 (2022).
92. Ning, F., Wang, X. & Wang, Y. Unraveling the ultrasonic-assisted synthesis of green-emitting $CsPbBr_3$@Cs_4PbBr_6: reaction process, luminescence property, and display application. *Inorg. Chem.* **63**, 20993–20999 (2024).
93. Wang, C. et al. Exceptional stability against water, UV light, and heat for $CsPbBr_3$@Pb-MOF composites. *Small Methods* **8**, 2400241 (2024).
94. Jiang, H. et al. One-step preparation of ion-doped cesium lead halide perovskite nanocrystals by ultrasonication. *Part. Syst. Charact* **40**, 2300032 (2023).
95. Dou, Y. et al. Ten-gram-scale synthesis of $FAPbX_3$ perovskite nanocrystals by a high-power room-temperature ultrasonic-assisted strategy and their electroluminescence. *Adv. Mater. Technol.* **5**, 1901089 (2020).
96. Abdel-Latif, K., Bateni, F., Crouse, S. & Abolhasani, M. Flow synthesis of metal halide perovskite quantum dots: from rapid parameter space mapping to AI-guided modular manufacturing. *Matter* **3**, 1053–1086 (2020).
97. Sadeghi, S. et al. A self-driving fluidic lab for data-driven synthesis of lead-free perovskite nanocrystals. *Digital Discov* **4**, 1722–1733 (2025).
98. Abdel-Latif, K. et al. Facile room-temperature anion exchange reactions of inorganic perovskite quantum dots enabled by a modular microfluidic platform. *Adv. Funct. Mater.* **29**, 1900712 (2019).
99. Jha, P. et al. Photo-induced bandgap engineering of metal halide perovskite quantum dots in flow. *Adv. Mater.* **37**, 2419668 (2025).
100. Li, M. et al. Ultrasonic cavitation-enabled microfluidic approach toward the continuous synthesis of cesium lead halide perovskite nanocrystals. *Chin. J. Chem. Eng.* **59**, 32–41 (2023).
101. Fang, X. et al. Light-induced synthesis of Highly stable $CsPbCl_3$:Mn^{2+}@$mSiO_2$ nanocomposites for white Light-Emitting Diodes. *Chem. Eng. J.* **500**, 157339 (2024).
102. Li, H. et al. Thermal management towards ultra-bright and stable perovskite nanocrystal-based pure red light-emitting diodes. *Nat. Commun.* **15**, 6561 (2024).
103. Wei, K. et al. Perovskite heteroepitaxy for high-efficiency and stable pure-red LEDs. *Nature* **638**, 949–956 (2025).
104. Lv, H., Tang, X. & Chen, M. Ionic doping of $CsPbI_3$ perovskite nanocrystals improves luminescence and stability in patterned large-area light-emitting diodes. *ACS Appl. Nano Mater* **6**, 18918–18925 (2023).
105. Saleem, M. I., He, S., Kim, S. H., Kang, J.-W. & Lee, J.-H. Perovskite nanocrystals passivated by aromatic phosphonic acid for high-performance light-emitting diodes. *J. Mater. Chem. C* **12**, 17289–17297 (2024).
106. Han, Y. et al. Manipulating electron-phonon coupling for efficient tin halide perovskite blue LEDs. *Adv. Mater.* **37**, 2413895 (2025).

107. Wang, Q., Zhang, X., Qian, L. & Xiang, C. Improving perovskite green quantum dot light-emitting diode performance by hole interface buffer layers. *ACS Appl. Mater. Interfaces* **15**, 28833–28839 (2023).
108. Chen, F. et al. Highly spectra-stable pure blue perovskite light-emitting diodes based on copper and potassium co-doped quantum dots. *Nano Res* **16**, 7654–7660 (2023).
109. Chen, T. et al. Tetrafluoroborate-passivated $CsPbB_xCl_{3-x}$ nanocrystals for spectrally stable pure blue perovskite light-emitting diodes. *ACS Appl. Nano Mater* **7**, 4474–4480 (2024).
110. Baek, S.-D., Wang, C., Khang, D.-Y. & Myoung, J.-M. Mixed halide perovskite nanocrystals with surface engineering based on pseudohalide passivation and Short-Chain ligand exchange for High-Performance blue Light-Emitting diodes. *Chem. Eng. J.* **455**, 140594 (2023).
111. Zhou, X. et al. Synchronously polishing the lead-rich surface and passivating surface defects of $CsPb(Br/I)_3$ quantum dots for high-performance pure-red PeLEDs. *Nano Lett* **24**, 3719–3726 (2024).
112. Xie, M. et al. Suppressing ion migration of mixed-halide perovskite quantum dots for high efficiency pure-red light-emitting diodes. *Adv. Funct. Mater.* **33**, 2300116 (2023).
113. Fan, M. et al. Efficient all-perovskite white light-emitting diodes made of in situ grown perovskite-mesoporous silica nanocomposites. *Adv. Funct. Mater.* **33**, 2215032 (2023).
114. Fang, T. et al. Sulfonate additive simultaneously suppresses interstitials and vacancies toward efficient and stable perovskite quantum dot LEDs. *Adv. Opt. Mater.* **12**, 2302253 (2024).
115. Karmaker, H., Siddique, A., Das, B. K. & Islam, M. N. Modeling and performance investigation of novel inorganic $Cs_4CuSb_2Cl_{12}$ nanocrystal perovskite solar cell using SCAPS-1D. *Results Eng* **22**, 102106 (2024).
116. Yang, W. et al. Overcoming charge confinement in perovskite nanocrystal solar cells. *Adv. Mater.* **35**, 2304533 (2023).
117. Liu, Y. et al. Hexagonal lead-free Cs_2AgBiI_6 perovskite nanocrystals: a promising material for solar cell application. *ACS Appl. Energy Mater* **6**, 5188–5196 (2023).
118. Song, H. et al. On the surface passivating principle of functional thiol towards efficient and stable perovskite nanocrystal solar cells. *Chem. Eng. J.* **454**, 140224 (2023).
119. Wang, B. et al. Ruddlesden-popper perovskite nanocrystals as interface modification layer for efficient perovskite solar cells. *Nano Lett* **24**, 4512–4520 (2024).
120. Fu, J. et al. 3D/2D core/shell perovskite nanocrystals for high-performance solar cells. *Small* **19**, 2207312 (2023).
121. Wieliczka, B. M., Habisreutinger, S. N., Schutt, K., Blackburn, J. L. & Luther, J. M. Nanocrystal-enabled perovskite heterojunctions in photovoltaic applications and beyond. *Adv. Energy Mater.* **13**, 2204351 (2023).
122. Goldreich, A., Prilusky, J., Prasad, N., Puravankara, A. & Yadgarov, L. Highly stable $CsPbBr_3$@MoS_2 nanostructures: synthesis and optoelectronic properties toward implementation into solar cells. *Small* **20**, 2404727 (2024).
123. Guan, X. et al. Perovskite quantum dots embedded paper photodetectors with high flexibility and self-powered operation. *J. Mater. Chem. C* **12**, 5784–5792 (2024).
124. Suhail, A., Saini, A., Beniwal, S. & Bag, M. Tunable optoelectronic properties of $CsPbBr_3$ perovskite nanocrystals for photodetectors applications. *J. Phys. Chem. C.* **127**, 17298–17306 (2023).
125. Patra, D., Saini, A., Bag, M. & Singh, S. P. Amine-free $CsPbBr_3$ perovskite nanocrystals with a near-unity photoluminescence quantum yield for a superfast photodetector. *ACS Appl. Nano Mater* **7**, 16438–16449 (2024).
126. Sulaman, M. et al. Hybrid bulk-heterojunction of colloidal quantum dots and mixed-halide perovskite nanocrystals for high-performance self-powered broadband photodetectors. *Adv. Funct. Mater.* **32**, 2201527 (2022).
127. Jeong, S.-J. et al. Zero dimensional-two dimensional hybrid photodetectors using multilayer MoS_2 and lead halide perovskite quantum dots with a tunable bandgap. *ACS Appl. Mater. Interfaces* **15**, 5432–5438 (2023).
128. Yang, B. et al. Self-powered photodetectors based on $CsPbBr_3$ quantum dots/organic semiconductors/SnO_2 heterojunction for weak light detection. *Sci. China-Mater.* **66**, 716–723 (2023).
129. Wei, H. et al. High-performance $CsPbI_3$ quantum dot photodetector with a vertical structure based on the frenkel-poole emission effect. *ACS Nano* **18**, 26643–26654 (2024).
130. Moon, B., Ahn, J.-H., Jeong, M.-H., Lee, S.-H. & Lee, J.-S. High-performance and stability of $CsPbBr_3$/WSe_2 hybrid photodetectors functionalized using quaternary ammonium ligands. *Adv. Opt. Mater.* **11**, 2300414 (2023).
131. Saleem, M. I., Sulaman, M., Batool, A., Bukhtiar, A. & Khalid, S. Suppression of mid-gap trap state in $CsPbBr_3$ nanocrystals with Br-passivation for self-powered photodetector. *Energy Technol* **11**, 2300013 (2023).
132. Athanasiou, M. et al. Efficient amplified spontaneous emission from solution-processed $CsPbBr_3$ nanocrystal microcavities under continuous wave excitation. *ACS Photonics* **8**, 2120–2129 (2021).
133. He, Y. et al. Lasing properties and carrier dynamics of $CsPbBr_3$ perovskite nanocrystal vertical-cavity surface-emitting laser. *Nanophotonics* **12**, 2133–2143 (2023).
134. Lu, Y.-J. et al. Upconversion plasmonic lasing from an organolead trihalide perovskite nanocrystal with low threshold. *ACS Photonics* **8**, 335–342 (2021).
135. Xie, M. et al. Solution-processed whispering-gallery-mode microsphere lasers based on colloidal $CsPbBr_3$ perovskite nanocrystals. *Nanotechnology* **33**, 115204 (2022).
136. Wei, Y. et al. Turn-on fluorescence humidity sensing based on Cs_4PbBr_6 nanocrystal array. *J. Mater. Chem. C.* **12**, 4054–4061 (2024).
137. Xu, X. et al. $CsPbBr_3$-based nanostructures for room-temperature sensing of volatile organic compounds. *ACS Appl. Mater. Interfaces* **14**, 39524–39534 (2022).
138. Li, H. et al. Photoluminescence sensing of chloride ions in sea sand using alcohol-dispersed $CsPbBr_3$@SiO_2 perovskite nanocrystal composites. *Chemosensors* **10**, 170 (2022).
139. Liu, Y., Guo, H., Mei, A., Chen, K. & Chen, W. Bromine-defect induced high sensitivity of Cs_4PbBr_6 nanocrystals humidity sensor. *J. Alloy. Compd.* **1005**, 176043 (2024).
140. Wu, Y. et al. Temperature sensing of novel Tb^{3+}/Ho^{3+}/Bi^{3+} co-doped lead-free double perovskite $Cs_2AgInCl_6$ nanocrystals. *J. Lumin.* **268**, 120430 (2024).
141. Guha, S. et al. Deriving chiroptical properties from intrinsically achiral building blocks of one-dimensional $CsPbBr_3$ perovskite nanowires. *J. Am. Chem. Soc.* **146**, 33883–33892 (2024).
142. Zhou, C. et al. Low dimensional metal halide perovskites and hybrids. *Mater. Sci. Eng. R.Rep.* **137**, 38–65 (2019).
143. Huang, M. et al. Heterogeneous interface engineering enabling homogeneous metal halide perovskite nanowires for artificial synapses. *Mater. Today Nano* **25**, 100449 (2024).
144. Zhang, Q. et al. Perovskite light-emitting diodes with quantum wires and nanorods. *Adv. Mater.* **37**, 2405418 (2025).
145. Huang, Z., Zhang, Z., Lamers, N., Baranov, D. & Wallentin, J. Controlled ligand-free growth of free-standing $CsPbBr_3$ perovskite nanowires. *ACS Omega* **9**, 48390–48396 (2024).
146. Li, Y. S., Liang, S., Trieu, T., Bautista, R. R. & Lin, Z. Unraveling the electronic heterogeneity and inhomogeneity in individual perovskite $CsPbBr_3$ nanowires. *Acs Appl. Energy Mater* **5**, 4431–4438 (2022).
147. Lin, C.-K. et al. Controlling the phase transition in $CsPbI_3$ nanowires. *Nano Lett* **22**, 2437–2443 (2022).
148. Markina, D. I. et al. Photophysical properties of halide perovskite $CsPb(Br_{1-x}I_x)_3$ thin films and nanowires. *J. Lumin.* **220**, 116985 (2020).

149. Pushkarev, A. P. et al. Nanoimprinted halide perovskite nanowires with directly-written gratings. *Photonics Nanostruct.-Fundament. Appl.* **53**, 101103 (2023).
150. Ren, K. et al. Electrodeposition-grown mixed-halide inorganic perovskite $CsPbI_{3-x}Br_x$ nanowires for nanolaser applications. *Small* **20**, 2406681 (2024).
151. Saleem, M. I. & Lee, J.-H. Colloidal cesium lead bromide-based anisotropic nanorods for improving outcoupling in perovskite light-emitting diodes. *J. Inf. Disp* **25**, 157–168 (2024).
152. Wang, W. et al. Sustainable fabrication of ultralong Pb(OH)Br nanowires and their conversion to luminescent $CH_3NH_3PbBr_3$ nanowires. *Green. Chem.* **23**, 7956–7962 (2021).
153. Wang, Y., Jiang, P., Liang, K. & Yu, L. On-chip unidirectional micro-nano-light sources based on multi-mode cesium lead halide perovskite nanowires. *Appl. Phys. Lett.* **119**, 173101 (2021).
154. Oksenberg, E. et al. Large lattice distortions and size-dependent bandgap modulation in epitaxial halide perovskite nanowires. *Nat. Commun.* **11**, 489 (2020).
155. Lv, Q. et al. Laser-induced phase segregation of inorganic halide perovskite alloy nanowires for optical switch. *Nano Res* **18**, 94907119 (2025).
156. Zhang, H. et al. Lasing operation in the $CsPbBr_3$ perovskite micron hemisphere cavity grown by chemical vapor deposition. *Chem. Eng. J.* **389**, 124395 (2020).
157. Meng, Y. et al. Direct vapor–liquid–solid synthesis of all-inorganic perovskite nanowires for high-performance electronics and optoelectronics. *ACS Nano* **13**, 6060–6070 (2019).
158. Meng, Y. et al. Perovskite core–shell nanowire transistors: interfacial transfer doping and surface passivation. *ACS Nano* **14**, 12749–12760 (2020).
159. Hossain, M. K. et al. Mechanism of non-catalytic chemical vapor deposition growth of all-inorganic $CsPbX_3$ (X = Br, Cl) nanowires. *J. Mater. Chem. C.* **9**, 3229–3238 (2021).
160. Li, D. et al. Surface energy-mediated self-catalyzed CsPbBr3 nanowires for phototransistors. *Adv. Electron. Mater.* **8**, 2200727 (2022).
161. Yadav, P. et al. Morphology-controlled vapor-phase nanowire growth with Ruddlesden-Popper lead bromide perovskite. *Chem. Mater.* **35**, 3300–3306 (2023).
162. Bai, Y. et al. In situ cell-scale probing nucleation, growth and evolution of $CsPbBr_3$ nanowires by optical absorption spectroscopy. *Nanotechnology* **35**, 305701 (2024).
163. Chen, M. et al. Exciton-to-dopant energy transfer dynamics in Mn^{2+} Doped $CsPbBr_3$ nanowires synthesized by diffusion doping. *J. Phys. Chem. Lett.* **14**, 11543–11549 (2023).
164. Li, H. et al. Evolution and mechanism of cesium lead bromide nanostructures in oleylamine-rich system by hot-injection method. *Adv. Mater. Interfaces* **10**, 2201916 (2023).
165. Gokul, M. A. & Rahman, A. Phase evolution of all-inorganic perovskite nanowires during its growth from quantum dots. *Nanotechnology* **33**, 085706 (2022).
166. Jia, F.-Y. et al. Improvement in the stability of γ-$CsPbI_3$ nanowires enabled by lattice immobilization through the Pb-O anchor in SBA-15. *Inorg. Chem. Front.* **7**, 4572–4579 (2020).
167. Fu, Y. et al. Strongly quantum-confined perovskite nanowire arrays for color-tunable blue-light-emitting diodes. *ACS Nano* **16**, 8388–8398 (2022).
168. Zhang, Z. et al. Single-crystalline perovskite nanowire arrays for stable x-ray scintillators with micrometer spatial resolution. *ACS Appl. Nano Mater* **5**, 881–889 (2022).
169. Zhang, Z. et al. Free-standing metal halide perovskite nanowire arrays with blue-green heterostructures. *Nano Lett* **22**, 2941–2947 (2022).
170. Lin, C.-H. et al. Designed growth and patterning of perovskite nanowires for lasing and wide color gamut phosphors with long-term stability. *Nano Energy* **73**, 104801 (2020).
171. Chu, K. et al. Dimension-programmable $CsPbBr_3$ nanowires for plasmonic lasing with PDMS templated technique. *J. Phys. D. Appl. Phys* **55**, 215104 (2022).
172. Song, Z., Zhu, M., Chen, S., Xu, M. & Jie, W. Templated synthesis of $CsPbBr_3$ nanowire arrays toward low dark current drift and stable X-ray detectors. *J. Mater. Chem. C.* **12**, 9247–9254 (2024).
173. Paul, S., Ariga, K., Sarma, D. D. & Acharya, S. Dimension-controlled halide perovkites using templates. *Nano Today* **39**, 101181 (2021).
174. Chen, L. et al. SolvenT-mediated Structural Evolution In Colloidal Lead Halide Perovskite Nanocrystals Self-assembly. *Adv. Mater. Interfaces* **9**, 2200187 (2022).
175. Xu, G. et al. In-plane self-assembly and lasing performance of cesium lead halide perovskite nanowires. *Mater. Res. Lett.* **7**, 203–209 (2019).
176. Zardari, P. & Rostami, A. Construction of 1D perovskite nanowires by Urotropin passivation towards efficient and stable perovskite solar cell. *Sol. Energy Mater. Sol. Cells* **227**, 111119 (2021).
177. Pan, J. et al. Halogen vacancies enable ligand-assisted self-assembly of perovskite quantum dots into nanowires. *Angew. Chem.-Int. Ed.* **58**, 16077–16081 (2019).
178. Zhang, J. et al. A high-performance photodetector based on 1D perovskite radial heterostructure. *Adv. Opt. Mater.* **9**, 2101504 (2021).
179. Peng, Z. et al. Self-assembled ultrafine $CsPbB_3$ perovskite nanowires for polarized light detection. *Sci. China-Mater.* **64**, 2261–2271 (2021).
180. Ghorai, A., Das, A., Choi, Y., Roy, B. & Jeong, U. Revival of degraded CsPbI3 nanocrystals by diselenide ligand and nanocrystal self-assembly on nanofibrilar ligand template. *Small* **20**, 2404384 (2024).
181. Wu, W. et al. Green-white color switchable light-emitting devices based on laterally fused cesium lead bromide perovskite nanowires. *Appl. Phys. Lett.* **119**, 033505 (2021).
182. Jiang, S. et al. In-plane integrating unidirectional 1D $CsPbBr_3$ waveguide arrays with heterogeneous semiconductor wires for photonic integrated circuits. Adv. *Optical Mater* **11**, 2300596 (2023).
183. Xu, X. et al. Tunable fabrication of MAPbX3Triangular-micro-wires array for constructing high sensitivity photodetector. *Adv. Mater. Technol.* **8**, 2300946 (2023).
184. Chen, Y. et al. Amplifying surface energy difference toward anisotropic growth of all-inorganic perovskite single-crystal wires for highly sensitive photodetector. *Adv. Funct. Mater.* **31**, 2101966 (2021).
185. Chen, G. et al. Air-stable highly crystalline formamidinium perovskite 1D structures for ultrasensitive photodetectors. *Adv. Funct. Mater.* **30**, 1908894 (2020).
186. Guo, H. et al. Embedding laser generated GaAs nanocrystals in perovskite wires for enhanced charge transport and photodetection. *Sci. China Phys. Mech. Astron.* **65**, 274204 (2022).
187. Wei, Y. et al. A high-responsivity $CsPbBr_3$ nanowire photodetector induced by $CdS@Cd_xZn_{1-x}S$ gradient-alloyed quantum dots. *Nanoscale Horiz* **7**, 644–654 (2022).
188. Zhang, D. et al. Vertical heterogeneous integration of metal halide perovskite quantum-wires/nanowires for flexible narrowband photodetectors. *Nano Lett* **22**, 3062–3070 (2022).
189. Wang, H. et al. Spraying perovskite intermediate enabling inch-scale microwire film fabrication for integration compatible efficient-photodetectors array. *Adv. Funct. Mater.* **33**, 2209942 (2023).
190. Salimian, S. & Anttu, N. Optimized absorption of light in perovskite nanowire solar cells. *Nanotechnology* **35**, 175206 (2024).
191. Luo, T., Liu, L., Du, M., Wang, K. & Liu, S. Vacuum preparation of charge transport layers for perovskite solar cells and modules. *J. Mater. Chem. A* **13**, 1669–1710 (2025).
192. Swain, B. S., Rahim, A., Singh, S. & Lee, J. Microstructures, structural, optical, and photovoltaic characteristics of mixed halide perovskite nanowires. *Appl. Phys. a-Mater. Sci. Process* **127**, 674 (2021).

193. Shin, Y. M. et al. Dual-phase stabilized perovskite nanowires for reduced defects and longer carrier lifetime. *Adv. Funct. Mater.* **33**, 2210155 (2023).
194. Cha, J. et al. Perovskite nanowires as defect passivators and charge transport networks for efficient and stable perovskite solar cells. *Chem. Eng. J.* **451**, 138920 (2023).
195. Yang, E. et al. Controllable synthesis and heterogeneous tailoring of 1D perovskites, emerging properties and applications. *Adv. Powder Mater* **4**, 100250 (2025).
196. Wang, Q. et al. Superfluorescence and nonlinear optical response of $CH_3NH_3PbBr_3$-based mesostructures: applications to amplified spontaneous emission and ultrafast lasers. *Opt. Express* **33**, 1625–1635 (2025).
197. Tang, B. et al. Energy transfer and wavelength tunable lasing of single perovskite alloy nanowire. *Nano Energy* **71**, 104641 (2020).
198. Sun, M. et al. Two photon pumped nanowire laser based on all inorganic perovskite with high exciton binding energy grown by physical vapor deposition. *J. Phys. D. Appl. Phys.* **54**, 275103 (2021).
199. Guo, P. et al. On-wire axial perovskite heterostructures for monolithic dual-wavelength laser. *Nano Energy* **92**, 106778 (2022).
200. Zhao, J. et al. Ultra-thin size-controllable surface plasmon polariton laser by PDMS-assisted imprinting. *J. Phys. D.-Appl. Phys.* **57**, 405102 (2024).
201. Zhang, D. et al. Large-scale planar and spherical light-emitting diodes based on arrays of perovskite quantum wires. *Nat. Photonics* **16**, 284–290 (2022).
202. Cevallos-Toledo, R. B. et al. Ruddlesden-Popper hybrid lead bromide perovskite nanosheets of phase pure n=2: stabilized colloids stored in the solid state. *Angew. Chem.-Int. Ed* **60**, 27312–27317 (2021).
203. Litvin, A. P. et al. B-site doping of metal halide perovskite nanoplatelets influences their optical properties. *Adv. Opt. Mater.* **12**, 2301001 (2024).
204. Gao, Y. et al. Copper-doping defect-lowered perovskite nanosheets for deep-blue light-emitting diodes. *J. Colloid Interface Sci* **607**, 1796–1804 (2022).
205. Huang, J., Zou, S., Lin, J., Liu, Z. & Qi, M. Ultrathin lead-free double perovskite cesium silver bismuth bromide nanosheets. *Nano Res* **14**, 4079–4086 (2021).
206. Jing, X. et al. Evolution of self-trapped exciton emission tuned by high pressure in 2D all-inorganic cesium lead halide nanosheets. *J. Mater. Chem. C* **10**, 8711–8718 (2022).
207. Mitrofanov, A. et al. Surface-assisted synthesis of perovskite nanosheets with bivalent aromatic cations. *J. Mater. Chem. C* **12**, 1440–1445 (2024).
208. Zhang, X., Zhao, S., Zhang, J. & Wang, L. Materials design and preparation of ultrathin two-dimensional metal halide perovskites. *Nano Res* **17**, 6231–6246 (2024).
209. Kostopoulou, A., Konidakis, I. & Stratakis, E. Two-dimensional metal halide perovskites and their heterostructures: from synthesis to applications. *Nanophotonics* **12**, 1643–1710 (2023).
210. Li, D. et al. Efficient photosensitized singlet oxygen generation in two-dimensional perovskite nanosheets via energy transfer. *Appl. Surf. Sci.* **613**, 155991 (2023).
211. Ji, Y. et al. In-depth understanding of the effect of halogen-induced stable 2d bismuth-based perovskites for photocatalytic hydrogen evolution activity. *Adv. Funct. Mater.* **32**, 2201721 (2022).
212. Aamir, M., Sher, M. & Akhtar, J. Synthesis of lead free hybrid copper halide perovskite nanosheets: structural and optical properties. *Results Opt* **13**, 100562 (2023).
213. Chen, Z. et al. Ultrahigh energy harvesting ability of PVDF incorporated with 2D halide perovskite nanosheets via interface effect. *Chem. Eng. J.* **497**, 4079–4086 (2024).
214. Li, S. et al. Sizeable square $CsPb_2Br_5$ nanosheets for photodetection. *Chem. Commun.* **60**, 4679–4682 (2024).
215. Malani, S. B., Klein, E., Lesyuk, R. & Klinke, C. Toward high-performance photodetectors based on quasi-2D ruddlesden-popper mixed-n perovskite nanomaterials. *Adv. Funct. Mater.* 2416027 (2024).
216. Wang, Y. et al. The controllable fabrication of $CsPbBr_3$ perovskite nanomaterials in various dimensions and their photophysical luminescent properties. *Opt. Mater.* **149**, 115096 (2024).
217. Ruan, L. et al. Ultra-stable Mn-doped perovskite-related tetragonal $CsPb_2Cl_5$ nanosheets with bright luminescence and strong antiferromagnetism. *Appl. Surf. Sci.* **685**, 154558 (2025).
218. Elattar, A. et al. Single crystal of two-dimensional mixed-halide copper-based perovskites with reversible thermochromism. *J. Mater. Chem. C* **9**, 3264–3270 (2021).
219. Wang, X.-D. et al. The top-down synthesis of single-layered $Cs_4CuSb_2Cl_{12}$ halide perovskite nanocrystals for photoelectrochemical application. *Nanoscale* **11**, 5180–5187 (2019).
220. Li, J. et al. Fabrication of single phase 2D homologous perovskite microplates by mechanical exfoliation. *2D Mater* **5**, 021001 (2018).
221. Dhanabalan, B. et al. Simple fabrication of layered halide perovskite platelets and enhanced photoluminescence from mechanically exfoliated flakes. *Nanoscale* **11**, 8334–8342 (2019).
222. He, Y. et al. Broadband nonlinear optical modulator with 2d organic-inorganic hybrid perovskite nanocrystals. *IEEE J. Sel. Top. Quantum Electron.* **29**, 5101108 (2023).
223. Uddin, M. A., Glover, J. D., Park, S. M., Pham, J. T. & Graham, K. R. Growth of highly stable and luminescent $CsPbX_3$ (X = Cl, Br, and I) nanoplates via ligand mediated anion exchange of $CsPbCl_3$ nanocubes with AlX_3. *Chem. Mater.* **32**, 5217–5225 (2020).
224. Shao, Y. et al. Unlocking surface octahedral tilt in two-dimensional Ruddlesden-Popper perovskites. *Nat. Commun.* **13**, 138 (2022).
225. Hintermayr, V. A. et al. Tuning the optical properties of perovskite nanoplatelets through composition and thickness by ligand-assisted exfoliation. *Adv. Mater.* **28**, 9478–9485 (2016).
226. Xie, M. et al. Aqueous phase exfoliating quasi-2D $CsPbBr_3$ nanosheets with ultrahigh intrinsic water stability. *Small* **15**, 1901994 (2019).
227. Ashokan, G., Subramani, S., Vellingiri, G., Nallathambi, A. & Kulandaivel, J. Layered $Cs_3Bi_2I_9$ perovskite nanosheets on TiO_2 nanorods for high-performance heterostructure photodetectors. *J. Mater. Chem. C* **13**, 2978–2986 (2025).
228. Zhong, J. et al. Thickness dependent properties of ultrathin perovskite nanosheets with Ruddlesden-Popper-like atomic stackings. *Nanoscale* **13**, 18961–18966 (2021).
229. He, Y., Ma, Y., Li, X. & Zhang, Y. All-inorganic perovskite nanosheet fabrication under synergistic effect for integrated optoelectronics with strong light-matter interactions. *ACS Appl. Nano Mater* **4**, 2634–2641 (2021).
230. Liu, D. et al. Giant nonlinear optical response of lead-free all-inorganic $CsSnBr_3$ nanoplates. *J. Phys. Chem. C.* **125**, 803–811 (2021).
231. Shi, X. et al. Vapor phase growth of air-stable hybrid perovskite $FAPbBr_3$ single-crystalline nanosheets. *Nano Lett* **24**, 2299–2307 (2024).
232. Yin, Y. et al. Space-confined chemical vapor deposition synthesis of all-inorganic $CsSnI_3$ perovskite nanosheets. *J. Phys. Chem. C.* **128**, 8324–8330 (2024).
233. Dong, Y. et al. The synergy of plasmonic enhancement and hot-electron effect on $CsPbBr_3$ nanosheets photodetector. *Adv. Mater. Interfaces* **8**, 2002053 (2021).
234. Parveen, S., Paul, K. K. & Giri, P. K. Precise tuning of the thickness and optical properties of highly stable 2d organometal halide perovskite nanosheets through a solvothermal process and their applications as a white LED and a fast photodetector. *ACS Appl. Mater. Interfaces* **12**, 6283–6297 (2020).

235. Mandal, A., Ghosh, A., Ghosh, D. & Bhattacharyya, S. Photodetectors with high responsivity by thickness tunable mixed halide perovskite nanosheets. *ACS Appl. Mater. Interfaces* **13**, 43104–43114 (2021).
236. Sun, R. et al. In situ preparation of two-dimensional ytterbium ions doped all-inorganic perovskite nanosheets for high-performance visual dual-bands photodetectors. *Nano Energy* **93**, 106815 (2022).
237. Lv, J. et al. Epitaxial growth of lead-free 2D $Cs_3Cu_2I_5$ perovskites for high-performance UV photodetectors. *Small* **18**, 2201715 (2022).
238. Ba, Y. et al. Two-dimensional ruddlesden-popper perovskite $Cs_2PbI_2Cl_2$ nanostructures for self-powered visible-blind ultraviolet photodetectors. *ACS Appl. Electron. Mater* **7**, 582–589 (2025).
239. Chen, H. et al. Lead-free perovskite nanoflake/monoradicular CdSe nanobelt hybrid nanostructures for ultrasensitive broadband photodetectors. *ACS Appl. Nano Mater* **5**, 16923–16932 (2022).
240. Ansari, R. M., Salunke, A. D., Rahil, M. & Ahmad, S. Strong photocurrent from solution-processed Ruddlesden-Popper 2D perovskite-MoS_2 hybrid heterojunctions. *Adv. Mater. Interfaces* **10**, 2202170 (2023).
241. Tan, Q. et al. A $CsPbBr_3$/CdS-based hybrid bidirectional optoelectronic device with light-emitting, modulation, and detection functions. *Appl. Phys. Lett.* **124**, 121104 (2024).
242. Wang, T. et al. Flexible array of high performance and stable formamidinium-based low-n 2D halide perovskite photodetectors for optical imaging. *Nano Energy* **116**, 108827 (2023).
243. Fan, S. et al. All-inorganic perovskite $NiTiO_3$/$Cs_3Sb_2I_9$ heterostructure for photocatalytic CO_2 reduction to CH_4 with high selectivity. *Small* **20**, 2311978 (2024).
244. Teng, Y. et al. Dual atom-bridge effect promoting interfacial charge transfer in 2D/2D $Cs_3Bi_2Br_9$/BiOBr epitaxial heterojunction for efficient photocatalysis. *Chin. Chem. Lett* **36**, 110430 (2025).
245. Que, M. et al. 2D/2D Schottky heterojunction of in-situ growth $FAPbBr_3$/Ti_3C_2 composites for enhancing photocatalytic CO_2 reduction. *J. Colloid Interface Sci* **610**, 538–545 (2022).
246. Li, Y.-M., Hou, Z.-Z., Wan, X.-D., Liu, J. & Zhang, J.-T. Halide perovskite-based heterostructures for photocatalytic CO_2 conversion. *Rare Met* **43**, 5453–5472 (2024).
247. Wu, L.-Y. et al. Two-dimensional metal halide perovskite nanosheets for efficient photocatalytic CO_2 reduction. *Sol. RRL* **5**, 2100263 (2021).
248. Zhao, J.-S. et al. Directed electron delivery from a Pb-free halide perovskite to a Co(II) molecular catalyst boosts CO_2 photoreduction coupled with water oxidation. *Angew. Chem.-Int. Ed* **63**, e202401344 (2024).
249. Yuan, S.-X., Su, K., Feng, Y.-X., Zhang, M. & Lu, T. B. Lattice-matched in-situ construction of 2D/2D T-$SrTiO_3$/$CsPbBr_3$ heterostructure for efficient photocatalysis of CO_2 reduction. *Chin. Chem. Lett.* **34**, 107682 (2023).
250. Feng, Y.-X. et al. Self-template-oriented synthesis of lead-free perovskite $Cs_3Bi_2I_9$ nanosheets for boosting photocatalysis of CO_2 reduction over Z-scheme heterojunction $Cs_3Bi_2I_9$/CeO_2. *J. Energy Chem.* **69**, 348–355 (2022).
251. Jiang, Y., Zhou, R., Zhang, Z., Dong, Z. & Xu, J. Boosted charge transfer and CO_2 photoreduction by construction of S-scheme heterojunctions between $Cs_2AgBiBr_6$ nanosheets and two-dimensional metal-organic frameworks. *J. Mater. Chem. C* **11**, 2540–2551 (2023).
252. Liu, Y., Zhang, X., Yang, Z., Chen, K. & Chen, W. Passivation of 2D $Cs_2PbI_2Cl_2$ nanosheets for efficient and stable $CsPbI_3$ quantum dot solar cells. *ACS Appl. Mater. Interfaces* **16**, 22197–22206 (2024).
253. Zhu, L., Lu, Q., Li, C., Wang, Y. & Deng, Z. Graded interface engineering of 3D/2D halide perovskite solar cells through ultrathin $(PEA)_2PbI_4$ nanosheets. *Chin. Chem. Lett.* **32**, 2259–2262 (2021).
254. Bathula, C. et al. Interfacial engineering of quasi-2-D formamidinium lead iodide nanosheets for perovskite solar cell by mechanochemical approach. *Surf. Interfaces* **27**, 101551 (2021).
255. Liu, L. et al. Multi-site intermolecular interaction for in situ formation of vertically orientated 2D passivation layer in highly efficient perovskite solar cells. *Adv. Funct. Mater.* **33**, 2303038 (2023).
256. Xu, Y. et al. Color-stable deep-blue light-emitting diodes based on perovskite nanosheet films passivated with zwitterionic choline chloride and rubidium bromide. *ACS Appl. Nano Mater* **7**, 5784–5790 (2024).
257. Gao, L. et al. Metal halide perovskites blue emitters and light-emitting diodes: a review on morphological and molecular dimensions. *Laser Photonics Rev.* **18**, 2301100 (2024).
258. Wang, C. et al. Single-layer sheets of alkylammonium lead iodide perovskites with tunable and stable green emission for white light-emitting devices. *Adv. Opt. Mater.* **10**, 2200217 (2022).
259. Mishra, K. K. & Sharma, R. Investigating Sr_3NBr_3 halide perovskite for photovoltaic applications: a study of structural, electronic, and optical properties. *Phys. B-Condens. Matter* **704**, 417037 (2025).
260. Caid, M., Rached, D., Al-Qaisi, S., Rached, Y. & Rached, H. DFT calculations on physical properties of the lead-free halide-based double perovskite compound $Cs_2CdZnCl_6$. *Solid State Commun* **369**, 115216 (2023).
261. Behera, D. et al. A DFT insight into the physical features of alkaline based perovskite compounds $AInBr_3$ (A = K, Rb). *Solid State Ion* **409**, 116513 (2024).
262. Bochaoui, H. & El Bouabdellati, M. Exploring the photovoltaic potential of $RbGeCl_3$ perovskite: a DFT and SCAPS-1D approach for lead-free solar cells. *Phys. B-Condens. Matter* **702**, 417007 (2025).
263. Hwang, S., Kim, W., Kim, K. & Ko, M. J. Theoretical studies on the electronic structures of halide perovskites: a critical review. *Korean J. Chem. Eng* **41**, 3737–3749 (2024).
264. Ahmed, H., Mukhtar, S., Agathopoulos, S. & Ilyas, S. Z. Structural, electronic, and optical properties of GA-based lead-free mixed-halide perovskites $Cs_3GaI_{6-x}Br_x$ (0=x=6) for solar cell applications: a DFT study. *Physica B-Condensed Matter* **640** (2022).
265. Bouhmaidi, S. et al. A DFT study of electronic, optical and thermoelectric properties of Ge-halide perovskites $CsGeX_3$ (X=F, Cl and Br). *Comput. Condens. Matter* **31**, e00663 (2022).
266. Chen, J., Feng, M., Zha, C., Zhang, L. & Wang, L. Pseudo-halide anions engineering of $FAPbI_3$ surface and SnO_2/$FAPbI_3$ heterostructure. *Surf. Interfaces* **43**, 103530 (2023).
267. Adam, I. M. et al. SnO_2/Perovskite interface engineering with mixed-halide potassium salts: a pathway to efficient and stable perovskite solar cells through a combined experimental-density functional theory approach. *ACS Appl. Mater. Interfaces* **17**, 31000–31012 (2025).
268. Dar, S. A. & Want, B. Direct band gap double perovskite halide $Cs_2ScInCl_6$ for optoelectronic applications-A first principle study. *Comput. Condens. Matter* **33**, e00736 (2022).
269. Munir, J. et al. First-principles scrutiny of double perovskite halides $A_2AlAuCl_6$ (A = Cs, K, Rb): potential contenders for renewable energy. *Arab. J. Sci. Eng.* **50**, 6511–6522 (2025).
270. Zhou, Z.-R., Liao, Z.-H. & Wang, F. Shape-controlled synthesis of one-dimensional cesium lead halide perovskite nanocrystals: methods and advances. *J. Mater. Chem. C* **11**, 3409–3427 (2023).
271. Liang, G.-Q. & Zhang, J. A machine learning model for screening thermodynamic stable lead-free halide double perovskites. *Comput. Mater. Sci.* **204**, 111172 (2022).
272. Sheng, M., Zhu, H., Wang, S., Liu, Z. & Zhou, G. Accelerated discovery of halide perovskite materials via computational methods: a review. *Nanomaterials* **14**, 1167 (2024).
273. Mannodi-Kanakkithodi, A. & Chan, M. K. Y. Accelerated screening of functional atomic impurities in halide perovskites using high-throughput computations and machine learning. *J. Mater. Sci* **57**, 10736–10754 (2022).
274. Zuo, T., Qi, F., Yam, C. & Meng, L. Lead-free all-inorganic halide double perovskite materials for optoelectronic applications:

progress, performance and design. *Phys. Chem. Chem. Phys.* **24**, 26948–26961 (2022).
275. Wei, X. et al. A domain knowledge enhanced machine learning method to predict the properties of halide double perovskite $A_2B^+B^{3+}X_6$. *J. Mater. Chem. A.* **11**, 20193–20205 (2023).
276. Mishra, S., Boro, B., Bansal, N. K. & Singh, T. Machine learning-assisted design of wide bandgap perovskite materials for high-efficiency indoor photovoltaic applications. *Mater. Today Commun.* **35**, 106376 (2023).
277. Li, X. et al. Machine learning-assisted design of high-performance perovskite photodetectors: a review. Adv. Compos. *Hybrid. Mater.* **8**, 27 (2025).
278. Furasova, A. et al. Nanophotonics for perovskite solar cells. *Adv. Photonics Res* **3**, 2100326 (2022).
279. Hu, W., Zhang, L. & Pan, Z. Designing two-dimensional halide perovskites based on high-throughput calculations and machine learning. *ACS Appl. Mater. Interfaces* **14**, 21596–21604 (2022).
280. Gupta, N., Kumar, R. & Alankar, A. Machine learning-based discovery of novel oxide and halide perovskites for energy storage. *J. Alloy. Compd* **1010**, 177470 (2025).
281. Mishra, P. et al. Synthesis of machine learning-predicted Cs_2PbSnI_6 Double perovskite nanocrystals. *ACS Nano* **19**, 6107–6119 (2025).
282. Meftahi, N. et al. Machine learning enhanced high-throughput fabrication and optimization of quasi-2D Ruddlesden-Popper perovskite solar cells. *Adv. Energy Mater.* **13**, 2203859 (2023).
283. Duan, D. et al. Recent progress with one-dimensional metal halide perovskites: from rational synthesis to optoelectronic applications. *NPG Asia Mater* **15**, 8 (2023).
284. Tran, T. K. T., Nyiera, H. N. & Zhao, J. Instability of colloidal lead halide perovskite nanocrystals: Causes, improvement, and evaluation. *Nano Res* **17**, 10607–10619 (2024).
285. Mathew, P., Cho, J. & Kamat, P. V. Ramifications of ion migration in 2D lead halide perovskites. *ACS Energy Lett* **9**, 1103–1114 (2024).
286. Saleem, M. I., Batool, A. & Hur, J. Cutting-edge developments in metal halide perovskites core/shell heterocrystals: from photodetectors to biomedical applications. *Small* **21**, 2407032 (2024).
287. Sobhanan, J. et al. Luminescent quantum dots: synthesis, optical properties, bioimaging and toxicity. *Adv. Drug Deliv. Rev.* **197**, 114830 (2023).
288. Wu, W. & Chen, C. Suppression and recovery of lead leakage in perovskite solar cells. *Chin. Sci. Bull.-Chin.* **69**, 3283–3298 (2024).
289. Yao, H. et al. Strategies for improving the stability of tin-based perovskite (ASnX3) solar cells. *Adv. Sci.* **7**, 1903540 (2020).
290. Gao, S., Bae, J.-J., Lee, D. S., Yang, T.-Y. & Shin, S. S. Toward sustainable perovskite solar cells: from lead-free materials to environmental concerns and mitigation strategies. *Ecomat* **7**, e70001 (2025).
291. Kim, D., Yun, T., An, S. & Lee, C.-L. How to improve the structural stabilities of halide perovskite quantum dots: review of various strategies to enhance the structural stabilities of halide perovskite quantum dots. *Nano Convergence* **11**, 4 (2024).
292. Fiuza-Maneiro, N. et al. Ligand chemistry of inorganic lead halide perovskite nanocrystals. *ACS Energy Lett* **8**, 1152–1191 (2023).
293. Wang, M. & Carmalt, C. J. Film fabrication of perovskites and their derivatives for photovoltaic applications via chemical vapor deposition. *ACS Appl. Energy Mater* **5**, 5434–5448 (2022).
294. Ding, S., Hao, M., Lin, T., Bai, Y. & Wang, L. Ligand engineering of perovskite quantum dots for efficient and stable solar cells. *J. Energy Chem.* **69**, 626–648 (2022).
295. Deng, C., Huang, Q., Fu, Z. & Lu, Y. Ligand engineering of inorganic lead halide perovskite quantum dots toward high and stable photoluminescence. *Nanomaterials* **14**, 1201 (2024).
296. Wu, Y., Wang, D., Liu, J. & Cai, H. Review of interface passivation of perovskite layer. *Nanomaterials* **11**, 775 (2021).
297. Zhang, F. et al. Perovskite photovoltaic interface: from optimization towards exemption. *Nano Energy* **124**, 109503 (2024).
298. Zeng, Y. et al. The synthesis of metal halide perovskite nanocrystals: surface and interface engineering. *CrystEngComm* **24**, 7345–7359 (2022).
299. Li, S. et al. Recent application and progress of metal halide perovskite photodetector on flexible substrates. *Chin. J. Chem.* **41**, 3689–3702 (2023).
300. Park, I. J., An, H. K., Chang, Y. & Kim, J. Y. Interfacial modification in perovskite-based tandem solar cells. *Nano Converg* **10**, 22 (2023).
301. Azmi, R. et al. Moisture-resilient perovskite solar cells for enhanced stability. *Adv. Mater.* **36**, 2211317 (2024).
302. Chatterjee, S. et al. Strategies to achieve long-term stability in lead halide perovskite nanocrystals and its optoelectronic applications. *J. Phys. Chem. Lett* **15**, 10118–10137 (2024).
303. Otero-Martinez, C., Fiuza-Maneiro, N. & Polavarapu, L. Enhancing the intrinsic and extrinsic stability of halide perovskite nanocrystals for efficient and durable optoelectronics. *Acs Appl. Mater. Interfaces* **14**, 34291–34302 (2022).
304. Du, F. et al. Improving the stability of halide perovskites for photo-, electro-, photoelectro-chemical applications. *Adv. Funct. Mater.* **34**, 2312175 (2024).
305. Cheng, R. et al. Fibrous nanoreactors from microfluidic blow spinning for mass production of highly stable ligand-free perovskite quantum dots. *Angew. Chem.-Int. Ed* **61**, e202204371 (2022).
306. Marques, M. J. M., Lin, W., Taima, T., Umezu, S. & Shahiduzzaman, M. Unleashing the potential of industry viable roll-to-roll compatible technologies for perovskite solar cells: challenges and prospects. *Mater. Today* **78**, 112–141 (2024).
307. Valsalakumar, S., Roy, A., Mallick, T. K., Hinshelwood, J. & Sundaram, S. An overview of current printing technologies for large-scale perovskite solar cell development. *Energies* **16**, 190 (2023).
308. Lu, H., Wu, W., He, Z., Han, X. & Pan, C. Recent progress in construction methods and applications of perovskite photodetector arrays. *Nanoscale Horiz* **8**, 1014–1033 (2023).
309. Bhowmik, K. K. & Zhao, L. Metal halide perovskite light-emitting devices for optical communications: a spotlight on speed, brightness, wavelength tunability, bidirectionality, and integration. *Acs Appl. Electron. Mater* **6**, 8558–8570 (2024).
310. Liu, J., Qu, J., Kirchartz, T. & Song, J. Optoelectronic devices based on the integration of halide perovskites with silicon-based materials. *J. Mater. Chem. A* **9**, 20919–20940 (2021).
311. Hoang, M. T. et al. Towards the environmentally friendly solution processing of metal halide perovskite technology. *Green. Chem.* **23**, 5302–5336 (2021).
312. Zhao, H., Kordas, K. & Ojala, S. Recent advances in synthesis of water-stable metal halide perovskites and photocatalytic applications. *J. Mater. Chem. A* **11**, 22656–22687 (2023).
313. Liu, X. et al. A review on mechanochemistry: approaching advanced energy materials with greener force. *Adv. Mater.* **34**, 2108327 (2022).
314. Tang, X., Quan, W. & Yang, F. Green-route manufacturing towards future industrialization of metal halide perovskite nanocrystals. *Chem. Commun.* **60**, 1389–1403 (2024).
315. Cheng, J., Fan, Z. & Dong, J. Research progress of green solvent in $CsPbBr_3$ perovskite solar cells. *Nanomaterials* **13**, 991 (2023).
316. Fu, Y. et al. Metal halide perovskite nanostructures for optoelectronic applications and the study of physical properties. *Nat. Rev. Mater.* **4**, 169–188 (2019).

Acknowledgements

This work is supported by the Fundamental Research Funds for the Central Universities (grant number 531118010971), the Education Department of Hunan Province (grant number Z202481430960), and the City University of Hong Kong (project no. 7006109, 7020088, and 9229138).

Author contributions

X.P. and Z.L. wrote the manuscript. H.S. and Y.S. contributed to the figure preparation. Y.M. and J.C.H. reviewed and edited the manuscript.

Competing interests

The authors declare no competing interests.

Additional information

Correspondence and requests for materials should be addressed to Zhengxun Lai or You Meng.

Reprints and permissions information is available at http://www.nature.com/reprints

Publisher's note Springer Nature remains neutral with regard to jurisdictional claims in published maps and institutional affiliations.